Chain-Forming Zintl Antimonides as Novel Thermoelectric Materials

Thesis by

Alexandra Zevalkink

In Partial Fulfillment of the Requirements

for the Degree of

Doctor of Philosophy

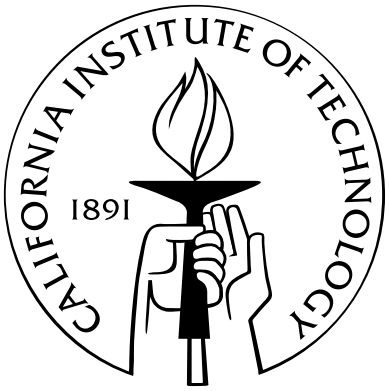

California Institute of Technology

Pasadena, California

2013

(Defended October 7, 2013)

Acknowledgments

First and foremost, I would like to thank my husband, Alex, for supporting me and putting up with me throughout my time as a graduate student. All of my family members have been extremely supportive and encouraging, for which I am immensely grateful.

None of this work would have been possible without the advice and guidance of my research adviser, Jeff Snyder, who has been an absolute pleasure to work with for the past five years.

I have also benefited from the help of several close collaborators who have contributed to this work both intellectually and experimentally. Eric Toberer is responsible for starting me down the path of Zintl research, and guiding the first several years of work on the materials in this thesis. Greg Pomrehn performed the majority of the computational work, and Wolfgang Zeier contributed his considerable knowledge of solid state chemistry.

I would also like to acknowledge my friends and colleagues in Jeff Snyder's research group, from whom I have learned most of what I now know about thermoelectric materials. In addition, much of the experimental work described herein could not have been accomplished without the help of the scientists and staff in the thermoelectric group at the Jet Propulsion Laboratory. I would particularly like to thank Sabah Bux and Jean-Pierre Fleurial.

Abstract

Zintl phases, a subset of intermetallic compounds characterized by covalently-bonded "sub-structures," surrounded by highly electropositive cations, exhibit precisely the characteristics desired for thermoelectric applications. The requirement that Zintl compounds satisfy the valence of anions through the formation of covalent substructures leads to many unique, complex crystal structures. Such complexity often leads to exceptionally low lattice thermal conductivity due to the containment of heat in low velocity optical modes in the phonon dispersion. To date, excellent thermoelectric properties have been demonstrated in several Zintl compounds. However, compared with the large number of known Zintl phases, very few have been investigated as thermoelectric materials.

From this pool of uninvestigated compounds, we selected a class of Zintl antimonides that share a common structural motif: anionic moieties resembling infinite chains of linked $M\mathrm{Sb}_4$ tetrahedra, where M is a triel element. The compounds discussed in this thesis ($A_5M_2\mathrm{Sb}_6$ and $A_3M\mathrm{Sb}_3$, where A = Ca or Sr and M = Al, Ga and In) crystallize as four distinct, but closely related "chain-forming" structure types. This thesis describes the thermoelectric characterization and optimization of these phases, and explores the influence of their chemistry and structure on the thermal and electronic transport properties. Due to their large unit cells, each compound exhibits exceptionally low lattice thermal conductivity (0.4 - 0.6 W/mK at 1000 K), approaching the predicted glassy minimum at high temperatures. A combination of Density Functional calculations and classical transport models were used to explain the experimentally observed electronic transport properties of each compound. Consistent with the Zintl electron counting formalism, $A_5M_2\mathrm{Sb}_6$ and $A_3M\mathrm{Sb}_3$ phases

were found to have filled valence bands and exhibit intrinsic electronic properties. Doping with divalent transition metals (Zn^{2+} and Mn^{2+}) on the M^{3+} site, or Na^{1+} on the A^{2+} site allowed for rational control of the carrier concentration and a transition towards degenerate semiconducting behavior. In optimally-doped samples, promising peak zT values between 0.4 and 0.9 were obtained, highlighting the value of continued investigations of new Zintl phases.

Contents

List of Figures

List of Tables

Chapter 1

Introduction

1.1 Thermoelectric Energy Conversion

Solving society's current energy dilemma requires both broadening our energy resources and reducing our energy consumption. Since more than 50% of the energy consumed nationwide is lost as waste heat, the recovery of even a small fraction of this energy through the use of thermoelectric generators has the potential to significantly impact the global energy landscape [15]. While this solid state technology is currently used in extraterrestrial and other specialized applications, further improvements in cost and efficiency of thermoelectric materials are required for thermoelectric generators to be competitive in most automotive and industrial waste heat applications.

The construction of a thermoelectric generator is shown schematically in Figure 1.1 a. Here, two thermoelectric 'legs' made of n-type and p-type materials are alternated such that they are electrically in series and thermally in parallel. For power generation, the legs are placed across a temperature gradient, causing the carriers to move towards the cold end, and generating a voltage across each leg. This behavior, known as the Seebeck effect, is the basis of thermoelectric energy conversion. In reverse, the same device operates as a Peltier cooler, where an applied voltage generates a temperature gradient [16].

The conversion efficiency of a given thermoelectric material is dependent on the figure of merit, or zT value, which is defined such that $zT{=}\infty$ corresponds to the Carnot efficiency. The figure of merit is given by $zT = \frac{\alpha^2 T}{\sigma\kappa}$ [17, 18]. The Seebeck

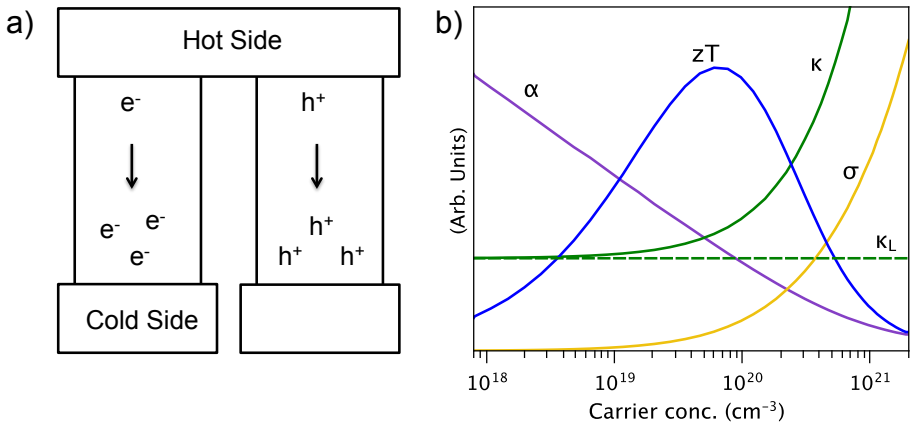

Figure 1.1: a) Schematic of a thermoelectric generator. b) A balance between insulating and metallic behavior must be achieved to obtain high zT.

coefficient (α) is the voltage generated due to a temperature gradient (α=ΔV/ΔT). The electrical resistivity ($\rho = 1/\sigma$, where σ is conductivity) and thermal conductivity (κ), are, respectively, parasitic sources of voltage and heat loss, and must be minimized. Traditional thermoelectric materials have zT near unity, corresponding to about 10% of the Carnot efficiency. However there have been an increasing number of reports of larger zT through enhancements in both electronic and thermal properties [19, 20, 21, 6].

Figure 1.1b illustrates the balance that must be achieved in order to obtain high thermoelectric efficiency; a large Seebeck coefficient is found in low carrier concentration (n) insulators, while high electrical conductivity is found in high carrier concentration metals. As a consequence, most good thermoelectric materials are heavily doped semiconductors with carrier concentrations between 10^{19} to 10^{21} carriers/cm^3 [18]. Thermoelectric optimization is complicated by the transport of heat, which is carried by both phonons, which lead to lattice thermal conductivity (κ_L), and by charge carriers, which lead to electronic thermal conductivity (κ_e) and bipolar thermal conductivity (κ_B). The electronic term is related to the electrical conductivity through the Wiedemann-Franz law ($\kappa_e = L\sigma T$), where the Lorenz factor (L) can be calculated from Boltzmann transport theory.

Ideal thermoelectric materials must therefore be both excellent electronic conductors and poor phonon conductors. This combination of properties is challenging to obtain due to the strongly coupled nature of α, ρ, and κ [18]. In the past decade, however, several effective approaches have emerged for the design of such materials. One frequent strategy is the addition of phonon scattering sources, such as grain boundaries, impurities, or nano-precipitates, to reduce lattice thermal conductivity while minimally impacting charge carrier transport. This has been most successful in traditional semiconductors with inherently high electronic mobility such as Si [22]. A second promising approach is the manipulation of electronic band structures via either doping or alloying to take advantage of multiple charge carrier pockets in the Fermi surface. This leads to excellent thermoelectric properties in compounds such as LaTe and PbTe [19, 23]. Lastly, materials with complex crystal structures have been exploited for their inherently low lattice thermal conductivities. For example, exceptionally low lattice thermal conductivity is found in the Zintl phase $Yb_{14}MnSb_{11}$, which contains 104 atoms in its primitive cell [21]. Such complexity results in glass-like lattice thermal conductivity at high temperatures, due to confinement of heat in low velocity, optical phonon modes, as well as additional opportunities for scattering events. This thesis, which describes the characterization and optimization of a new class of complex Zintl phases, favors the latter of these strategies.

1.2 Introduction to Zintl Phases

1.2.1 Zintl Chemistry

The term "Zintl phase" was used first by F. Laves to describe a class of intermetallic compounds systematically investigated by Eduard Zintl during the 1930's [24, 25]. Eduard Zintl studied intermetallic compounds in an era during which the distinction between salt-like insulators and intermetallic compounds was becoming increasingly blurred. Eduard Zintl was interested in determining which combinations of metallic and metalloid elements resulted in the formation of salt-like structures [26]. The rules

that he developed to explain the formation of such structures were later extended and generalized by W. Klemm [27]. R. Hoffman has described the Zintl-Klemm concept as "the single most important theoretical concept in solid-state chemistry of the last century." [28]

Chemically, Zintl phases can be placed between insulating, salt-like compounds and intermetallic compounds [29]. In salt-like compounds (e.g., sulfates, phosphates, and a vast array of silicates), both the anions and cations obtain a full octet or "18 electron shell." Barite ($BaSO_4$) is an excellent example, in which Ba donates its two valence electrons to support the formation of $[SO_4]^{2-}$ tetrahedra. Such compounds possess large band gaps, and generally exhibit insulating behavior. In contrast, many intermetallic phases, despite their highly complex, ordered structures, are electron deficient or lack a band gap, leading to metallic behavior.

Zintl phases are characterized by highly electronegative cations that donate their electrons to an anionic substructures. The Zintl-Klemm concept rationalizes the structural and bonding characteristics of Zintl phases by assuming that the cation transfers its valence electrons fully to the anions. The anions must in turn form covalently-bonded polyanions to obtain closed shells (filled octet) [24]. Referred to by W. Pearson as "valence compounds," [30], Zintl phases are distinguished from other intermetallic compounds by their valence-precise nature. Fundamentally, Zintl phases are more closely related to the salt-like compounds described above, in which all octets are filled. However, the constituent elements in Zintl compounds are different, leading, ultimately, to different structure types and semiconducting rather than insulating electronic behavior. Zintls compounds are formed traditionally from a combination of an alkali or alkaline earth metal and a post-transition metal or metalloid from group 13, 14, 15, or 16. A classic example is NaSi, in which the Si atoms form $[Si_4]^{4-}$ tetrahedra to yield a valence-precise structure [31]. More recently, the criteria for the cation has expanded to include rare earth metals. Ternary Zintl compounds may also contain transition metals in addition to the requisite cation and group 13-16 anions. For example, the compound $YbZn_2Sb_2$ [32] forms the same structure type as the more traditional Zintl phase, $CaAl_2Si_2$ [33].

The guiding principle for rationalizing the number of covalent bonds in a Zintl structure is given by the 8-N rule, in which N is the total valence electron count. The total valence electron count (VEC) simply describes the total number of electrons available to each anion in the structure, including those donated by the cations. For a binary compound, A_aX_x, the VEC is given by Eq. 1.1, where $e(A)$ and $e(X)$ are the valence counts for A and X respectively. Typically, it is assumed that there are no bonds between A atoms, and that X can have $X-X$ bonds that are considered to be two-center, two-electron bonds, and also that the octet rule is satisfied for both elements.

$$VEC = (a \cdot e(A) + x \cdot e(X))/x \tag{1.1}$$

For example, in NaTl, VEC = (1·1 + 1·3) / 1 = 4. Since (8 - VEC) = 4, each Tl is expected to form four Tl-Tl bond. The resulting anionic structure is a Tl diamond lattice (B32, Strukturbericht classification). In NaSi, $VEC = 5$, requiring the formation of 3 additional bonds per Si atom, and leading to the isolated $[Si_4]^{4-}$ tetrahedra observed in this structure type.

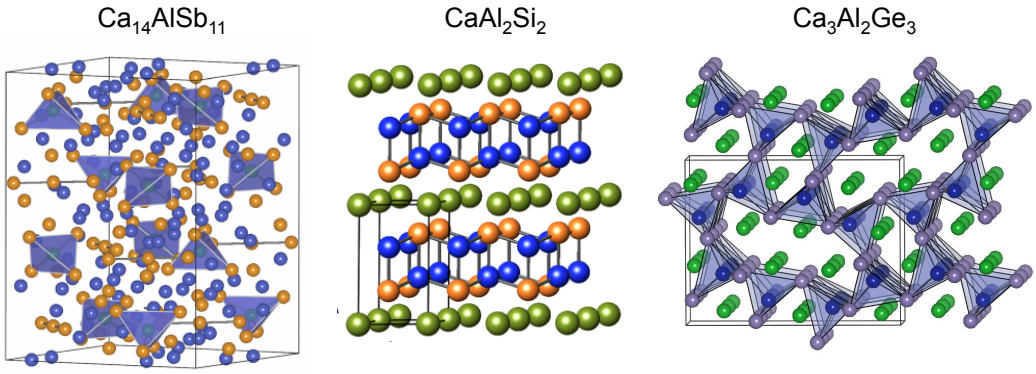

Figure 1.2: Examples of classic Zintl structure types with 0-, 2-, and 3-dimensional anionic substructures.

The requirement that Zintl compounds satisfy the valence of anions through the formation of covalent substructures leads to many unique, complex crystal structures. In some cases the resulting polyanions are simple, isolated units such as the $[Si_4]^{4-}$ tetrahedra in NaSi. In others, a single structure type contains several differ-

ent types of anionic moieties. Take for example the extremely complex structure of $Ca_{14}AlSb_{11}$, shown below in Figure 1.2a. A single formula unit contains 4 isolated Sb^{3-}, an $[AlSb_4]^{9-}$ tetrahedra, and a linear $[Sb_3]^{7-}$ moiety. The 14 Ca^{2+} cations lead to overall charge-balance [34]. In many Zintl phases, extended 2-dimensional or 3-dimensional networks are formed. For example, in compounds with the $CaAl_2Si_2$ structure type (Figure 1.2b), Ca contributes two electrons to Al and Si, which form infinitely extending 2-dimensional $[Al_2Si_2]^{2-}$ slabs [33]. $Ca_3Al_2Ge_3$, in contrast, forms a 3-dimensional net of corner-linked $AlGe_4$ tetrahedra. [35]. The electron deficiency of the $[Al_2Ge_3]^{6-}$ sublattice is balanced by the 3 Ca^{2+} cations that reside in the tunnels. In each case, the structure can be rationalized by using simple electron counting rules. A testament to its effectiveness, the Zintl-Klemm concept is still used today to guide the discovery of new structure types and compounds.

1.2.2 Thermoelectric Zintl Phases

The rich chemistry of Zintl compounds leads to many of the characteristics desired for thermoelectric applications: complex structures, extensive opportunities to tune transport properties, narrow band gaps, and thermal and chemical stability [36, 37]. However, it was not until 2005 that Zintl compounds were recognized as potential thermoelectric materials with the discovery of high zT in $Yb_{1-x}Ca_xZn_2Sb_2$ by Gascoin et al.[32]. Shortly thereafter, the thermoelectric properties of the degenerately p-doped Zintl compound $Yb_{14}MnSb_{11}$ were investigated by Brown et al in 2006 [38]. $Yb_{14}MnSb_{11}$ was found to have a figure of merit of 1 at 1000 K. Compared with the state-of-the-art high temperature p-type material $Si_{0.8}Ge_{0.2}$, this was an improvement of a factor of two. Further optimization of the $Yb_1Zn_2Sb_2$ system has since been achieved via alloying [39, 40, 41], while $Yb_{14}MnSb_{11}$ has been improved via doping [21, 42, 43] and through improvement of the synthetic process [44]. Beyond these examples, very few Zintl compounds have been optimized as thermoelectric materials.

A number of investigated Zintl compounds were found to have very small band gaps or to otherwise behave as metals [45, 46, 47, 48]. When the metallic behavior

arises from a small or negative band gap, there is very little potential for thermoelectric applications. Several recently discovered Zintl phases are known to possess band gaps, but the transport properties have not yet been fully characterized. For example, $BaGa_2Sb_2$, $Ba_4In_8Sb_{16}$, $Eu_{11}Zn_6Sb_{12}$, $Eu_7Ga_6Sb_8$, $Eu_{10}Mn_6Sb_{13}$, $Ba_2Sn_3Sb_6$, $Ba_3Ga_4Sb_5$, and $Ba_2In_5As_5$ exhibit unique, complex structures and appear to have energy gaps in their electronic structures [49, 50, 51, 52, 53, 54, 55, 56]. However, the vast majority of known Zintl compounds have not been studied beyond the initial crystallographic characterization.

Clathrate compounds, characterized by covalent, anionic cages containing ionically-bonded cations, can also be considered Zintl phases [6]. Clathrate compounds have been the focus of frequent studies of their unique chemistry [57, 58] and excellent thermoelectric properties [59]. As they comprise their own field of study, they will not be discussed further here. Skutterudite compounds are yet another group of excellent thermoelectric materials [60, 61, 62] that sometimes meet the definition of a Zintl phase, but are ubiquitous enough to be considered as a separate field of study.

1.3 Electronic Transport in Zintl phases

1.3.1 Carrier Concentration Optimization

Due to their valence-precise nature, Zintl compounds are ideally semiconductors with fully filled valence bands [36, 37], provided the band gap is greater than zero. Zintl compounds generally behave as intrinsic semiconductors with very low carrier concentrations ($n > 10^{19}$ carriers/cm^3), low electronic conductivity, σ, and high Seebeck coefficients, α. In contrast, high zT generally occurs in heavily doped semiconductors with n between 10^{19}-10^{20} carriers/cm^3. Fortunately, most Zintl compounds can be doped to obtain degenerate semiconducting behavior, and by rationally optimizing the electronic properties, large improvements in zT relative to undoped material can be achieved. It is worth noting that degenerately doped Zintl compounds no longer meet the strict definition of a Zintl phase, as they are not valence-precise. However,

in this thesis, and in the literature in general, such compounds are referred to as Zintl phases as long as the parent compound is valence-precise.

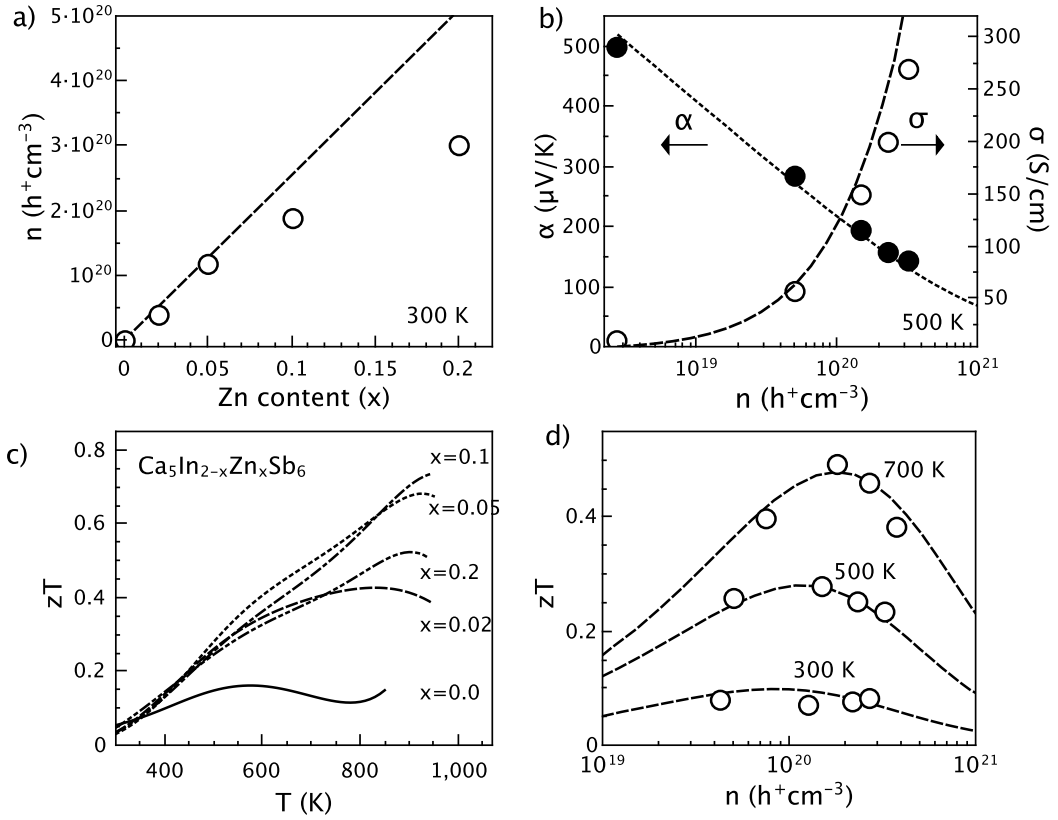

Figure 1.3: Influence of Zn doping on the room temperature (a) carrier concentration, (b) Seebeck coefficient and conductivity, and (c-d) figure of merit of $Ca_5In_2Sb_6$.

Figure 1.3 illustrates the effects of doping the Zintl phase $Ca_5In_2Sb_6$ with an alio-valent element (Zn^{2+}) on the In^{3+} site. Increasing the Zn content leads to a valence imbalance and thus to increased n (Figure 1.3a), decreased α coefficient and increased σ (Figure 1.3b), and an improved figure of merit (Figure 1.3 c-d). A single parabolic band model (SPB model) can be used to approximate the dependence of σ and α on n (dashed curves in Figure 1.3b) by assuming that the band mass (m^*) is invariant with doping (rigid band approximation), and that acoustic phonons are the predominant scattering mechanism. The figure of merit can also be modeled as a function of carrier concentration, if the lattice thermal conductivity is assumed to be independent of doping. This is illustrated in Figure 1.3d for the $Ca_5In_{2-x}Zn_xSb_6$

system. While an SPB model can reduce the need to synthesize a large number of samples, the input parameters should ideally be obtained from an extrinsically doped sample, and the model should be employed only at temperatures below the onset of minority carrier effects. A more detailed description of the SPB model and its limitations can be found in ref. [6] and in Chapter 2.

In traditional Zintl phases, the maximum carrier concentration that can be achieved is usually limited by the solubility of the dopant. The chemistry and electronic structure of the Zintl phase also plays a role; doping leads to an electron deficiency in which some bonding states are left unfilled, potentially destabilizing the structure.

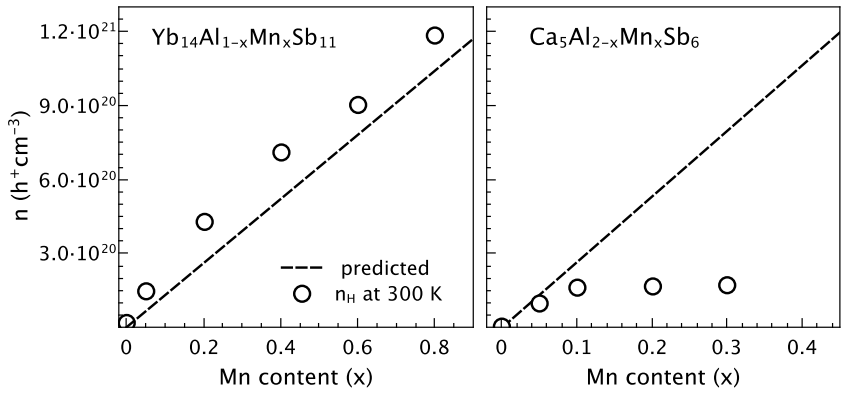

Figure 1.4: Left panel: The carrier concentration in $Yb_{14}Al_{1-x}Mn_xSb_{11}$ increases linearly with increasing x. Right panel: In contrast, in $Ca_5Al_{2-x}Mn_xSb_6$, n increases linearly only at very low Mn concentrations.

Doping Limitations Some Zintl phases are able to tolerate very large dopant concentrations and show highly degenerate behavior, while in others, doping is very limited. For example, $Yb_{14}MSb_{11}$ compounds tolerate $n_H > 10^{21} h^+/cm^3$ [21]. The $Yb_{14}MSb_{11}$ structure is valence precise when M is 3^+. $Yb_{14}MnSb_{11}$ (in which Mn is divalent) can thus be regarded as a heavily doped analogue of the valence-precise Zintl phase, $Yb_{14}AlSb_{11}$. The carrier concentration in the Mn-analogue (n_H = 1.2 x $10^{21} h^+/cm^3$) is consistent with simple charge counting predictions, assuming that each substitution leads to one free hole. This high doping tolerance in $Yb_{14}MSb_{11}$

compounds may be partly explained by the presence of several heavy bands (and thus a large density of states) slightly below the valence band edge [63]. In contrast, the $Ca_5Al_2Sb_6$ system tolerates only 5 at% Mn on the Al site, leading to a maximum carrier concentration of 2 x $10^{20} h^+/cm^3$ [64].

While most Zintl compounds can be doped to obtain degenerate p-type semiconducting behavior, n-type behavior is rarely reported. Since n-type doping fills anti-bonding states in the conduction band, the resulting chemical instability may cause the formation of more stable secondary phases [65]. Alternatively, attempts to increase the Fermi level through n-type chemical doping may encourage the formation of compensating defects (e.g., vacancies, substitutions, or interstitial defects), effectively pinning the Fermi level close to the valence band maximum. In the case of AZn_2Sb_2 compounds (A = Ca, Sr, Eu, Yb), this was demonstrated by Pomrehn et al. [66] using Density Functional theory. The formation enthalpy for cation vacancies was found to decrease with increasing Fermi level, making n-type behavior thermodynamically unattainable due to the inevitable formation of positively charged cation vacancies.

Non-Stoichiometric Phases Stretching the limit of the Zintl formalism are compounds that cannot be synthesized with a valence-precise composition, such as $Yb_9Mn_{4+x}Sb_9$. The $Yb_9Mn_{4+x}Sb_9$ system is valence-precise when $x = 0.5$. However, when x is greater than zero, the additional Mn atoms must occupy interstitial sites [67]. The competing energetic requirements of charge balance and structural stability lead to an electron deficient composition of approximately $Yb_9Mn_{4.2}Sb_9$. The resulting high p-type carrier concentration (2 x 10^{20} h^+/cm^3) is very close to the optimal n predicted by an SPB model, leading to excellent thermoelectric performance without the need for doping [68].

Similarly, AZn_2Sb_2 samples (A = Ca, Sr, Eu, Yb) are consistently found to have large carrier concentrations despite the lack of a dopant [66]. In this case, a high concentration of thermodynamically stable vacancies, as described above, are responsible for the observed behavior. Pomrehn et al demonstrated that A-site vacancies

in $A\mathrm{Zn_2Sb_2}$ compounds depend strongly on the electronegativity of A. While electronegativity influences the degree of electron transfer between the anion and cation in a bond, it does not directly affect the total number of electrons in the valence band or the concentration of free carriers (assuming the valence state of the cation is unaltered). However, the bonding character does influence the bond strength and lattice energy, and, in turn, affects the thermodynamically stable concentration of lattice defects. In this way, the electronegativity of the cation indirectly affects the electronic carrier concentration. This mechanism may be generally applicable, perhaps explaining similar trends seen in $\mathrm{A_{14}MnSb_{11}}$ and $A_9\mathrm{Mn_{4+x}Sb_9}$ (A = Yb or Ca) based materials [69, 70].

1.3.2 Band Structure Criteria

When selecting and optimizing Zintl phases for thermoelectric applications, several key characteristics of the electronic band structure should be considered. The most critical requirement is the presence of a band gap ($E_g > 0$), which allows a single carrier type to dominate transport. The magnitude of E_g determines the temperature at which minority carrier effects begin to negatively impact thermoelectric performance (e.g., bipolar thermal conductivity and degradation of the Seebeck coefficient) [71, 16]. Many Zintl compounds are semiconductors with small band gaps ($E_g < 1$ eV), although semimetallic Zintl phases, in which the conduction and valence bands overlap ($E_g < 0$ eV), have also been reported [72]. Good thermoelectric performance is most often found in materials with band gaps in the range of 0.2 and 0.6 eV.

The band mass, anisotropy, and the number of bands involved in transport (band degeneracy, N_v) also play an important role in determining thermoelectric performance. The effective mass presents a fundamental conflict; while a light inertial effective mass (m_i^*) along the direction of transport is desired for high mobility ($\mu = \tau/m_i^*$, where τ=carrier relaxation time), a heavy "density of states effective mass" (m_{DOS}^*) is necessary for a high Seebeck coefficient [16, 71]. When electrons are scattered primarily by acoustic phonons, as is the case in most known thermoelectric materials, the

improvement in mobility conferred by a light band mass outweighs the detrimental effect on the Seebeck coefficient [73].

The density of states effective mass and the inertial effective mass are related to the band degeneracy by Eq. 1.2. This relationship suggests that when N_v is large and m_i^* is small, a high Seebeck coefficient and high mobility can be obtained simultaneously [17].

$$m_{DOS}^* = m_i^* N_v^{2/3} \tag{1.2}$$

Of the Zintl band structures reported to date, the number of bands involved in p-type transport near the valence band edge varies from one to three. This is far less than that of the most successful thermoelectric materials such as PbTe and its alloys, which have up to N_v =16 [19]. This disparity is partly explained by the higher symmetry of the latter compounds, which leads to multiple symmetrically equivalent carrier pockets [17]. However, there is no theoretical limitation on N_v in Zintl compounds, suggesting that a computational survey may reveal Zintl phases with high N_v.

Because electronic mobility is higher in covalent materials than in ionic materials, it is often assumed that charge transport in Zintl compounds occurs preferentially through the anionic framework. This is supported by the influence that the dimensionality and orientation of the covalently bonded sublattice appears to have on the anisotropy of the electronic band structure in some Zintl phases. For example, in $Ca_5Al_2Sb_6$, the lightest band mass is parallel to the chains of corner-linked $AlSb_4$ tetrahedra [74]. In AZn_2Sb_2, the bands are lightest along the directions within the plane of the covalent Zn_2Sb_2 slabs [75]. In contrast, $Ca_{14}MnBi_{11}$, which is characterized by isolated $MnBi_4$ tetrahedra, has a relatively isotropic band dispersion with no clearly preferred direction for charge transport [63]. It is not yet clear, however, whether transport along the anionic framework is controlled by the covalent bonds themselves, or the "non-bonding" states that comprise the valence band edge. Anisotropic transport has not been confirmed experimentally due to the difficulty of

growing sufficiently large single crystal or oriented polycrystalline samples.

1.3.3 Carrier Relaxation Time

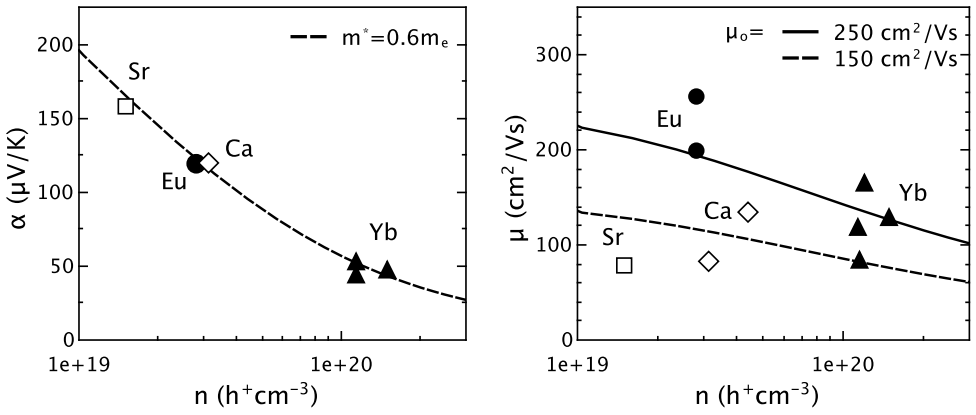

Figure 1.5: (a) $A\mathrm{Zn_2Sb_2}$ samples (A = Sr, Eu, Ca, Yb) have a broad range of carrier concentrations, but all can be described by the same band mass ($m^* = 0.6\ m_e$) within a single parabolic band model. (b) In contrast, the mobility of $A\mathrm{Zn_2Sb_2}$ samples varies widely, suggesting large differences in the carrier relaxation time, τ_e.

The charge carrier relaxation time, τ_e, is a critical but often-overlooked transport parameter. In most bulk thermoelectric materials at high temperature (> 300 K), τ is limited by acoustic phonon scattering. In this limit, the temperature dependence of the carrier mobility decreases as $\mu_H \propto T^{-\nu}$, where ν is between 1 and 1.5 for degenerate and non-degenerate behavior, respectively [76].

The relationship between the magnitude of τ_e and the structure and chemistry of Zintl phases is not yet well understood. The $A\mathrm{Zn_2Sb_2}$ series, where A = Sr, Ca, Eu, or Yb, provides a good example of the large variation in τ_e that can result from chemical substitutions. The electronic mobility in $A\mathrm{Zn_2Sb_2}$ compounds is very high relative to most Zintl phases, in part due to relatively light m_i^*. Transport data suggests that m_{DOS}^* in $A\mathrm{Zn_2Sb_2}$ remains constant regardless of the choice of cation, as illustrated by the pisarenko curve (Figure 1.5a) generated using an SPB model with an effective mass of $m^* = 0.6\ m_e$ [75]. Computational studies have also confirmed similar effective mass values across the $A\mathrm{Zn_2Sb_2}$ series [75, 66]. Despite this, the

carrier mobility is found to be significantly higher in the rare earth analogues than in the alkaline earth analogues (Figure 1.5b) [26]. A recent investigation of $A\mathrm{Zn_2Sb_2}$ single crystals (included in Figure 1.5b), by May et. al suggests that this trend is an intrinsic material property, rather than a result of processing [77]. This behavior has not yet been rationalized, and cannot be readily explained by material parameters.

1.4 Lattice Thermal Conductivity

1.4.1 Introduction

Thermal conductivity (κ) in bulk semiconductors arises primarily from electronic (κ_e), bipolar (κ_B), and lattice (κ_L) contributions [78, 79, 80, 7]. The electronic component is reasonably well-described by the Wiedemann-Franz law, scaling linearly with electrical conductivity and temperature according to $\kappa_e = LT\sigma$. The Lorenz number, L, can be obtained using classic solutions to the Boltzmann transport equation, described in Chapter 2. The bipolar contribution is due to the recombination of n- and p-type charge carriers on the cool side the sample, releasing energy as heat [71]. This term is significant only when intrinsic carriers dominate transport (e.g., in compounds with small band gaps, in intrinsic semiconductors, or at very high temperatures). The lattice contribution arises from phonon transport and is the subject of this section.

The discovery of complex, bulk thermoelectric materials with intrinsically low lattice thermal conductivity, (e. g., $\mathrm{Yb_{14}MnSb_{11}}$, $\mathrm{Ba_8Ga_{16}Ge_{30}}$, $X_y\mathrm{Co_4Sb_{12}}$) has led to many of the recent advances in thermoelectric performance [21, 59, 6, 60]. Understanding the origins of this behavior is important for the development of advanced materials. The complexity of these materials, however, makes *ab initio* calculations of lattice dynamics prohibitively difficult [81, 82, 83, 84, 85, 86]. In this section, simple models for heat transport are used to approximate the complex interplay of phonon

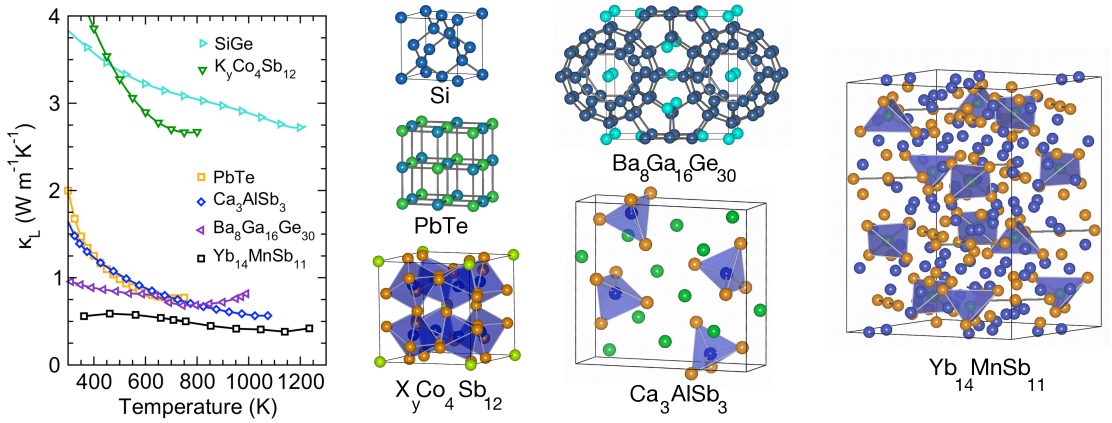

Figure 1.6: Thermoelectric materials can achieve low lattice thermal conductivity through point scattering sources ($Si_{1-x}Ge_x$, $X_yCo_4Sb_{12}$ [1, 2, 3]), heavy atoms and anharmonic bonding (PbTe), and complex crystal structures, in which most of the phonon dispersion consists of low velocity optical modes ($Yb_{14}MnSb_{11}$, Ca_3AlSb_3, $Ba_8Ga_{16}Ge_{30}$) [4, 5, 6].

scattering and group velocity. Despite these approximations, these models highlight the critical material parameters that ultimately determine thermal conductivity.

To lay the groundwork for a more in-depth examination of factors affecting lattice thermal conductivity, we consider Eq. 1.3, which describes κ_L as the product of heat capacity (C_v), phonon velocity (ν), and phonon mean free path (l). This equation provides a rough guide to κ_L by neglecting the frequency dependence of each parameter. The phonon relaxation time, τ, is related to l by the phonon velocity. The phonon velocity is often simply approximated by the low frequency speed of sound ($\nu_s \propto \sqrt{B/d}$), where B is the appropriate elastic modulus and d is the density of the material.

$$\kappa_L = \frac{1}{3} C_v \nu l = \frac{1}{3} C_v \nu^2 \tau \qquad (\nu = l/\tau) \tag{1.3}$$

Traditionally, achieving low lattice thermal conductivity has relied on (a) low ν_s, found in dense materials with soft bonds, or (b) reduction of τ by the intentional introduction of point defects and nanostructures to scatter phonons [87, 88, 89, 90, 1, 91]. Figure 1.6 shows the success of these approaches in PbTe and in Si.

While Eq. 1.3 qualitatively describes κ_L, the universal relaxation time and constant velocity used in this model leads to significant inconsistencies and departure

from experimental results. Crucial to the development of materials with controlled phonon transport is a frequency-dependent description of κ_L, as all of the terms in Eq. 1.3 vary significantly across the phonon spectrum. Use of a simplified version of the Callaway model gives Eq. 1.4 [92, 93], which neglects the small correction term for non-resistive (normal) phonon-phonon interactions [79, 81, 82, 94].

$$\kappa_L = \frac{1}{3}\int_0^{\omega_{max}} C_s(\omega)\nu_g(\omega)^2\tau(\omega)d\omega \tag{1.4}$$

The need for frequency-dependent analysis is revealed by considering bulk silicon. Eq. 1.3 yields $l = 45$ nm at 300 K, using experimental κ_L, heat capacity, and speed of sound. In contrast, a more thorough analysis by Dames et al. using Eq. 1.4 indicates that 80% of the lattice thermal conductivity arises from phonons with mean free paths between 0.1 - 10 μm [95]. This latter result is consistent with experimental results showing significant reduction in κ_L when phonon scattering sources are induced at micron length scales [96].

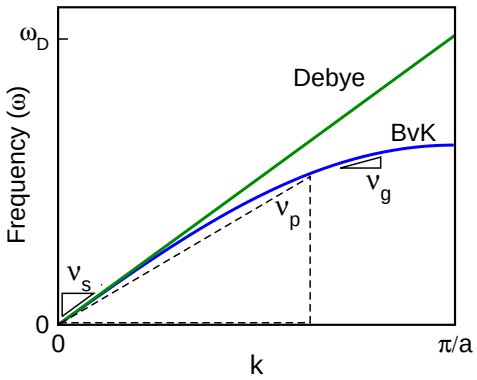

Figure 1.7: In a Debye model, the speed of sound (ν_s), phase velocity (ν_p), and group velocity (ν_g) are equivalent. In contrast, the Born-von Karman model for a monoatomic chain shows significant curvature of the phonon dispersion.

1.4.2 Thermal Conductivity within the Debye Model

The Debye model is a reasonable starting point for discussing thermal transport in simple crystalline materials, as it approximates the phonon group velocity (ν_g =

$d\omega/dk$) and phase velocity ($\nu_p = \omega/k$) as the speed of sound, ν_s (Figure 1.7) [97, 98]. Here, ν_s is the appropriate average of the longitudinal and transverse velocities at the low frequency limit. By neglecting the frequency dependence of velocity, we can focus fully on the frequency dependence of the heat capacity and relaxation time. The Debye model has a maximum phonon frequency given by $\omega_{max} = \omega_D = (\frac{6\pi^2}{V})^{1/3}\nu_s$, where V is the atomic volume. The corresponding Debye temperature is given by $k_B\Theta_D = \hbar\omega_D$.

Heat Capacity The Debye specific heat capacity is given by Eq. 1.5. We are interested in the *spectral* heat capacity ($C_s(\omega)$), which is the integrand of Eq. 1.5, shown in Figure 1.8(a) at various temperatures. At high temperature, the frequency dependence of $C_s(\omega)$ approaches ω^2 and can be approximated by Eq. 1.6. Integrating Eq. 1.6 to ω_D yields the Dulong Petit approximation ($3k_B$ per atom) for the heat capacity.

$$C_v = \frac{3\hbar^2}{2\pi^2 k_B T^2} \int_0^{\omega_{max}} \frac{\omega^4 e^{\hbar\omega/k_B T}}{\nu_g \nu_p^2 (e^{\hbar\omega/k_B T} - 1)^2} d\omega \tag{1.5}$$

$$C_{s,HT}(\omega) = \frac{3k_B\omega^2}{2\pi^2\nu_g\nu_p^2} \tag{1.6}$$

Phonon Relaxation Time The phonon relaxation time, $\tau(\omega)$, is typically limited by a combination of phonon-phonon scattering, point defect scattering, and, in nanostructured materials, boundary scattering, which sum according to Eq. 1.7.

$$\tau^{-1} = \sum_i \tau_i^{-1} \tag{1.7}$$

At temperatures above θ_D, Umklapp phonon-phonon scattering is often the dominant scattering effect. Umklapp scattering depends strongly on the anharmonicity of the bonding, described by the Grüneisen parameter (γ) [99, 100], as well as the average mass ($\bar{M}$) and temperature (T), as seen in Eq. 1.8. Although many expressions exist for τ_U, we emphasize the universality of $\tau_U \propto \frac{\bar{M}\nu^3}{V^{1/3}\omega^2\gamma^2 T}$ and similarity of the pre-factor [94, 101, 102, 103, 104]. It is instructive to consider the rock salt

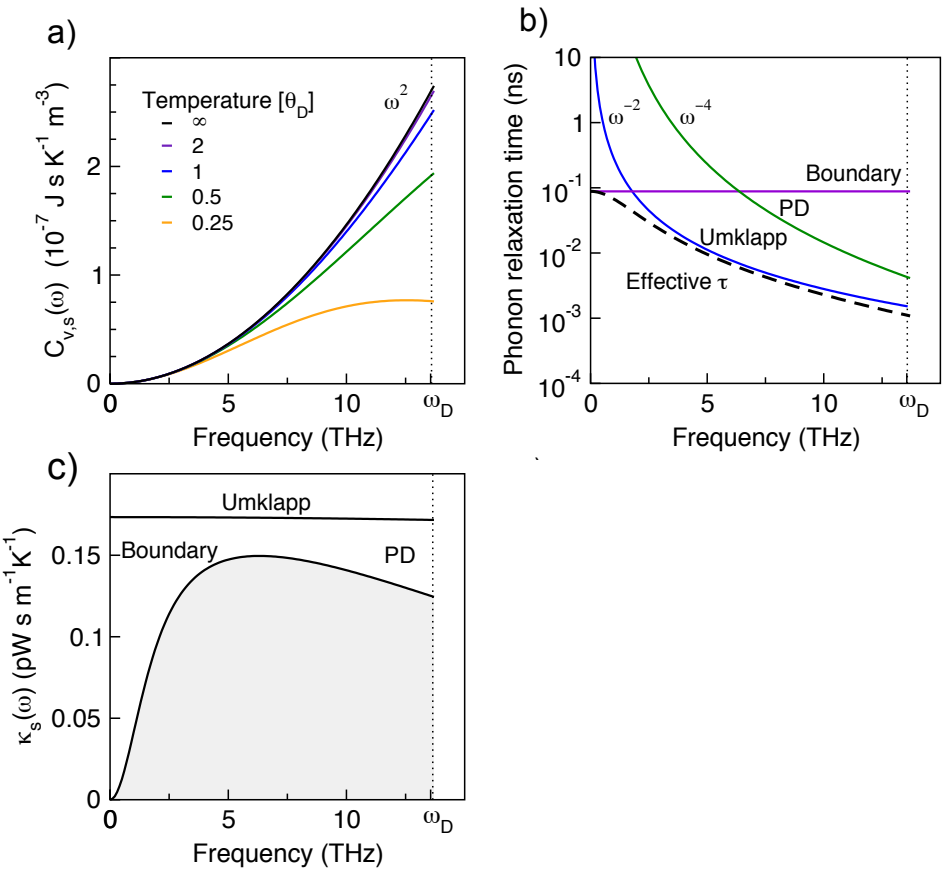

Figure 1.8: (a) Spectral Debye heat capacity approaches ω^2 dependence at high temperatures. (b) Frequency dependence of common scattering mechanisms. (c) Top curve: spectral thermal conductivity (assuming $\nu_g(\omega) = \nu_s$ and $T >> \theta_D$) when τ_U limits transport. Lower curve: spectral thermal conductivity when τ_B, and τ_{PD} are also accounted for.

compounds PbTe and PbSe in the context of Eq. 1.8. While heavier, softer PbTe has a lower group velocity than PbSe, the larger Grüneisen parameter of PbSe leads to similarly low κ_L [105].

$$\tau_U(\omega) = \frac{(6\pi^2)^{1/3}}{2} \frac{\bar{M}\nu_g\nu_p^2}{k_B V^{1/3}\gamma^2\omega^2 T} \tag{1.8}$$

Boundary scattering in polycrystalline materials with grain size d can be estimated from Eq. 1.9 [106, 107]. This scattering mechanism is particularly effective in nanostructured materials such as nanowires, thin films, and nanocomposites [22, 87, 88, 89]. In Zintl compounds, boundary scattering has only been employed, unintentionally, in

$SrZnSb_2$, which was found by transmission electron microscopy to contain numerous stacking faults [108].

$$\tau_B = \frac{d}{\nu_g} \tag{1.9}$$

Scattering by point defects arises from both mass and strain contrast within the lattice. Point defect scattering has been successfully employed in both thermoelectic materials ($Si_{1-x}Ge_x$), and in thermal barrier coatings such as yttria stabilized zirconia [1, 91]. Among Zintl materials, this strategy has been very successful in reducing κ_L in alloyed AM_2Sb_2 compounds (A = Ca, Eu, Yb, and M = Mn, Zn, Cd) [32, 109, 110, 40] and in $Yb_9Mn_{4+x}Sb_9$, which contains interstitial Mn [68]. In the simple case of alloying on a single crystallographic site, τ_{PD} is given by Eq. 1.10. Here, f_i is the fraction of atoms with mass m_i and radius r_i that reside on a site with average mass and radius $\bar{m}$ and $\bar{r}$, respectively [111, 98].

$$\tau_{PD}^{-1} = \frac{V\omega^4}{4\pi\nu_p^2\nu_g}\left(\sum_i f_i\left(1-\frac{m_i}{\bar{m}}\right)^2 + \sum_i f_i\left(1-\frac{r_i}{\bar{r}}\right)^2\right) \tag{1.10}$$

The scattering mechanisms discussed above target different populations of phonons, as shown in Figure 1.8b. Umklapp and point defect scattering target high frequency phonons, while boundary scattering is often the dominant scattering mechanism at low frequencies. In concert, these scattering mechanisms lead to an effective τ shown by the dashed line.

The frequency dependence of κ_L can be used to determine which phonons are critical to heat transport. The integrand of Eq. 1.4 is commonly referred to as the spectral thermal conductivity, $\kappa_s(\omega) = C_s(\omega)\nu_g(\omega)^2\tau(\omega)$. In a defect-free crystal at high temperatures, the ω^2 dependence of $C_s(\omega)$ is offset by the ω^{-2} dependence of Umklapp scattering, resulting in the frequency-independent $\kappa_s(\omega)$ shown in Fig. 1.8(c). Integrating over the phonon spectrum yields the classic expression for τ_U-limited κ_L given in Eq. 1.11 [94, 103].

$$\kappa_U = \frac{(6\pi^2)^{2/3}}{4\pi^2}\frac{\bar{M}\nu_s^3}{TV^{2/3}\gamma^2} \tag{1.11}$$

This simple expression is commonly invoked to explain high temperature transport,

and yields reasonable estimates for κ_L in materials with low mass contrast and simple crystal structures. In most materials however, boundary and point defect scattering are also significant, resulting in a highly frequency dependent $\kappa_s(\omega)$. The impact of boundary and point defect scattering on κ_L can be readily visualized as the difference in area between the top and bottom curves of Fig. 1.8(c).

1.4.3 Thermal Conductivity in Complex Systems

The following sections consider material systems with phonon dispersions that are progressively more complex than a simple Debye model. Complex phonon dispersions influence κ_L by (a) changing the states available for Umklapp scattering and (b) leading to highly frequency-dependent phonon velocities, as $\nu_g(\omega) = d\omega/dk$ [112, 81, 7].

Use of a simple Born-von Kármán (BvK) model allows us to visualize how the crystal structure determines the phonon dispersion. The 1-dimensional BvK model describes the lattice as a chain of atoms connected by springs with harmonic restoring forces [97, 98]. Figure 1.7 compares the Debye and BvK dispersions for the simple case of a monatomic chain [113].

High Mass Contrast The trend between high mass contrast and low lattice thermal conductivity has been clearly demonstrated by Slack [7]. Figure 1.9 reveals that the experimental κ_L of rock salt compounds is dramatically overestimated by the Debye model (κ_U) when mass contrast is high (e. g. BaO, mass ratio of 8.6).

The relationship between mass contrast and κ_L can be understood by examining the BvK phonon dispersions for a diatomic chain with varying mass ratio, $m_1 : m_2$ (Figure 1.10a). When the mass ratio is low, the Debye model's assumption of a constant phonon velocity appears reasonable. However, this assumption breaks down as the mass ratio increases and the optical branch flattens [114]. When τ is limited by Umklapp scattering, the spectral thermal conductivity, $\kappa_s(\omega)$, is proportional to $\nu_g(\omega)^2$. Figure 1.10b shows the dramatic reduction in $\nu_g(\omega)^2$, and thus κ_L, associated with the flattening of the optical modes with increasing mass contrast. Although not

accounted for here, changes to the phonon dispersion may also influence the available states for scattering events, leading to changes in the spectral mean free paths.

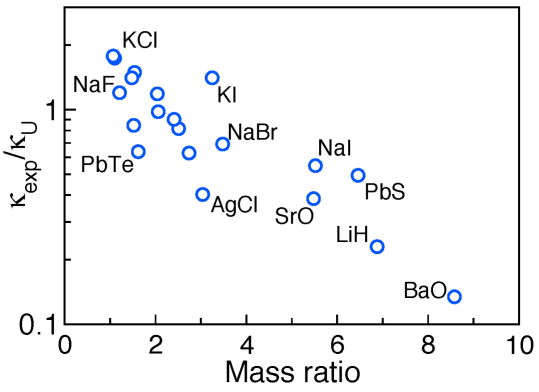

Figure 1.9: Calculated κ_U (Eq. 1.11) significantly overestimates experimental κ_L in rock salt compounds with high mass contrast at $T = \theta_D$. Values for θ_D, γ and κ_L were obtained from Ref. [7]

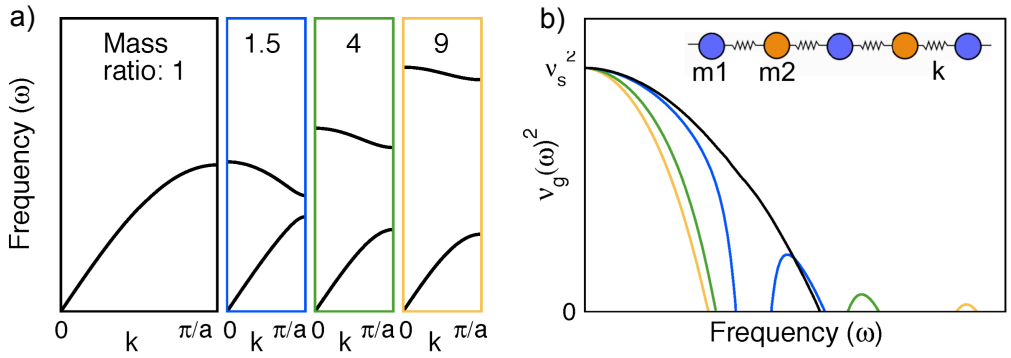

Figure 1.10: (a) As mass contrast increases in a diatomic chain, (average mass, ν_s held constant) the optical mode flattens and the gap increases. (b) The reduction of κ_L due to mass contrast can be judged from the area beneath the $\nu_g(\omega)^2$ curves.

Complex Primitive Cells Much like the high mass contrast rock-salt compounds, it has been argued that compounds with a large number of atoms (N) in the primitive unit cell have low κ_L due to low velocity optical modes [7, 101]. Classic examples of high-N compounds with low κ_L include $Y_3Al_5O_{12}$ (N=80), β-Boron (N=105), and YB_{68} (N=402) [7, 118]. More recently, similar trends have been observed in promising

Table 1.1: Room temperature κ_L in materials with a large number of atoms (N) per primitive cell.

Material	N	κ_L (300 K) W/mK	Ref.
$LaPO_4$	24	2.5	[115]
$W_3Nb_{14}O_{44}$	61	1.8	[115]
$LaMgAl_{11}O_{19}$	64	1.2	[116]
$La_2Mo_2O_9$	624	0.7	[115]
α $Al_{14.7}Mn_{3.5}Si_{1.8}$	138	1.5	[117]
$Ca_5Al_2Sb_6$	26	1.5	[10]
Ca_3AlSb_3	28	1.6	[5]
$Yb_{11}Sb_{10}$	42	0.8	[47]
$Yb_{11}In_1Sb_9$	42	0.8	[48]
$Yb_9Mn_{4.2}Sb_9$	44	0.5	[68]
$Ba_8Ga_{16}Ge_{30}$	54	1.1	[6, 59]
$Yb_{14}AlSb_{11}$	104	0.6	[21]

materials for thermoelectrics and thermal barrier coatings (Table 1.1) [4, 115].

To further investigate the trend between low κ_L and N, we have compiled the properties of materials for which all of the quantities in Eq. 1.11 are known experimentally. Many materials with applications for thermal barrier coatings have not been included, as their Grüneisen parameters are not reported in the literature. We consider the ratio of measured κ_L to that predicted by κ_U (Eq. 1.11). Figure 1.11 shows that for simple structures, good agreement between κ_U and experimental κ_L can sometimes be obtained. However, κ_L of more complex materials are consistently over-estimated by the simple κ_U model.

The trend between low κ_L and structural complexity can be qualitatively rationalized by a BvK model. Figure 1.12a shows phonon dispersions for 1D chains with N-atom cells. As N increases, the phonon dispersion "folds in" on itself, resulting in $N-1$ optical modes with low $\nu_g(\omega)$. Thus, in complex materials, the vast majority of heat is trapped in flat, low velocity optical modes, which are not accurately described by a Debye model. Figure 1.12b emphasizes the reduction of $\nu_g(\omega)^2$ (and thus $\kappa_s(\omega)$ at the limit of Umklapp scattering), with increasing structural complexity. Zintl compounds in particular benefit from this mechanism. Compared with other bulk thermoelectric materials, Zintl compounds have larger unit cells and exhibit some of

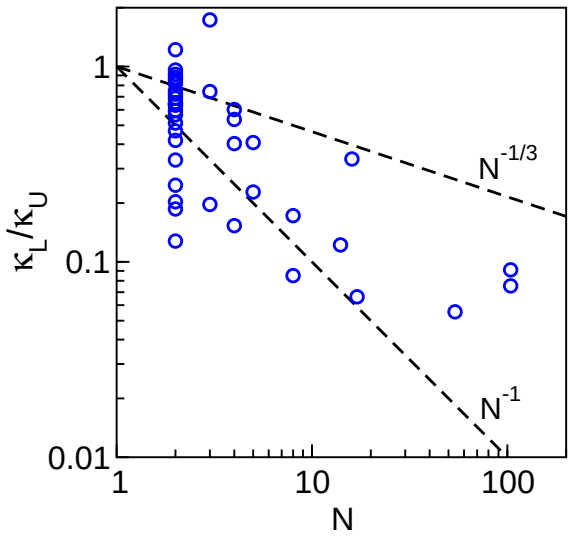

Figure 1.11: For materials with many atoms per primitive cell (N), Eq. 1.11 fails to predict the experimental κ_L. Data obtained from ref [8].

the lowest experimental lattice thermal conductivities [37].

A promising approach to modeling κ_L in complex materials, proposed by Toberer et al. [8], is to consider the acoustic contribution (κ_a) using a Debye model and the optical (κ_o) contribution using Cahill's model for disordered structures. To determine the maximum frequency of the acoustic branch, ω_a, the equal partition of the heat capacity amongst the phonon modes ($C_{v,acoustic} = C_v/N$) is employed, yielding $\omega_a = \omega_D/N^{1/3}$ [101]. Values for ω_a can thus be obtained either from measurements of ν_s or θ_D. However, the various approaches to obtaining θ_D (e. g., low or high temperature heat capacity measurements or density of states from neutron experiments) can yield significantly different values [7, 119].

With ω_a determined, the acoustic contribution can be determined from Eq. 1.4 using the high temperature limit for the heat capacity. For τ limited by Umklapp scattering, $\kappa_a \propto N^{-1/3}$ (Eq. 1.12). If instead, boundary scattering is assumed to dominate transport, $\kappa_a \propto N^{-1}$ (Eq. 1.13). In practice, the experimental N-dependence in Figure 1.11(a) is between these bounds, and is consistent with the $N^{-2/3}$ dependence obtained by Slack [7].

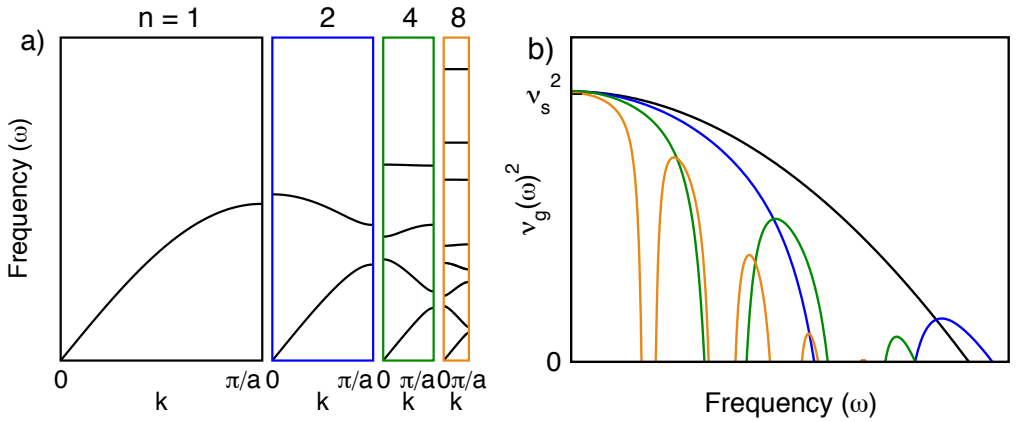

Figure 1.12: (a) Phonon dispersions for ball and spring chains with increasing number of atoms per unit cell (constant ν_s). (b) A dramatic decrease in $\nu_g(\omega)^2$, and thus $\kappa_s(\omega)$, is found with increasing N. For $N = 4$ and 8, the high frequency optical modes are not visible on a linear plot due to the extreme flatness of these modes.

$$\text{Umklapp: } \kappa_a = \frac{(6\pi^2)^{2/3}}{4\pi^2} \frac{\bar{M}\nu_s^3}{TV^{2/3}\gamma^2} \left(\frac{1}{N^{1/3}}\right) \tag{1.12}$$

$$\text{Boundary: } \kappa_a = \frac{k_B \nu_s \, d}{V} \left(\frac{1}{N}\right) \tag{1.13}$$

Traditional models for κ_L in materials with complex structures ignore the optical branches entirely. However, at the amorphous limit ($N = \infty$), the acoustic contribution (κ_a) approaches zero, whereas in reality, glasses still possess finite thermal conductivity. For a lower bound to the optical contribution to thermal conductivity (κ_o), one can look to Einstein's treatment of heat transport as the diffusion of heat between atomic oscillators. Cahill has extended this theory to larger oscillating units, for which $l_{glass} = \lambda/2$, or equivalently $\tau_{glass}(\omega) = \pi/\omega$ [120, 121]. Note that $l_{glass} = \lambda/2$ is still much larger than the average distance between atoms [71]. In this model, the speed of sound is used to describe the coupling between oscillators. The optical contribution to κ_L can thus be estimated by evaluating Eq. 1.4 using τ_{glass}, the high temperature limit of the heat capacity, and lower and upper integration limits of $\omega_D/N^{1/3}$ and ω_D respectively. The resulting expression for κ_o is given by Eq. 1.14.

$$\kappa_o = \frac{3k_B\nu_s}{2V^{2/3}}\left(\frac{\pi}{6}\right)^{1/3}(1-\frac{1}{N^{2/3}}) \tag{1.14}$$

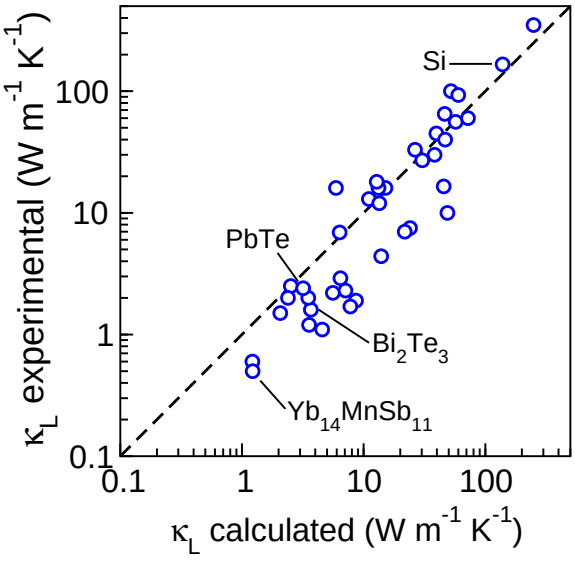

Figure 1.13: Success of κ_a+κ_o in predicting the lattice thermal conductivity of selected materials (see supplementary Table 1). Here, κ_a includes both Umklapp scattering and a boundary scattering term of 1 μm (Eq. 1.7).

Having developed expressions for both the acoustic and optical phonons, we can re-evaluate the calculated thermal conductivity of the materials presented in Fig. 1.11. We estimate κ_a in a manner analogous to Eq. 1.12 and 1.13, except that here we assume that both Umklapp and boundary scattering (d =1 μm) limit transport. Summing κ_a and κ_o (Eq. 1.14) yields good agreement with the experimental κ_L across two orders of magnitude, as illustrated by Fig. 1.13.

While computational methods may eventually be able to accurately predict thermal conductivity in complex materials, this simple model provides valuable intuition. A comparison of $Yb_{14}MnSb_{11}$ and PbTe is particularly revealing. As the bulk properties of these two materials are extremely similar, (θ_D, $\bar{M}$, C_v, γ, see Supplementary Table 1) κ_U suggests that PbTe should have a slightly lower κ_L than $Yb_{14}MnSb_{11}$. However, calculations accounting for the difference in N predict that the κ_L of $Yb_{14}MnSb_{11}$ (N=104) should be a factor of 3 lower than that of PbTe

(N=2) at room temperature. Indeed, the experimental κ_L of $Yb_{14}MnSb_{11}$ and PbTe at 300 K are 0.6 and 2 W m^{-1} K^{-1}, respectively.

This model confirms that structural complexity can be used to reduce lattice thermal conductivity by causing glass-like thermal transport across much of the phonon spectrum, explaining the exceptionally low thermal conductivity found in many Zintl compounds. Although structural complexity remains underutilized in the development of new thermoelectric materials, the recent emergence of Zintl phases with excellent thermoelectric performance highlights the value of this approach.

1.5 Summary of Research

An ideal thermoelectric material has a narrow band gap (< 1 eV), tunable electronic properties, low lattice thermal conductivity, and thermal stability at the temperature of interest. Zintl phases, with their complex yet malleable chemistry, exhibit precisely the characteristics desired for thermoelectric applications. However, compared with the number of known Zintl compounds, very few have been investigated as thermoelectric materials. Thus, an exciting aspect of this field is the vast potential for future discovery of new thermoelectric materials.

From this huge pool of compounds, we selected a class of hitherto uninvestigated antimonides that share a common structural motif: anionic moieties resembling infinite chains of MSb$_4$ tetrahedra. The compounds discussed in this thesis include $Ca_5M_2Sb_6$ (where M = Al, Ga, or In), $Sr_5Al_2Sb_6$, Ca_3AlSb_3, Sr_3GaSb_3, and Sr_3AlSb_3, each of which forms a distinct, but related, structure type. This is a particularly attractive group of Zintl compounds for reasons both fundamental and applied: on a fundamental level, there is a need to explore Zintl compounds which structurally bridge between the isolated (0-D) covalent moieties of $Yb_{14}MnSb_{11}$ and the covalent slabs (2-D) of AZn_2Sb_2 (A = Ca, Sr, Yb, Eu). The variety of 1D chain structures in the $A_5M_2Pn_6$ and A_3MPn_3 compounds enables such comparisons. Also, these materials allow further exploration of trends in band mass, mobility, and lattice thermal conductivity in Zintl antimonides. From an application perspective, good thermoelec-

tric performance in $Ca_5Al_2Sb_6$ and Ca_3AlSb_3 would be attractive, as the constituents are reasonably nontoxic and abundant.

This thesis describes the synthesis, characterization, and computational study of the "chain-forming" Zintl phases. All of the samples were prepared using a synthesis method based on milling and hot pressing of the constituent elements, and the electronic and thermal transport properties of the samples were characterized to high temperature. Density functional calculations were performed by our collaborators Espen Flage-Larsen, Gregory Pomrehn, and Yoshiki Takagiwa. The following chapters are divided by structure type. The studies within each chapter revolve around characterizing and optimizing the figure of merit of each compound via iso-electronic substitutions to subtly tune the transport properties, or by doping to increase the carrier concentration. The improved understanding of the structure-property relationships in Zintl compounds gained from these results may ultimately help to guide future work on Zintl phase thermoelectrics.

Chapter 2

Experimental Methods

2.1 Synthesis

The chain-forming Zintl compounds discussed in this thesis were first synthesized by Cordier et al. by heating the elements in argon-filled, sealed alumina tubes at temperatures in excess of 1200 K, and then cooled to room temperature [13, 9, 122, 123, 12, 11]. The solidified melts typically contained small crystals of the desired ternary phase together with a high fraction of secondary phases. In the current work, we instead employ a solid-state method, in which high energy ball milling of the elements is used to reduce the diffusion distance, and the formation and consolidation of the final ternary phase occurs during hot pressing. This method has already been established for the synthesis of several thermoelectric materials, including La_3Te_4 [124], $Ba_8Ga_{16}Ge_{30}$ [6] and the Zintl phase $Yb_{14}MnSb_{11}$ [44]. The general milling and pressing procedure used for those materials was adapted for the compounds in this work.

Stoichiometric quantities of high purity elemental precursors were manually cut into small (1-3 mm) pieces in an argon-filled glove box. The source and purity (metals basis) of the elemental precursors used for each study are listed in Table 2.1. In the glove box, the elements were loaded into stainless-steel vials with two 0.5 inch diameter stainless-steel balls and sealed. In compounds containing either In or Ga, an additional step was added: prior to ball milling, a binary GaSb or InSb precursor phase was formed by melting the elements in evacuated quartz tubes for 12 hours

(at 1073 K or 873 K, respectively) and then quenching in water. The relevant binary phase was then crushed and loaded into the steel milling vial along with the elements. The stoichiometric mixtures were then ball-milled for 1 hour (in the absence of solvents) using a high energy SPEX Sample Prep 8000 Series Mixer/Mill. Exceptions include Mn-doped $Ca_5Al_2Sb_6$, Na- and Zn-doped Ca_3AlSb_3, and Zn-doped Sr_3GaSb_3, which were milled for 90 minutes.

Table 2.1: The purity (% metals basis) and geometry of the elemental precursors are given below. Except for Ca dendrites from Sigma-Aldrich, all elements were sourced from Alfa-Aesar.

	Ref.	*A* (Ca, Sr)	*M* (Al, Ga, In)	Sb	dopant (Na, Zn, Mn)
$Ca_{5-x}Na_xAl_2Sb_6$	[10]	99.99 dendrite	99 shot	99.5 lump	99.95 cube
$Ca_5Al_{2-x}Zn_xSb_6$	[125]	99.99 dendrite	99 shot	99.5 lump	99.99 shot
$Ca_5Al_{2-x}Mn_xSb_6$	[64]	99.99 dendrite	99 shot	99.5 lump	99.95 powder
$Ca_5Ga_{2-x}Zn_xSb_6$	[126]	99.99 dendrite	99.99 shot	99.9999 shot	99.99 shot
$Ca_5In_{2-x}Zn_xSb_6$	[127]	99.99 dendrite	99.999 shot	99.9999 shot	99.99 shot
$Sr_5Al_2Sb_6$		99 lump	99 shot	99.9999 shot	
$Ca_{3-x}Na_xAlSb_3$	[5]	99.99 dendrite	99 shot	99.5 lump	99.95 cube
$Ca_3Al_{1-x}Zn_xSb_3$	[128]	99.9 dendrite	99 shot	99.9999 shot	99.99 shot
$Sr_3Ga_{1-x}Zn_xSb_3$	[129]	99 lump	99.99 shot	99.9999 shot	99.99 shot)
$Sr_3Al_{1-x}Zn_xSb_3$	[65]	99 lump	99 shot	99.9999 shot	99.99 shot

The resulting fine powder was consolidated by hot-pressing under flowing argon in high-density graph-ite dies (manufactured by POCO) with 12 mm inner diameter. Samples were heated slowly (2-3 hours) to the maximum temperature (T_{max}) and held for several hours (t_{max}) to consolidate the powder and allow for the formation of the desired ternary phase. The pressure was increased to the maximum value

(P_{max}) only after T_{max} was reached. Samples containing Ga or In were first held at an initial reduced load (P_i) and temperature (T_i) for time t_i, to ensure complete reaction of any low-melting-temperature phases in the milled powder, after which the temperature and pressure were increased to the maximum values over approximately 1 hour. Finally, a slow (between 2-3 hours), stress-free cool down was used to minimize internal stress in the samples. The pressures, temperatures, and durations used during hot pressing are outlined in Table 2.2 for each compound. The consolidated samples were sliced into 1 mm thick, 12 mm diameter disks for thermal and electronic transport measurements.

Table 2.2: Hot pressing parameters.

	Ref.	T_i (K)	P_i (MPa)	t_i (h)	T_{max} (K)	P_{max} (MPa)	t_{max} (h)
$Ca_{5-x}Na_xAl_2Sb_6$	[10]	-	-	-	973	110	2
$Ca_5Al_{2-x}Zn_xSb_6$	[125]	-	-	-	873	40	5
$Ca_5Al_{2-x}Mn_xSb_6$	[64]	-		-	1073	110	4
$Ca_5Ga_{2-x}Zn_xSb_6$	[126]	873	80	2	973	110	3
$Ca_5In_{2-x}Zn_xSb_6$	[127]	773	80	2	973	110	3
$Sr_5Al_2Sb_6$		-	-	-	110	110	3
$Ca_{3-x}Na_xAlSb_3$	[5]	-	-	-	973	110	2
$Ca_3Al_{1-x}Zn_xSb_3$	[128]	-	-	-	973	40	2
$Sr_3Ga_{1-x}Zn_xSb_3$	[129]	873	80	1.5	973	110	2
$Sr_3Al_{1-x}Zn_xSb_3$	[65]	-	-	-	1073	110	3

2.2 Characterization

Chemical Characterization The phase purity of the samples was characterized primarily using X-ray diffraction (XRD), scanning electron microscopy (SEM), and energy dispersive spectroscopy (EDS). XRD was performed on polished slices using a Philips PANalytical XPERT MPD diffractometer operated at 45 kV and 40 mA with CuKα radiation. In most cases, Rietveld analysis was performed using Philips X'Pert Plus software. However, for both Zn-doped Ca_3AlSb_3 and Sr_3GaSb_3 samples, Pawley refinements were performed by Wolfgang Zeier using TOPAS Academic V4.1 [130].

SEM and EDS analysis was performed on the consolidated materials using a Zeiss 1550 VP SEM. Analysis of the polished surfaces was used to confirm the composition and amount of secondary phases, while fracture surfaces were used to estimate the grain size. To quantify the incorporation of Na in the Na-doped Ca_3AlSb_3 system, electron microprobe analysis (EMPA) with wavelength dispersive spectroscopy (WDS) was carried out by Teruyuki Ikeda using a JEOL JXA - 8200 system. Elemental Al and Sb, $NaAlSi_3O_8$, and $CaAl_2Si_2O_8$ were used for the Al, Sb, Na, and Ca standards, respectively.

Electronic Transport Measurements The electronic and thermal transport properties were characterized under dynamic vacuum from room temperature up to maximum temperatures ranging from 973-1073 K. The maximum temperature is dependent on the thermal stability of each compound. The Hall coefficients and resistivity were measured simultaneously by relying on the Van der Pauw technique to obtain resistivity values, and employing press-assisted tungsten contacts.[131]. Two different measurement systems were used in these studies: a system at Caltech with a 2 Tesla field and a maximum temperature of 873 K, and a system at the Jet Propulsion Laboratory (JPL) with a 1 Tesla field, and a higher maximum temperature of 1373 K. From the Hall coefficients, R_H, the Hall carrier concentration, n_H, was calculated from $R_H = -1/en_H$, assuming a single carrier type. The Hall mobility was determined from the measured resistivity and carrier concentration using the relation μ_H=$1/n_H e\rho$ The Seebeck coefficients were also measured on two different system, both of which measure the Seebeck coefficient by allowing the temperature gradient across the sample to oscillate between $\pm$10 K while maintaining a constant average temperature at each set point. The Seebeck measurement system at Caltech employs chromel-Nb thermocouples and resistive heaters [132], and the system at JPL uses W-Nb thermocouples and a light-pipe heating system [133]. The latter system was used for the following studies: Na-doped $Ca_5Al_2Sb_6$, Zn-doped $Ca_5In_2Sb_6$, Na-doped Ca_3AlSb_3, and Zn-doped Sr_3GaSb_3. The remaining studies used the Caltech system.

Thermal Transport Measurements The thermal conductivity, κ_L was calculated using $\kappa_L = DC_P d$, where D is thermal diffusivity, C_P is the heat capacity, and d is density. A Netzch LFA 457 was used to measure the thermal diffusivity using the laser flash method. The heat capacity was estimated using the Dulong Petit value, and the density was determined geometrically. Although it is common to use the Dulong Petit value at temperatures above θ_D, this can lead to a 10-20% underestimate of the true C_p and therefore of the thermal conductivity, particularly at high temperatures. Longitudinal and transverse ultrasonic measurements were performed at room temperature to obtain the longitudinal and transverse sound velocities. Honey was used as a coupling agent. A Panametrics NDT 5800 pulser/receiver was employed with a Tektronix TDS 1012 digital oscilloscope; these measurements were performed in W. Johnson's laboratory at Caltech.

Optical Measurements Optical absorption measurements were performed by Zach Gibbs to characterize the electronic band gap in $Ca_5M_2Sb_6$ samples (M = Al, Ga, and In). The measurements were performed at room temperature using diffuse reflectance infrared Fourier transform spectroscopy (DRIFTS), using a Nicolet 6700 FTIR spectrophotometer (Thermo Scientific) equipped with a Praying Mantis Diffuse Reflection accessory (Harrick) and DTGS detector and KBr beamsplitter. The spectra were analyzed by first referencing the raw intensity to that obtained from measuring a mirror, then calculating the Kubelka Munk function $F(R) = \frac{k}{S} = \frac{(1-R_\infty)^2}{2R_\infty}$ where k is the absorption coefficient, S is the scattering coefficient, and R_∞ is the diffuse reflectance from an optically thick layer [134]. Direct band gaps were obtained by plotting $(F(R)\hbar\omega)^2$ vs. $\hbar\omega$, where $\hbar\omega$ is the incoming photon energy, and extrapolating the slope of the absorption edge to $(F(R)\hbar\omega)^2 = 0$ [135]. While care was taken to avoid sample oxidation, O-H stretching absorption was observed in some spectra ($\sim$ 0.43 - 0.45 eV).

2.3 Analysis of Transport Properties

To analyze the electronic and thermal transport data, solutions to the Boltzmann transport equation within the relaxation time approximation were used, assuming a single, parabolic band ($E(\vec{k}) \propto \frac{\hbar^2\vec{k}^2}{2m^*}$). This model is frequently applied to bulk thermoelectric materials, and is referred to simply as a single parabolic band (SPB) model in the literature. The SPB model is most accurate when used to approximate electronic transport dominated by a single carrier type, and when the Fermi level is in a relatively parabolic and isotropic region of the band structure.

In the following work, an SPB model is used to estimate the effective mass (m^*) using Eq. 2.1 and 2.2, which relate the Seebeck coefficient to the carrier concentration via the chemical potential (η). Here, λ is a constant determined by the dominant electron scattering mechanism. In this work, acoustic phonon scattering is assumed, corresponding to $\lambda = 0$. The function $F_j(\eta)$ is the Fermi integral (Eq. 2.3), with ζ the reduced carrier energy. From Eq. 2.1, the experimental α obtained from a degenerately doped sample can be used to determine η. If n is known, m^* can then be estimated from Eq. 2.2. m^* can be used to predict the relationship between α and n for samples with varying dopant concentrations, assuming rigid band behavior. Note that in this model, m^* is equivalent to the the density of state effective mass, m^*_{DOS}, described above.

$$\alpha = \frac{k}{e}\left(\frac{(2+\lambda)F_{1+\lambda}(\eta)}{(1+\lambda)F_\lambda(\eta)} - \eta\right) \tag{2.1}$$

$$n = 4\pi\left(\frac{2m^*k_BT}{h^2}\right)^{3/2} F_{1/2}(\eta) \tag{2.2}$$

$$F_j(\eta) = \int_0^\infty \frac{\zeta^j d\zeta}{1+e^{\zeta-\eta}} \tag{2.3}$$

The carrier mobility is given as a function of chemical potential by Eq. 2.4. The intrinsic mobility, μ_o, is a fitting parameter obtained by solving Eq. 2.4 with the experimental Hall mobility, μ_H, and chemical potential.

$$\mu_H = \mu_o \frac{\pi^{1/2} F_\lambda(\eta)}{F_{1/2}(\eta)} \tag{2.4}$$

Eq. 2.5 gives the Lorenz number as a function of chemical potential. Here, the chemical potential is again obtained from Eq. 2.1 and the experimental α. This relationship is used to generate temperature-dependent Lorenz numbers for the calculation of electronic thermal conductivity, κ_e, using the Wiedemann-Franz relationship ($\kappa_e = LT/\rho$).

$$L = \frac{k^2}{e^2} \frac{3F_0(\eta)F_2(\eta) - 2F_1(\eta)^2}{F_0(\eta)^2} \tag{2.5}$$

Using the above expressions for $\alpha(\eta)$, $n(\eta)$, $\mu(\eta)$, and $L(\eta)$, and assuming a constant value for the lattice thermal conductivity, the figure of merit zT can be calculated as a function of chemical potential. This method is used to estimate an optimum carrier concentration for a given material at a given temperature.

2.4 Density Functional Theory

Density Functional calculations were performed by collaborators Espen Flage-Larsen, Gregory Pomrehn, and Yoshiki Takagiwa.

Density Functional calculations for Ca_3AlSb_3 and $Ca_5Al_2Sb_6$ were performed using the Vienna *Ab-initio* Simulation Package (VASP) [136, 137]. For the exchange and correlation the Perdew-Burke-Enzerhof generalized gradient approximation (PBE-GGA) [138] functional was used in the projector augmented-wave (PAW) formalism [139]. The experimental lattice constants and atom positions reported by Cordier et al. were used as input [12, 13]. For Ca_3AlSb_3, a k-point grid of 5×15×5 and an energy cutoff of 450 eV were necessary to converge the total energy to within a few meV. For $Ca_5Al_2Sb_6$, the k-point grid was 4×4×12 and the energy cutoff was 400 eV. The electron density difference (EDD) surfaces presented for Ca_3AlSb_3 are the difference between the electron density of the crystal and the overlapping, non-bonding, atomic electron densities (procrystal) [140].

Calculations for the $Ca_5M_2Sb_6$ series (M = Al, Ga, In), Sr_3GaSb_3, Sr_3AlSb_3 and $Sr_5Al_2Sb_6$ were performed using the WIEN2K code [141] based on the full-potential linearized augmented plane-wave and local orbitals (FP-APW+LO) method under the generalized gradient approximation (GGA) as parameterized by Perdew, Burke, and Ernzerhof (PBE) [138]. The modified Becke-Johnson (TB-mBJ) [142] semi-local exchange potential, which has been shown to improve the band gap in *sp* bonded semiconductors [143], was used to produce the density of states and electronic dispersions. For comparison, additional calculations were performed for the $Ca_5M_2Sb_6$ compounds using the Vienna *ab initio* simulation package (VASP) [137] with the projector-augmented-wave (PAW) [144, 139] using hybrid functionals under the HSE06 [145] scheme.

For $Ca_5M_2Sb_6$ compounds, a plane wave basis cutoff of $R_{mt}K_{max} = 9$ was used, in terms of the smallest muffin tin radius and maximum plane wave vector respectively. Muffin tin radii were 2.5 a.u. for Ca, Ga, and In and 2.4 a.u. for Al and Sb. For Sr_3GaSb_3, $R_{mt}K_{max}$ was 9 and the muffin tin radii were 2.4 a.u. for Sr and 2.5 a.u. for both Ga and Sb. Total energy convergence was achieved in the self consistent calculations with a shifted 6x4x6 k-point mesh, which reduced to 36 symmetrically unique k-points. Calculations for Sr_3AlSb_3 used $R_{mt}K_{max} = 7$, muffin tin radii of 2.5 a.u. for Sr and 2.37 a.u. for both Al and Sb and a 32x32x15 k-point mesh, which reduced to 2176 symmetrically unique k-points. Calculations for $Sr_5Al_2Sb_6$ used $R_{mt}K_{max} = 7$, muffin tin radii of 2.5 a.u. for Sr and 2.49 a.u. for both Al and Sb and a 9x11x8 k-point mesh. For $Ca_5M_2Sb_6$ and Sr_3GaSb_3 calculations were performed at the theoretical ground state lattice parameters as determined by structural minimization of the unit cell. For Sr_3AlSb_3 and $Sr_5Al_2Sb_6$, the experimental lattice parameters were used. In all calculations, atomic positions were relaxed to converged forces below 0.025 eV/Å on each atom.

Chapter 3

Thermoelectric Properties of $Ca_5M_2Sb_6$ (M = Al, Ga, or In)

3.1 Introduction

$Ca_5M_2Sb_6$ Zintl compounds (where M = Al, Ga, or In) belong to a larger group of isostructural compounds with the $Ca_5Ga_2As_6$ structure type [13, 9]. The structure of $Ca_5Al_2Sb_6$ is shown in figure 3.1a. The anionic sub-structure of $Ca_5M_2Sb_6$ consists of corner-linked chains of MSb_4 tetrahedra oriented along the c-axis, which are, in turn, connected by Sb-Sb bonds to form infinite, 1-dimensional, ladder-like moieties (Figure 3.1b).

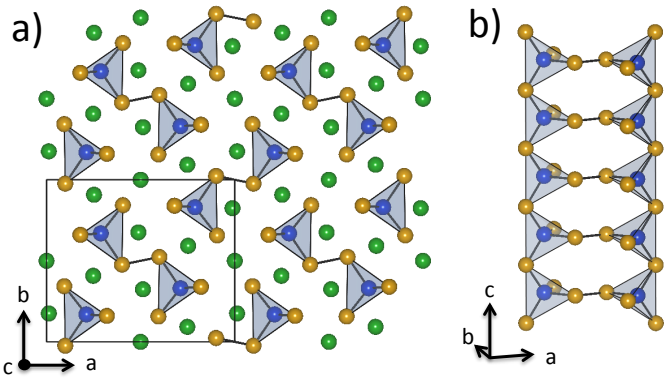

Figure 3.1: (a) The orthorhombic unit cell of $Ca_5Al_2Sb_6$ (*Pbam*) viewed down the [001] direction. (b) Adjacent tetrahedral chains, oriented along the [001] axis, are connected by Sb-Sb bonds. Sb atoms are orange, Ca are green, and Al are blue.

In $Ca_5M_2Sb_6$ compounds, the anionic building block can be written as $(M_2Sb_6)^{10-}$

while the five Ca^{2-} atoms situated between the chains provide overall valence balance. Within the anionic structure, the Sb-Sb bonds are clearly covalent, whereas the M-Sb bonds are less well defined. The MSb_4 tetrahedra can be treated as either covalently or ionically bonded and still yield overall charge balance; a covalent description yields two Sb^{1-} bridging across the chains, two Sb^{1-} shared between two tetrahedra, and two Sb^{2-} that are bonded only to one M atom, while the two M atoms have four covalent bonds and a formal valence of -1. In contrast, an ionic description yields two Al^{3+}, while a formal valence state of -2 is assigned to the two bridging Sb. The two Sb shared between two tetrahedra and the two Sb bonded to only an M atom each have a valence state of -3.

In addition to the three $Ca_5M_2Sb_6$ compounds, the $Ca_5Ga_2As_6$ structure type is also formed by $Sr_5In_2Sb_6$, $Ba_5In_2Sb_6$, and one rare-earth based compound, $Eu_5In_2Sb_6$. The transport properties of $Eu_5In_2Sb_6$ have been previously investigated by S. M. Park et al. [146]. Undoped samples showed a decreasing resistivity with temperature, indicative of carrier activation across a band gap. Alloying Zn onto the In site successfully yielded a sample with metallic transport properties. However, the thermal properties and figure of merit were not reported.

In $A_5M_2Pn_6$ compounds with Bi on the Pn site ($Ca_5Al_2Bi_6$, $Sr_5In_2Bi_6$, and $Ba_5Al_2Bi_6$ [12]) or Yb on the cation site ($Yb_5M_2Sb_6$, M = Al, Ga, In [72, 147]), an alternate packing arrangement of the anionic "ladders" leads to a distinct, but closely related structure type. Of compounds with this alternate structure type, the thermoelectric properties of $Yb_5Al_2Sb_6$ and $Yb_5In_2Sb_6$ have been investigated [72, 147]. In both cases, metallic behavior was observed for nominally undoped materials. Optical measurements of $Yb_5In_2Sb_6$ yielded a band gap between 0.2-0.4 eV.[147]. If a band gap is indeed present, the observed metallic behavior may arise from deviations from the charge-balanced stoichiometry, similar to that observed in AZn_2Sb_2 compounds.

The following sections describe the chemical characterization, thermal and electronic transport properties, and calculated electronic structures of $Ca_5M_2Sb_6$ compounds. Section 3.2 investigates the influence of the triel element (M) on the chemistry and intrinsic transport properties of the $Ca_5M_2Sb_6$ system. The optimization of

the figure of merit of $Ca_5Al_2Sb_6$ by doping with Na^{1+} on the Ca^{2+} site is presented in Section 3.3.1, while the results of doping with Zn and Mn are given in sections 3.3.2 and 3.3.3, respectively. Zn-doped $Ca_5Ga_2Sb_6$ and Zn-doped $Ca_5In_2Sb_6$ are described in Sections 3.4 and 3.5 respectively.

3.2 Influence of the Triel Elements (M = Al, Ga, In) on the Properties of $Ca_5M_2Sb_6$

Introduction The ambivalent M-Sb bonding description, resulting from the intermediate electronegativity of the M atom in A-M-X Zintl compounds (where M is a triel element or transition metal and X is a main group 3 or 4 element), often makes it difficult to predict the role of the M site in the chemical and transport properties of such materials. There have been several studies on the effect of isoelectronic substitutions on the M-site in Zintl compounds, many of which demonstrate the ability of such substitutions to tune, and even optimize, thermoelectric properties. This is a frequently used strategy in $A_{14}MSb_{11}$ and AM_2Sb_2 compounds, as well as in $A_8M_{16-x}X_{30+x}$ clathrates [43, 109, 148, 149]. However, in most studies, isoelectronic substitutions are used to effectively dope the material by adjusting the thermodynamically stable charged defect concentration. This makes it difficult to separate the first order effects of varying the carrier concentration from the more subtle consequences arising from potential changes to the band structure. $Ca_5M_2Sb_6$ is an ideal system in which to study the effect of metal-site substitutions on transport properties, as the M-site can accommodate either Al, Ga, or In, and these substitutions have no effect on the small extrinsic carrier concentration that results from defects. Here, we investigate the $Ca_5M_2Sb_6$ series (M = Al, Ga, or In) using a combination of high temperature electronic and thermal measurements, optical measurements, and computational studies, with the goal of furthering our understanding of structure-property

relationships in ternary Zintl compounds.

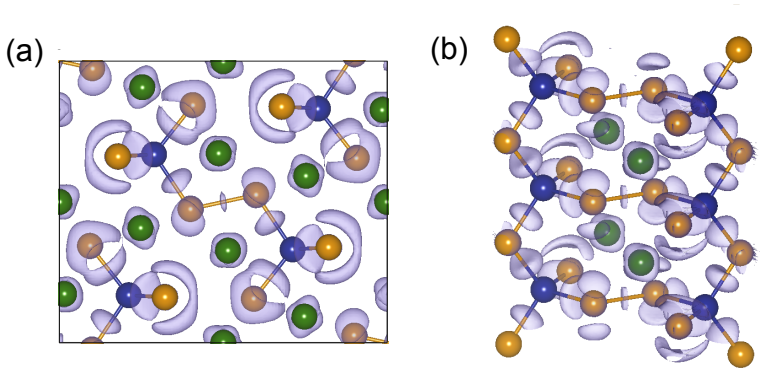

Figure 3.2: (a) Electron density difference isosurfaces show regions of charge accumulation in a $Ca_5Al_2Sb_6$ unit cell, and (b) along the $AlSb_4$ tetrahedral chains. Al atoms are blue, Sb in orange, and Ca in green.

Electronic structure calculations Density Functional calculations were performed to clarify the effect of the M-site (M = Al, Ga, and In) on the chemistry of $Ca_5M_2Sb_6$ compounds. As the Zintl-Klemm concept allows the M atoms in $Ca_5M_2Sb_6$ to be treated as either ionic charge donors *or* covalently bonded anions, the true bonding character remains unknown. To identify covalent bonds, an intuitive approach is to locate regions of increased electron density. We pursue this approach here by using electron density difference (EDD) maps. EDD maps were generated by subtracting super-positioned, non-interacting, atomic electron densities (procrystal) from the calculated electron density of $Ca_5Al_2Sb_6$. EDD isosurfaces of a single unit cell of $Ca_5Al_2Sb_6$ and a segment of its covalent ladder substructure are shown in Figure 3.2 (a) and (b), respectively. A large degree of charge accumulation occurs midway between the Al and Sb atoms, suggesting that these bonds have significant covalent character. Though not shown here, Ga-Sb and In-Sb bonds exhibit similar accumulation. Charge accumulation is also observed, to a lesser degree, midway between the Sb atoms comprising the Sb-Sb "ladder rungs." The more diffuse regions of charge build-up around the Sb atoms indicate unbonded electron lone pairs.

The density of states (DOS) of $Ca_5M_2Sb_6$ (M = Al, Ga, and In) compounds,

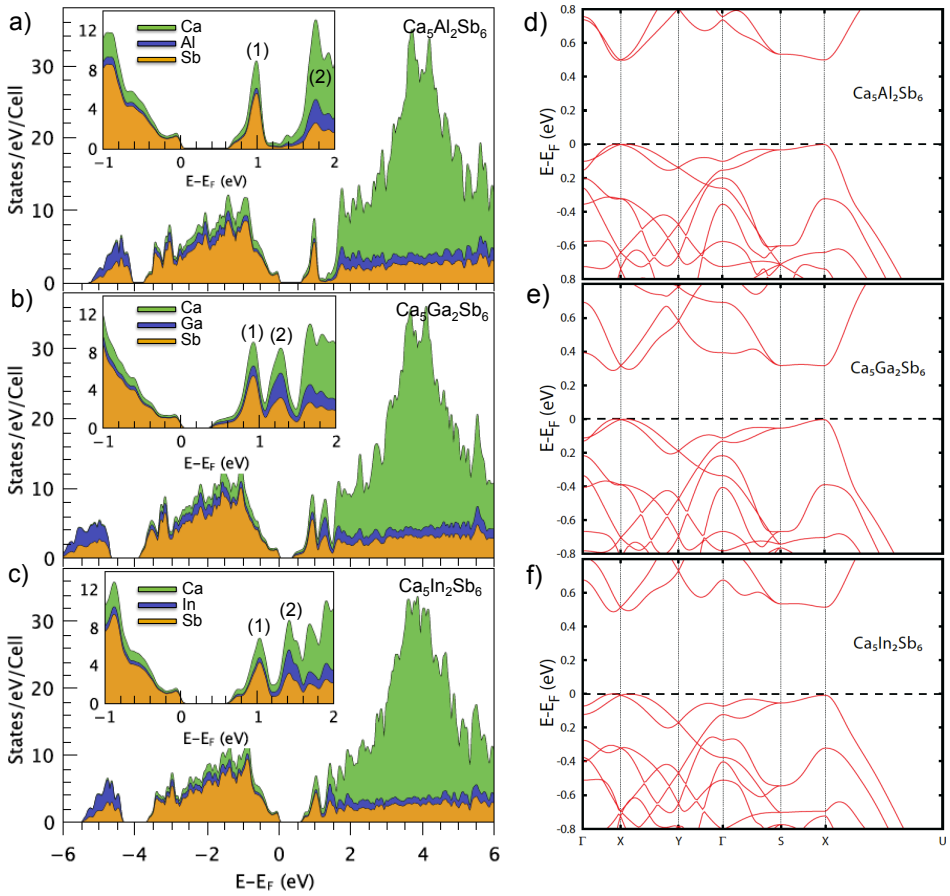

Figure 3.3: (a-c) The conduction band minima of $Ca_5M_2Sb_6$ (M=Al, Ga, In) compounds contain discreet anti-bonding states corresponding to Sb-Sb (1) and M-Sb (2) interactions. The position of the M-Sb anti-bonding peak influences E_g. (d-f) The band structures reveal a high degree of anisotropy. The lightest band mass (m^*_{X-U}) is parallel to the anionic "ladders", while the perpendicular directions (m^*_{X-S} and $m^*_{X-\Gamma}$) are far heavier.

shown in Figure 3.3a-c, are consistent with a predominately covalent depiction of M-Sb bonds. While ionically bonded Ca cations have states primarily in the conduction band and Sb states dominate the valence band, the Al electronic states are relatively equally distributed on either side of the band gap. EDD isosurfaces suggest that the presence of M and Sb electronic states in the valence band arises from a combination of M-Sb (-4 to -6 eV) and Sb-Sb bonding states (0 to -4 eV), as well as from the "lone pairs" surrounding Sb atoms (or equivalently, Ca-Sb interactions). In the conduction band, we intuitively expect to find M-Sb and Sb-Sb anti-bonding states. The peak

in Sb states near the bottom of the conduction band edge, labeled peak (1) in Figure 3.3a-c, likely arises from the Sb-Sb anti-bonding states. This conjecture is supported by a comparison between the DOS of $Ca_5Al_2Sb_6$ and that of the closely related compound, Ca_3AlSb_3, which lacks both Sb-Sb bonds and the corresponding peak near the conduction band minimum [5]. Anti-bonding states arising from Sb-Sb interactions have also been shown to dominate the conduction band minima in a variety of compounds including $Ca_{14}AlSb_{11}$, Zn_4Sb_3, and Mo_3Sb_7 [150]. Higher in the conduction band of each $Ca_5M_2Sb_6$ compound is a distinctive peak with a large fraction of M character (labeled peak (2) in Figure 3.3 (a)-(c)), which likely corresponds to M-Sb anti-bonding states.

The position of peak (2) is strongly dependent on our choice of M. We find that the electronegativity of the M atom, rather than its relative position in the periodic table, is the most accurate indicator of the energy of these electronic states. For example, while Ga falls between Al and In in the periodic table, it has the highest electronegativity of the three elements[151], and thus the lowest energy electronic states (electronegativities are given in Table 3.1).

Table 3.1: Given below for each compound is the electronegativity (χ), band gap from mBJ calculations (E_g theor.), from optical absorption (E_g opt.), and from resistivity (E_g ρ), the band mass, m^*, in three principle directions, and the estimated density of states effective mass, m^*_{DOS}.

	χ	E_g (eV)			effective mass (m_e)			
		theor.	opt.	ρ	m^*_{X-U}	m^*_{X-S}	$m^*_{X-\Gamma}$	m^*_{DOS}
Al	1.61	0.50	0.65	0.71	0.20	6.49	1.36	1.92
Ga	1.81	0.29	0.43	0.56	0.18	3.74	1.19	1.46
In	1.78	0.48	0.64	0.68	0.21	3.76	1.53	1.80

Since M elements posses electronegativities intermediate between Ca and Sb, and have electronic states that span both sides of the band gap in $Ca_5M_2Sb_6$, we might expect the choice of M element to strongly influence the size of the band gap. However, the dominance of Sb states at the conduction band and valence band extrema in $Ca_5M_2Sb_6$ means that, although the position of M-Sb anti-bonding states varies significantly, our choice of M has a diminished influence on the band gap.

The resulting subtle changes to the band structure suggest that partial M atom substitution or alloying can be used as a tool to fine-tune the band gap and band mass without inducing traps that would localize charge carriers.

A common challenge in using Sb-based Zintl compounds for thermoelectric applications is that n-type material cannot be formed. The DOS of $Ca_5Al_2Sb_6$ may shed some light on this limitation: if one were to add electrons to $Ca_5Al_2Sb_6$ (e.g., through chemical doping), the first states to be filled would be Sb-Sb anti-bonding states. Since the related Zintl compound, Ca_3AlSb_3, forms a similar structure, but lacks Sb-Sb "ladder rungs," any destabilizing influence to the Sb-Sb bonding in $Ca_5Al_2Sb_6$ could lead to the formation of Ca_3AlSb_3 with minimal energy cost. Such complications likely affect other ternary Zintl compounds, many of which occupy a phase space crowded with closely related, competing phases.

The electronic dispersions of compounds in the $Ca_5M_2Sb_6$ series are shown along high symmetry directions on the right side of Figure 3.3. In all three compounds, the band gap is nearly direct. Two symmetrically equivalent, overlapping hole pockets (symmetric about the X-Γ axis) characterize the valence band edge of each compound. Fermi levels -0.08 and -0.13 eV correspond to carrier concentration of approximately 1 and 5×10^{20} h^+ cm^{-3}, respectively. Perhaps the most striking feature of the electronic dispersions is the band mass anisotropy in the valence bands; the mass is very heavy in directions perpendicular to the covalent ladders ($m^*_{X-\Gamma}$ and m^*_{X-S} in Table 3.1) and extremely light in the parallel direction (m^*_{X-U} in Table 3.1). Consistent with the assumption that the covalent network in Zintl compounds strongly influences electronic transport, anisotropy is also evident in the published band structures of Ca_3AlSb_3 and AZn_2Sb_2 (A = Ca, Sr, Yb) [5, 75]. In both compounds, the lightest direction is parallel to the covalent substructure: along chains of corner-linked $AlSb_4$ tetrahedra in the case of Ca_3AlSb_3, and along Zn_2Sb_2 slabs in AZn_2Sb_2. This prompts the question of whether the dimensionality of such covalent moieties is an important factor in determining band mass and electronic mobility. Zintl compounds form an extensive variety of distinctive covalent substructures with a range of dimensionalities, making them an ideal starting point for developing such relationships.

In the optimization of thermoelectric materials, the effective mass presents a fundamental conflict; while a heavy "density of states effective mass" (m^*_{DOS}) is desired for a high Seebeck coefficient, a light inertial effective mass (m^*_I) along the direction of transport is necessary for high mobility. The density of states effective mass, and thus the Seebeck coefficient, is dependent on the band mass component in *all* crystallographic directions, as well as the band degeneracy (N_v). This can be approximated as $m^*_{DOS}=(m^*_1 m^*_2 m^*_3)^{1/3}\mathrm{N}_v^{2/3}$, where m^*_1, m^*_2, and m^*_3 are the mass components of a single band along three perpendicular directions. In contrast, the carrier mobility is proportional to the mass of a single band in the direction of interest, which in a single crystal could be chosen to optimize mobility. For example, in the $Ca_5M_2Sb_6$ system, the density of states effective mass is >1 m_e (given in Table 3.1, where $\mathrm{m}^*_{DOS}=(m^*_{X-\Gamma}m^*_{X-Y}m^*_{X-U})^{1/3}2^{2/3}$), while the effective mass parallel to the ladder substructure, m^*_{X-U}, is ∼0.2 m_e. This suggests that in $Ca_5M_2Sb_6$ compounds as well as in other anisotropic Zintl systems, orienting textured or single crystal samples in the light band mass direction (e. g., parallel to the covalent substructure) may yield significant improvements over traditional bulk polycrystalline samples.

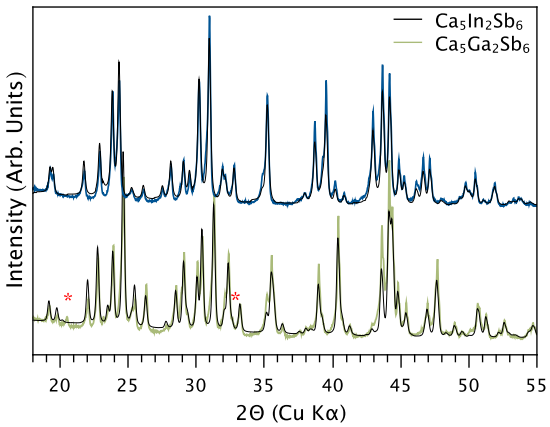

Figure 3.4: XRD patterns of polished, polycrystalline $Ca_5M_2Sb_6$ (M = Ga, In) samples (colored curves) and Rietveld fits using the known crystal structures (black curves) [9]. The reflections belonging to $CaSb_2$ are indicated by red asterisks.

Chemical Characterization $Ca_5Ga_2Sb_6$ and $Ca_5In_2Sb_6$ samples were synthesized for this study, while for $Ca_5Al_2Sb_6$, the undoped sample described in Section 3.3.2 was used. The hot pressed, polycrystalline $Ca_5Ga_2Sb_6$ and $Ca_5In_2Sb_6$ samples were found to be dense (98% and 97% of theoretical, respectively), and more stable in air than the Al-based compound. Scanning electron microscopy of fracture surfaces revealed grains sizes of approximately 1-5 μm. Polished $Ca_5Ga_2Sb_6$ and $Ca_5In_2Sb_6$ samples both contain a small percentage (1-3%) of a secondary phase identified as $CaSb_2$ based on energy dispersive X-ray spectroscopy (EDS) of the coarsest precipitates. Figure 3.4 compares the X-ray diffraction (XRD) patterns of $Ca_5Ga_2Sb_6$ and $Ca_5In_2Sb_6$ samples (colored curves) to the Rietveld fits using their known crystal structures (black curves)[9]. While the $Ca_5In_2Sb_6$ sample appears to be phase pure, two additional reflections corresponding to the $CaSb_2$ phase (marked by red asterisks) are visible in the $Ca_5Ga_2Sb_6$ sample. Preliminary differential scanning calorimetry (DSC) measurements suggest that a phase change may occur in $Ca_5In_2Sb_6$ at around 750 K. However, no strong signals were observed in DSC measurements of the Ga and Al analogues.

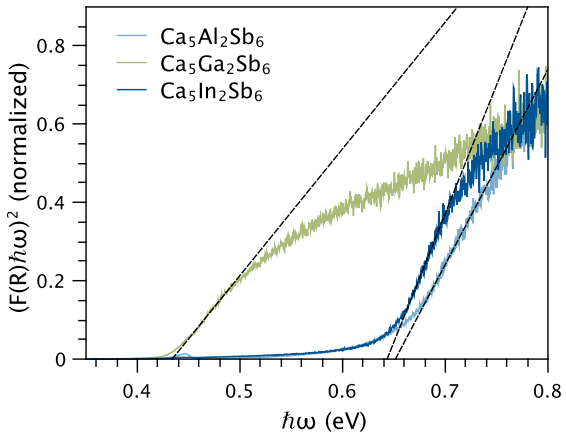

Figure 3.5: Optical absorption measurements at room temperature reveal direct band gaps in the $Ca_5M_2Sb_6$ samples, with the band gap in the Ga analogue (0.43 eV) significantly smaller than the Al or In analogues (0.65 eV and 0.64 eV, respectively).

Optical Properties Optical absorption measurements were used to estimate the room temperature band gaps of the three $Ca_5M_2Sb_6$ compounds. The spectra are shown in Figure 3.5, plotted as normalized $(F(R)\hbar\omega)^2$ vs $\hbar\omega$, where $F(R)$ is the Kubelka-Munk function and $\hbar\omega$ is the photon energy. Each of the spectra exhibits a steep rise in the absorption coefficient with increasing $\hbar\omega$, indicative of a direct band gap. At lower energies, there may also be some evidence of indirect transitions. Given in Table 3.1, the direct optical band gaps obtained from this measurement follow the trend predicted by DFT calculations. The direct band gap observed in $Ca_5Ga_2Sb_6$ is the smallest, while the larger gaps in the Al and In analogues are similar in magnitude.

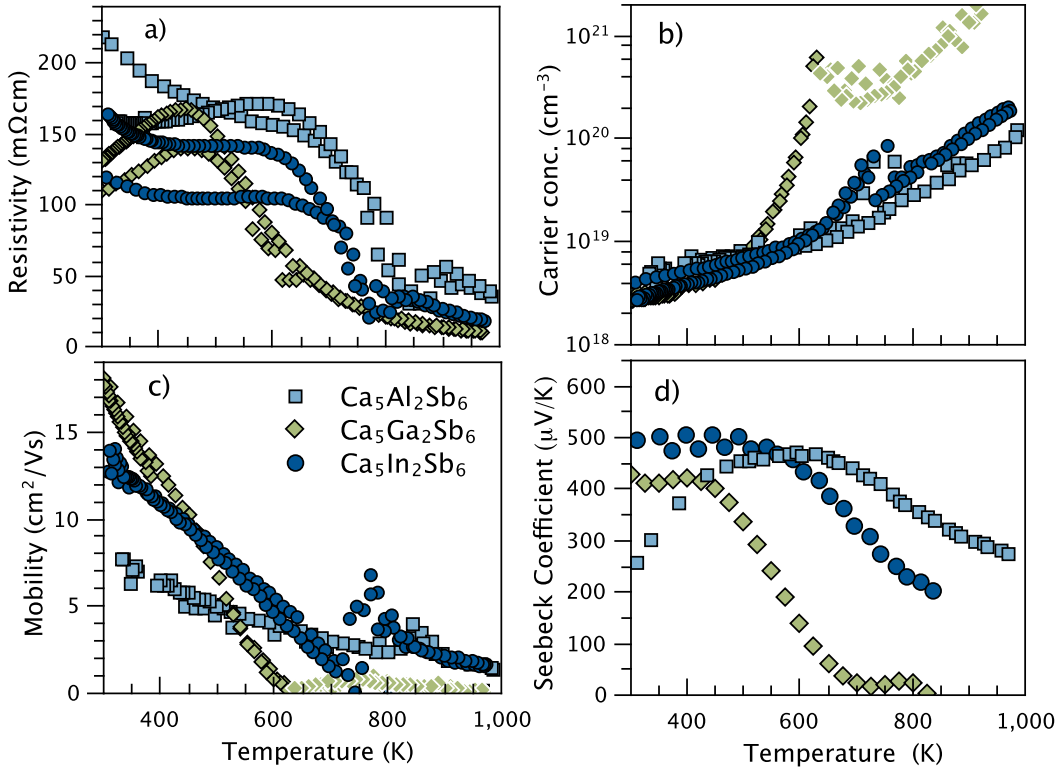

Figure 3.6: The temperature dependence of (a) the resistivity and (b) the Hall carrier concentration of $Ca_5M_2Sb_6$ samples is indicative of intrinsic semiconducting behavior. (c) Hall mobility at 300 K is highest in the Ga-analogue, consistent with its lower band mass. (d) Seebeck coefficients decrease with temperature due to activation of minority carriers. Band gaps estimated from $E_g \propto 2\alpha_{max}T_{max}$ are consistent with results from DFT calculations and with the measured resistivity.

Electronic Transport Properties Semiconducting behavior in $Ca_5M_2Sb_6$ compounds is predicted by both Zintl valence-counting rules and DFT calculations. High temperature resistivity measurements, shown in Figure 3.6a, confirm these predictions. At room temperature, $Ca_5M_2Sb_6$ samples exhibit high resistivity (ρ) that decreases with increasing temperature due to thermally activated intrinsic carriers. The discontinuity in the resistivity of the In- and Al-based compounds near 800 K may be an indicator of a phase transition. Repeated measurements of the same sample show the same behavior, on both heating and cooling, suggesting that any potential phase change is reversible and repeatable. From the slope of the resistivity at high temperature, we can estimate the magnitude of the band gaps using the following relation for intrinsic conduction: $\rho \propto e^{E_g/2k_BT}$. While the magnitude of the band gaps determined from resistivity (given in Figure 3.7) may, in actuality, reflect the band gaps of an unidentified high temperature phase, the trend is similar to that obtained from optical absorption measurements and predicted by DFT calculations (See Table 3.1): the thermal band gap is smallest in the Ga analogue and largest in the Al analogue.

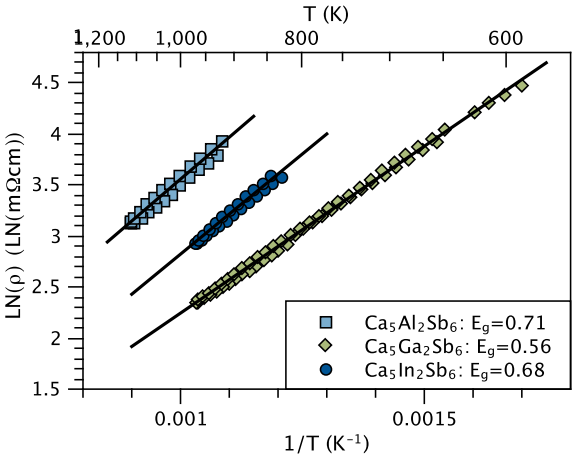

Figure 3.7: The band gap, E_g, is determined from $\rho \propto e^{E_g/2k_BT}$, where ρ is the resistivity in the intrinsic temperature regime.

Shown in Figure 3.6b are the Hall carrier concentrations (n) of $Ca_5M_2Sb_6$ (M = Al, Ga, In) samples. At room temperature, each compound contains a low concentration

of extrinsic, p-type carriers ($n \sim 3{\times}10^{18}$ holes/cm^3), which most likely arise from intrinsic defects in the crystal structure [75]. In contrast to many Zintl systems, in which isoelectronic substitutions influence the extrinsic carrier concentration, M-site substitutions in $Ca_5M_2Sb_6$ do not noticeably influence n at room temperature. This is advantageous, as we are thus able to experimentally observe the effect of M-site substitutions on the system's electronic structure, without having to account for the additional effects of doping.

Above room temperature, thermally activated intrinsic carriers begin to dominate transport, causing n to differ significantly across the $Ca_5M_2Sb_6$ series. In the Ga analogue, intrinsic carrier activation causes the Hall coefficient, R_H, to change sign from from p-type to n-type at 650 K reproducibly (symbols with white borders indicate n-type data). To understand this effect, it is necessary to consider the expression for R_H in mixed conductors:

$$R_H = \frac{n_h\mu_h^2 - n_e\mu_e^2}{e(n_h\mu_h + n_e\mu_e)} \tag{3.1}$$

Here, n_e and n_h are the electron and hole concentrations, and μ_e and μ_h are the electron and hole mobilities, respectively. If $\mu_e > \mu_h$, the Hall coefficient will switch from positive to negative when n_e approaches n_h due to intrinsic carrier activation [152]. n_e need not exceed n_h to switch the sign of R_H, as long as $\mu_e > \mu_h$. DFT calculations support the assumption that $\mu_e > \mu_h$, predicting a lower effective mass in the conduction band of $Ca_5Ga_2Sb_6$ than in the valence band (in the light crystallographic directions). However, without knowing n_e or μ_e directly from experiment, the full expression for R_H cannot be used to calculate the hole concentration and we must instead rely on the single carrier type expression ($R_H = -1/en$), which causes the carrier concentration to diverge when R_H goes to zero (at 650 K in $Ca_5Ga_2Sb_6$).

Figure 3.6c illustrates the temperature dependence of the carrier mobility. In $Ca_5Ga_2Sb_6$ the mobility is underestimated at high temperature due to the divergence of n discussed above ($\mu = 1/ne\rho$). We thus consider only the room temperature mobility when comparing $Ca_5M_2Sb_6$ compounds. At room temperature, despite sim-

ilar carrier concentrations, the Hall mobility varies significantly across the $Ca_5M_2Sb_6$ series, with $Ca_5Ga_2Sb_6$ exhibiting the highest mobility. Carrier mobility is dependent on both inertial effective mass (m_i^*) and carrier relaxation time (τ) according to $\mu = \frac{e\tau}{m_i^*}$. As m_i^* in polycrystalline materials is influenced by the mass of a single band in all crystallographic directions (weighted towards the lightest direction), the trend in mobility in the $Ca_5M_2Sb_6$ system should reflect, to some degree, the predicted trend in m_{DOS}^* (see Table 3.1). Indeed, the Ga analogue has both the highest mobility and the smallest m_{DOS}^*. This can be understood in the context of a Kane band model [76], which takes into account the interaction between the valence and conduction band, leading to an energy and band-gap dependent effective mass. This model predicts a decrease in the effective mass at the band extrema as the band gap narrows, which is qualitatively consistent with DFT calculations (see Table 3.1).

When comparing mobilities, we must also take into account differences in the carrier relaxation time, τ. The negative slope of the mobility as a function of temperature in each $Ca_5M_2Sb_6$ sample suggests that acoustic phonon scattering is the dominant scattering mechanism across the entire measured temperature range. In this limit, the carrier relaxation time can be approximated by Eq. 3.2, where C_l is a function of a combination of elastic constants that depends on the the structure type [153].

$$\tau \propto \frac{C_l}{(m^*)^{3/2}} \tag{3.2}$$

The bulk and shear elastic moduli (K and G respectively) of the $Ca_5M_2Sb_6$ compounds, determined by speed of sound measurements, are given in Table 3.2. The differences in stiffness among these compounds are minor compared with the differences in the band mass predicted by DFT calculations. Though the stiffness is highest in the Al-based compound, this is clearly not sufficiently important to outweigh its heavier effective mass.

The Seebeck coefficients of $Ca_5M_2Sb_6$ compounds, shown in Figure 3.6, are high at room temperature, as expected for intrinsic semiconductors. With increasing tem-

perature, the Seebeck coefficients decrease due to the parasitic voltage contribution of minority carriers. The magnitude and temperature at which the Seebeck coefficient "rolls over" is a function of the band gap ($E_g \propto 2\alpha_{max}T_{max}$)[154]. Consistent with both DFT calculations and resistivity measurements, this relationship yields the smallest band gap in the Ga analogue.

Thermal Transport Properties The total thermal conductivity (κ) in a typical thermoelectric material is the sum of electronic (κ_e), bipolar (κ_B), and lattice (κ_L) contributions. Above the Debye temperature, the lattice thermal conductivity is generally limited by Umklapp scattering, which leads to $\kappa_L \propto 1/T$. However, this 1/T decay can only continue until the minimum lattice thermal conductivity (κ_{min}) is reached, as defined by Cahill in ref[80, 121]. At high temperature ($T > \Theta_D$) κ_{min} can be approximated by Eq. 3.3, where V is the average volume per atom, and ν_L and ν_T are the longitudinal and transverse sound velocities, respectively.

$$\kappa_{min} = \frac{1}{2}\left(\frac{\pi}{6}\right)^{1/3} k_B V^{-2/3}(2\nu_T + \nu_L) \tag{3.3}$$

While compounds with simple crystal structures generally melt before κ_{min} is reached, κ_L in glasses and complex crystals may approach κ_{min} at lower temperatures [8, 7]. Owing to the complexity of its unit cell, κ_L in $Ca_5Al_2Sb_6$ approaches the predicted κ_{min} ($\sim$ 0.5 W/mK) at useful operating temperatures (1000 K) [10]. Since κ_L cannot be reduced beyond κ_{min}, improvements to the $Ca_5M_2Sb_6$ system at high temperature can only be achieved by reducing κ_{min} itself. From Eq. 3, we can see that this is best accomplished by reducing the system's speed of sound.

Table 3.2: Here, d is the theoretical density, D is thermal diffusivity at 325 K, and κ_{min} is the minimum lattice thermal conductivity at high temperature ($T > \Theta_D$).

	d	G	K	ν_T	ν_L	D	κ_{min}
	g/cm^3	GPa	GPa	m/s	m/s	mm^2/s	W/mK
Al	4.31	25	40	2400	4100	0.98	0.53
Ga	4.52	24	40	2280	3970	0.94	0.50
In	4.90	22	38	2115	3710	0.82	0.46

The longitudinal and transverse sound velocities in a solid are related to the

material's stiffness and density according to equations 3.4 and 3.5, where d is the theoretical density and K and G are the bulk and shear moduli, respectively.

$$\nu_T = \sqrt{\frac{G}{d}} \tag{3.4}$$

$$\nu_L = \sqrt{\frac{K + \frac{4}{3}G}{d}} \tag{3.5}$$

As expected, replacing Ga or In for Al in the $Ca_5M_2Sb_6$ system leads to increased density, and thus to the decreased sound velocities given in Table 3.2. Solving equations 3.4 and 3.5 for the elastic constants K and G reveals that lattice stiffness also decreases as we move towards the heavier elements. This effect is a natural result of progressing towards the heavier triel elements; larger atoms possess orbitals that are more diffuse, leading to a lesser degree of overlap with neighboring atoms [155]. This results in lower bond strength and a softer crystal structure. In $Ca_5In_2Sb_6$, this beneficial combination of increased density and decreased stiffness leads to a 10% decrease in the speed of sound relative to $Ca_5Al_2Sb_6$, and a corresponding decrease in the predicted κ_{min}, given in Table 3.2.

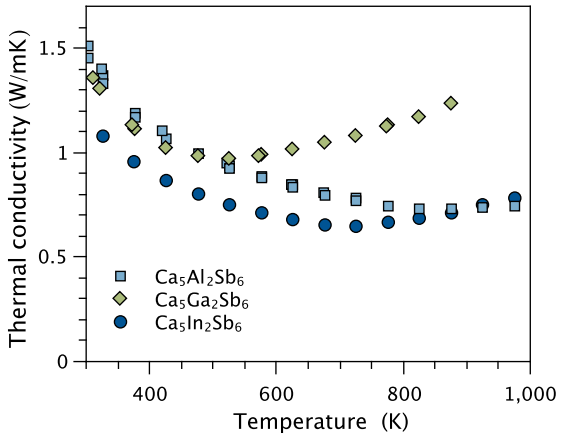

Figure 3.8: The thermal conductivity in $Ca_5M_2Sb_6$ (M = Al, Ga, In) is dominated by the lattice term at room temperature and by the bipolar term at higher temperatures. $Ca_5In_2Sb_6$ exhibits the lowest κ_L due to its relatively dense, soft lattice.

The thermal conductivity of each compound, shown in Figure 3.8, is calculated

from thermal diffusivity (D) using κ=$C_p dD$. The measured values of D at 325 K are given in Table 3.2, while C_p is estimated from the Dulong Petit heat capacity and d is the measured geometric density. The electronic contribution to κ can be estimated from κ_e=LT/ρ, using the non-degenerate limit of the Lorenz number (L=1.5). This contribution is negligible at room temperature and is minor even at high temperature ($<$ 0.1 W/mK at 1000 K) due to the high resistivity of the samples. In contrast, the bipolar contribution is very significant at intermediate temperatures and above ($>$ 500 K), giving rise to the increasing κ with respect to temperature. $Ca_5Ga_2Sb_6$ exhibits the most pronounced bipolar contribution due to its smaller band gap. A direct comparison of the lattice thermal conductivity of $Ca_5M_2Sb_6$ (M = Al, Ga, In) samples can best be made at room temperature, at which point both the electronic and bipolar contributions are small. Here, the thermal conductivity follows the trend that we expect based on the sound velocities given in Table 3.2; κ_L is highest in the Al-based compound and lowest in the heavier, softer In analogue.

Conclusions In an attempt to clarify the role of the metal (M) site in the thermal and electronic properties of ternary A-M-X Zintl compounds, we have investigated trends in the chemical and transport properties of the $Ca_5M_2Sb_6$ (M = Al, Ga, In) system. While the Zintl-Klemm concept allows the M atoms to behave as either ionic charge donors *or* covalently bonded anions, Density Functional calculations support the latter by revealing charge accumulation between M and Sb sites, and distinct M-Sb bonding and anti-bonding states in the DOS. We have found that the electronegativity of the M element is a good indicator for the position of the M-Sb anti-bonding states in the conduction band. These states indirectly influence the position of the conduction band minima in the $Ca_5M_2Sb_6$ system, leading to smaller band gaps in the Ga- and In-based compounds. This is reflected in high temperature electronic and thermal measurements, which confirm the smaller band gaps and reveal higher mobility in $Ca_5Ga_2Sb_6$ and $Ca_5In_2Sb_6$ relative to the Al analogue. This trend in band gap magnitude is also confirmed by room temperature optical absorption measurements. Similar room temperature hole concentrations across the

$Ca_5M_2Sb_6$ series ensure that these experimentally observed trends stem from band structure changes, rather than from doping effects. Progressing towards heavier elements in the $Ca_5M_2Sb_6$ system also results in a denser, softer crystal structure, which leads to reduced sound velocities, and a corresponding reduction in lattice thermal conductivity.

Ultimately, while the effects of substitutions on the M site in $Ca_5M_2Sb_6$ are subtle, they can be readily rationalized using fundamental chemical principles, providing us with a sensitive and intuitive route for fine-tuning the transport properties of the $Ca_5M_2Sb_6$ system.

3.3 Optimization of $Ca_5Al_2Sb_6$

3.3.1 Na-doped $Ca_5Al_2Sb_6$

Reproduced with permission from *Adv. Func. Mater.* **20**, 4375-4380 (2010).

Introduction $Ca_5Al_2Sb_6$ is an appealing thermoelectric material due to its low lattice thermal conductivity, reasonably large band gap, stability at high temperature, and relatively inexpensive elemental constituents. However, like other $Ca_5M_2Sb_6$ compounds (M = Al, Ga, In), $Ca_5Al_2Sb_6$ behaves as a charge-balanced semiconductor with intrinsic electronic properties. Since good thermoelectric performance is realized in heavily doped semiconductors, increasing and controlling the carrier concentration in this compound is crucial. Na is one potential p-type dopant in $Ca_5Al_2Sb_6$. Each substitution of Na^{1+} on the Ca^{2+} is expected to lead to one free hole, increasing the p-type carrier concentration and leading to an improved figure of merit. This work focuses on the high temperature thermal and electronic properties of $Ca_{5-x}Na_xAl_2Sb_6$, where $x = 0$, 0.05, 0.25, and 0.50.

Chemical Characterization Hot pressing of intrinsic $Ca_5Al_2Sb_6$ and Na-doped samples yielded high density polycrystalline ingots ($\geq$98% theoretical). Sample cross

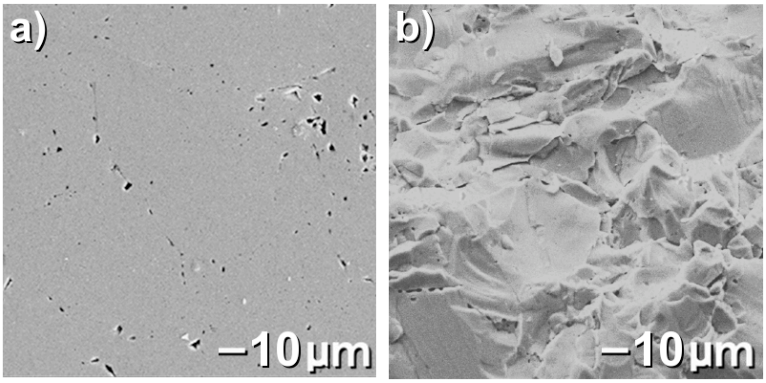

Figure 3.9: Scanning electron micrographs of (a) a polished surface and (b) a fracture surface of $Ca_{4.75}Na_{0.25}Al_2Sb_6$ following hot pressing.

sections were investigated with scanning electron microscopy (SEM), which confirmed the high density of these samples, with few pores observed (Figure 3.9). Despite the moderate pressure and temperature used during hot pressing, average grains sizes were found to be in excess of 10 μm by SEM. No secondary phases were observed by energy dispersive spectroscopy (EDS) or backscattering mode SEM imaging. EDS analysis found Na in all alloyed samples, however, a plateau in Na content was observed above $x = 0.25$ (Figure 3.11a). The dashed line in Figure 3.11a shows the expected sodium content from the nominal synthetic stoichiometry. For compositions above $x = 0.25$, an unidentified secondary phase was extruded out of the die during pressing. This suggests the material expelled during pressing was sodium rich, consistent with the variety of low melting phases in the Na-Sb and Na-Al phase diagram.

X-ray diffraction (XRD) patterns of polycrystalline slices of $Ca_{5-x}Na_xAl_2Sb_6$ were subject to Rietveld refinement using the known structure. Figure 3.10 shows two representative patterns: $x = 0$ and 0.5.[13] Additionally, Figure 3.10 shows the fit and difference profile for the $x = 0$ phase. No secondary phases were observed in any of the XRD patterns. Na was selected as a dopant for Ca due to the similar ionic radii; it is thus not a surprise that no trend in unit cell parameters was observed with Na doping.

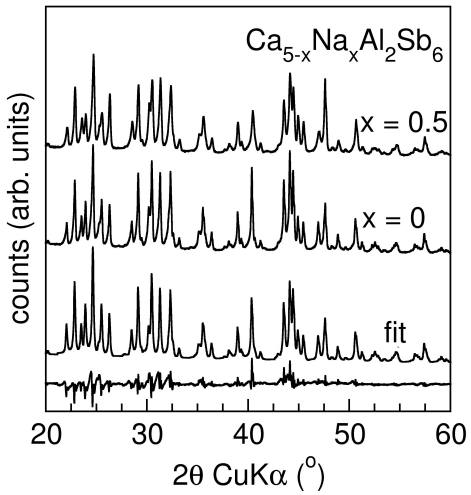

Figure 3.10: Powder XRD patterns for $Ca_{5-x}Na_xAl_2Sb_6$ (x = 0, 0.5), Rietveld fit to the $Ca_5Al_2Sb_6$ structure and difference profile for the $x = 0$ pattern.

Electronic properties In undoped $Ca_5Al_2Sb_6$, we find decreasing resistivity with increasing temperature (Fig 3.12a), suggesting carrier activation across a band gap. Fitting the high temperature behavior of the undoped sample ($\rho \propto e^{E_g/2k_BT}$ for an intrinsic semiconductor), a band gap of 0.5 eV is obtained, similar to that obtained from $Yb_{14}AlSb_{11}$ (0.5 eV).[21]

With low sodium doping (x=0.05), a decreasing resistivity with increasing temperature is likewise observed. The Hall carrier concentration ($n_H = 1/R_He$, with Hall coefficient R_H) is shown in Figure 3.12c. A slight rise in carrier concentration with temperature is observed in doped samples, likely due to intrinsic carrier activation. The temperature dependence of the resistivity for x=0.05 arises from this slight carrier activation and the thermally activated carrier mobility. The activated mobility, apparent from the positive slope in the mobility at low temperature (Figure 3.12d) may arise from the presence of a resistive grain boundary phase such as an oxide.

At high doping levels ($x \geq$0.25), the electrical resistivity is linear at high temperature (Fig 3.12b) and the Hall carrier concentration is approximately temperature independent (Figure 3.12c). The mobility in heavily doped samples decays with increasing temperature, associated with phonon scattering. At low temperatures, the mobility still shows a slightly positive slope and the resistivity briefly exhibits a neg-

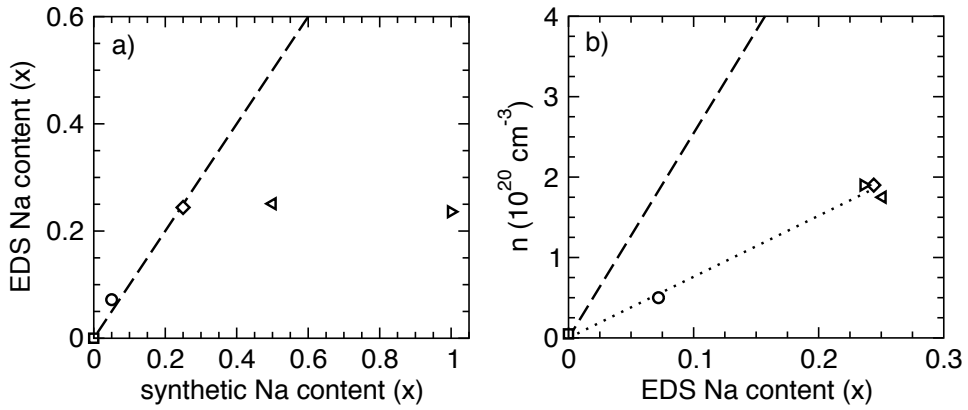

Figure 3.11: (a) Na levels in $Ca_{5-x}Na_xAl_2Sb_6$ track the synthetic composition well (dashed line) up to a maximum of x=0.25. (b) Hall effect measurements show that n increases with Na content at less than the predicted rate (dashed line), and does not exceed 2×10^{20} h^+ cm^{-3}.

ative slope with temperature. These observations suggest the activation effect in sample $x = 0.05$ is again present, albeit at a lower level, in the samples here.

Extrinsic doping of $Ca_5Al_2Sb_6$ with sodium clearly yields a material with the properties of a heavily doped semiconductor. Figure 3.11b shows the relationship between doping level and Hall carrier concentration (n) with increased alloying. The dashed line represents the theoretical n vs EDS x, calculated using Zintl-Klemm charge counting rules. The carrier concentration for samples above $x = 0.25$ plateaued at 2×10^{20} cm^{-3}. The measured carrier concentration is lower than expected from the EDS composition. This difference may be due to compensating impurities which reduce the doping effectivity. Alternatively, extended defects may form which involve additional anionic bonding, thereby reducing the effective hole concentration.

The Seebeck coefficient of the nominally undoped sample is positive and reasonably large in magnitude, typical for nominally undoped Zintl antimonides.[21] The effect of Na-doping, and thus increasing carrier concentration, on the Seebeck coefficient is shown at 300 K in Figure 3.13. As generally expected, increased carriers lead to a decrease in Seebeck coefficient. Further analysis incorporates solutions to the Boltzmann transport equation within the relaxation time approximation. In the

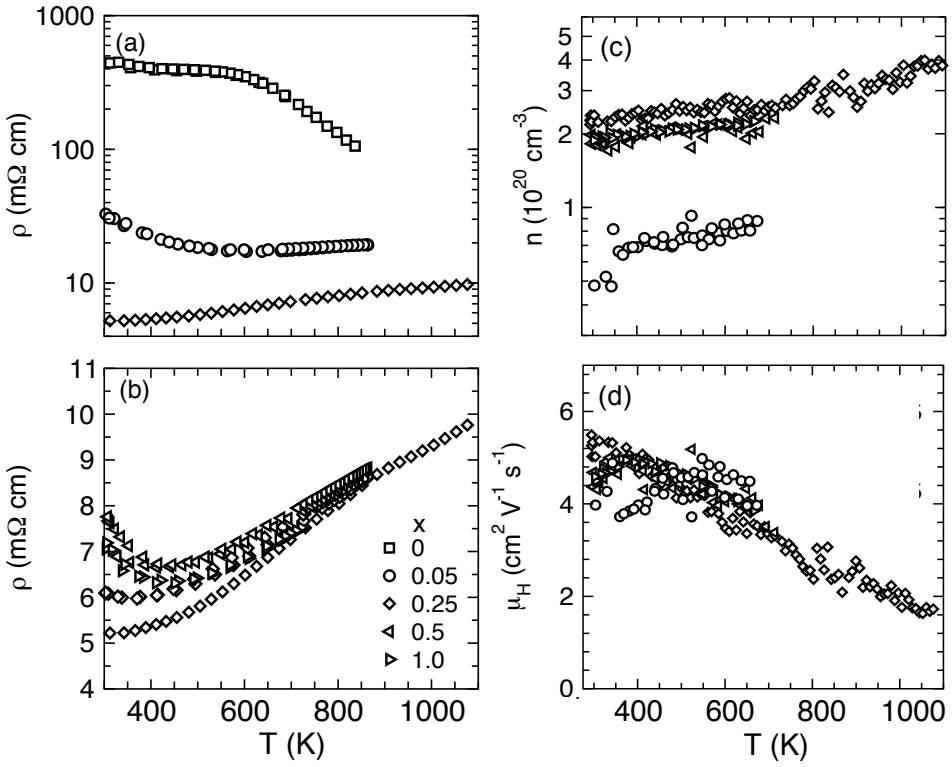

Figure 3.12: (a-b) The resistivity of $Ca_{5-x}Na_xAl_2Sb_6$ decreases with increasing x. (c) The Hall carrier concentration is relatively constant with temperature for all compositions. (d) Samples with low doping levels show some evidence for activated behavior leading to a positive slope in the mobility near room temperature. The decay in mobility at higher temperatures is associated with phonon scattering.

absence of minority carrier properties, a single parabolic band (SPB) model is utilized. Described in Chapter 2.3, this model relates the Seebeck coefficient to the carrier concentration via the chemical potential (η) assuming $\lambda = 0$ (acoustic phonon scattering). The dashed curve was generated at room temperature with an effective mass of $m^* = 2.2\ m_e$. Good agreement is found with the measured room temperature Seebeck coefficients, suggesting that a single parabolic band reasonably describes the valence band edge.

The high temperature Seebeck coefficients as functions of temperature are shown in Figure 3.14. The nominally undoped sample shows a decaying Seebeck coefficient with increasing temperature, as carrier activation dominates transport. Linearly temperature dependent Seebeck coefficients are obtained with extrinsic doping, as ex-

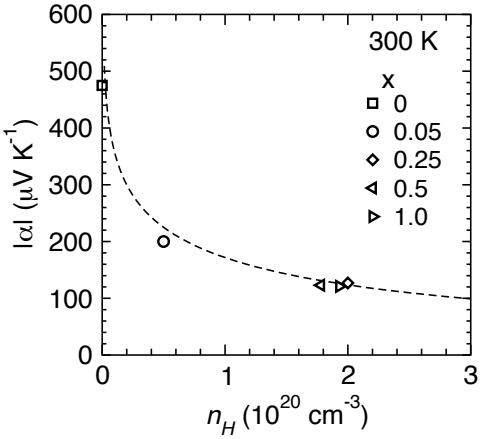

Figure 3.13: Carrier concentration (n) dependence of room temperature Seebeck coefficients compared to a single parabolic band model with an effective mass of 2.2 m_e.

pected for degenerate semiconductors. At high temperature, the Seebeck coefficient reaches a broad maximum due to minority carrier activation. From the maximum temperature and associated Seebeck coefficent, a thermal band gap of $\sim$0.4 eV is calculated ($E_g \simeq 2eT_{max}\alpha_{max}$).[154]

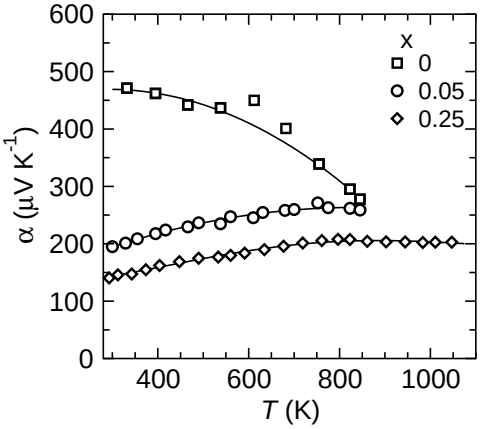

Figure 3.14: High temperature Seebeck coefficients of $Ca_{5-x}Na_xAl_2Sb_6$ show decreasing magnitude with increasing Na doping.

Thermal properties The thermal conductivity, calculated from $\kappa = DC_pd$, where D is thermal diffusivity, C_p is the Dulong-Petit heat capacity (C_p=0.33 J g^{-1} K^{-1}), and d is density, is shown in Figure 3.15a. The electronic thermal conductivity, κ_e, is

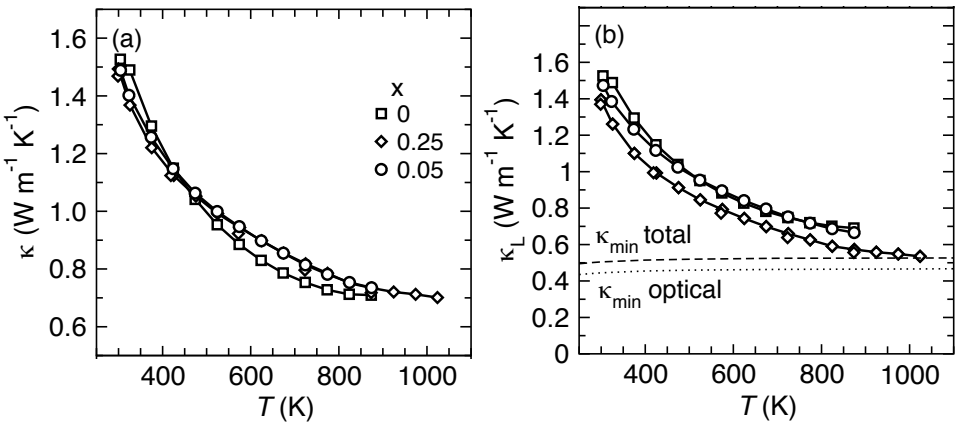

Figure 3.15: (a) The total thermal conductivity and (b) the lattice component for $Ca_{5-x}Na_xAl_2Sb_6$. The minimum thermal conductivity is obtained from Eq. 3.8. By assessing the optical mode contribution to the minimum thermal conductivity (κ_{min} optical), the experimental acoustic contribution can be estimated.

estimated here using the Wiedemann-Franz relationship ($\kappa_e = LT/\rho$). The temperature dependent Lorenz numbers were calculated using a single parabolic band model, where the reduced Fermi energy is a function of the experimental Seebeck coefficient. Due to relatively low doping levels, κ_e is minimal and the thermal conductivity ($\kappa = \kappa_L + \kappa_e + \kappa_B$) is dominated by the lattice (κ_L) and bipolar contributions (κ_B). Minimal bipolar effects are observed within the temperature range investigated.

Ultrasonic measurements at 300 K yield longitudinal and transverse speeds of sounds of $\nu_l = 4093$ m/s and $\nu_t = 2399$ m/s. Eq. 3.6 yields a mean speed of sound of 2660 m/s (ν_m, Eq. 3.6). These values are ∼14% higher than the Zintl antimonide $SrZn_2Sb_2$. Such a difference can be rationalized from the difference in density (d) if the bulk moduli (B) of $SrZn_2Sb_2$ and $Ca_5Al_2Sb_6$ are identical. From the speed of sound values, an effective Debye temperature of 257 K is obtained from Eq. 3.7.

$$\nu_m^3 = \frac{3}{\nu_l^{-3} + 2\nu_t^{-3}} \tag{3.6}$$

$$\theta_D = \frac{\nu_m \hbar}{k_B} \left(\frac{6\pi^2}{V} \right)^{1/3} \tag{3.7}$$

At high temperatures, Fig. 3.15b shows that κ_L approaches the minimum thermal

conductivity (κ_{min}, dashed line) calculated from Eq. 3.8 [121]. Such a low thermal conductivity likely arises from the structural complexity of $Ca_5Al_2Sb_6$. The vast majority of the heat capacity is in high frequency optical modes with near zero group velocity. The contribution of these modes to the thermal conductivity can be estimated using the expression for minimum thermal conductivity (Eq. 3.8). To isolate the optical contribution to κ_{min}, the high-frequency edge of the acoustic branch ($\frac{\theta_i}{TN^{1/3}}$, N = 26 atoms/primitive cell) sets the lower bound to the integral. This optical κ_{min} is shown as the dotted line in Fig. 3.15b.

$$\kappa_{min} = \left(\frac{\pi}{6}\right)^{1/3} \frac{k_B}{V^{2/3}} \sum_i \nu_i \left(\frac{T}{\theta_i}\right)^2 \int_0^{\frac{\theta_i}{T}} \frac{x^3 e^x}{(e^x - 1)^2} dx \tag{3.8}$$

With this approximation for the optical contribution, the acoustic contribution is $\kappa_L - \kappa_{min,optical}$. The decay in $\kappa_{acoustic}$ with increasing temperature arises from increased Umklapp scattering. At high temperatures, Umklapp scattering leads to a near-minimum acoustic phonon mean free path.

The low thermal conductivity in $Ca_5Al_2Sb_6$ thus appears to arise from the low group velocity of the optical modes and Umklapp scattering of the acoustic modes. Further reduction in κ_L could come from nanostructures or alloying to further suppress the acoustic mean free path at low temperatures, or from the investigation of $A_5M_2Pn_6$ compounds with higher mass densities.

Thermoelectric figure of merit From the high temperature transport measurements discussed above, the thermoelectric figure of merit (zT) can be estimated. Figure 3.16a shows zT curves calculated for the x=0-0.25 compositions. A maximum zT value in excess of 0.6 is obtained at 1000 K.

From the transport data, a single parabolic band model can be developed to determine the optimum carrier concentration. Here, we have focused on transport at 700 K, to avoid any error associated with thermally-induced minority carriers. The measured properties of the x=0.25 sample were used as inputs to yield an effective mass of 1.9 m_e and intrinsic mobility of μ_o = 4.7 cm^2 V^{-1} s^{-1}). A constant value of the

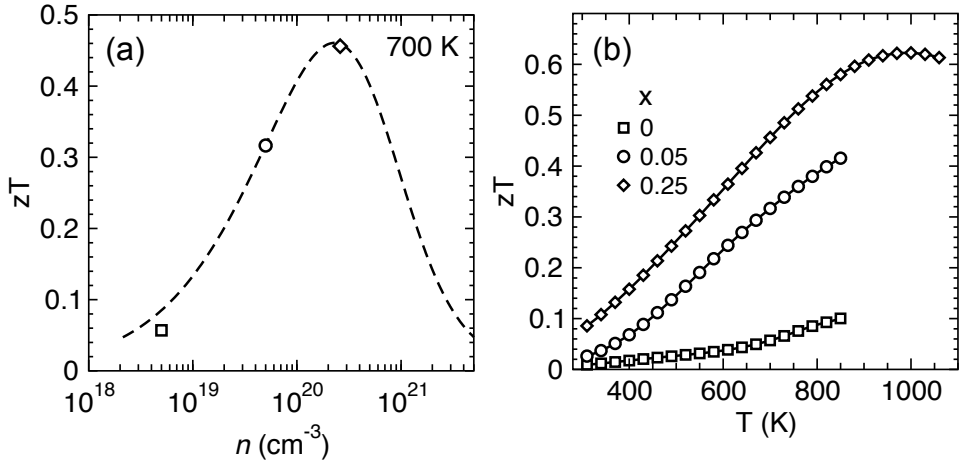

Figure 3.16: (a)The high temperature thermoelectric figure of merit (zT) of $Ca_{5-x}Na_xAl_2Sb_6$ samples increases with increasing temperature. Experimental zT versus carrier concentration at 700K. (b) The optimization of zT with carrier concentration was confirmed using a single parabolic band model with parameters given in the text.

lattice thermal conductivity were used (0.76 W m^{-1} K^{-1}), regardless of doping level. The result of this model is shown in Figure 3.16b, and yields good agreement with experiment across the measured carrier concentration range. Note that this model is limited by the assumption of a single parabolic band. Considering the effects of minority carriers, this is likely a slight underestimation of the optimum carrier concentration. Above 1000 K, samples with greater doping should yield higher zT than the $x = 0.25$ sample by remaining degenerate to higher temperatures. Beyond good thermoelectric performance, $Ca_5Al_2Sb_6$ is intriguing for magnetic investigations as the Al site should be suitable for transition metal substitution (as we have previously seen in $Yb_{14}AlSb_{11}$).[21, 156].

Conclusions Inspired by the excellent thermoelectric performance of $Yb_{14}MnSb_{11}$, this investigation of the high temperature transport properties of $Ca_5Al_2Sb_6$ reveals good thermoelectric performance and generally highlights the potential for Zintl compounds as thermoelectrics. The transport behavior of $Ca_5Al_2Sb_6$ is quite similar to $Yb_{14}MnSb_{11}$, with a large effective mass, low mobility, and low lattice thermal conductivity arising from structural complexity. The carrier concentration varies monotoni-

cally as a function of chemical dopant concentration and can reach levels associated with optimum performance (10^{20} h^+cm^{-3}). The large band gap ($\sim$0.5 eV) and low-cost, light, nontoxic materials suggest that $Ca_5Al_2Sb_6$-based materials could be ideal for high temperature waste heat recovery.

3.3.2 Zn-doped $Ca_5Al_2Sb_6$

Introduction Although Na-doping in $Ca_5Al_2Sb_6$ successfully yielded degenerate behavior, a solubility limit was reached at a doping level of 2×10^{20} h^+cm^{-3} and the dopant effectiveness was low [10]. Inspired by our previous investigation of the thermoelectric properties of Zn-doped $Yb_{14}MnSb_{11}$, here we consider $Ca_5Al_{2-x}Zn_xSb_6$ (x = 0, 0.02, 0.05, 0.10, and 0.20) [43]. Zn is an attractive dopant due to its low cost and ease of handling. A combination of high temperature transport measurements and classic transport theory is used to compare the effects of Na- and Zn-doping in $Ca_5Al_2Sb_6$.

Chemical Characterization Following ball milling and hot pressing, $Ca_5Al_{2-x}Zn_x$-Sb_6 samples (x = 0, 0.02, 0.05, 0.10, 0.20) have geometric densities ranging from 91% to 97%, and are found be phase pure by X-ray diffraction (Figure 3.17) and scanning electron microscopy (SEM). SEM analysis of fracture surfaces reveals small grains (1 μm diameter) and porosity (0.1 μm diameter) at grain boundaries. The larger grain size (50 μm) and slightly higher density ($\geq$98%) in the Na-doped samples are due to the use of a higher hot-pressing temperature (973 K) and pressure (100 MPa) compared with the current study.

Electronic Transport Properties Upon doping, each Zn^{2+} atom on an Al^{3+} site is expected to contribute one free hole. As shown in Figure 3.18, the measured room temperature Hall carrier concentration (n_H) in $Ca_5Al_{2-x}Zn_xSb_6$ is very close to that

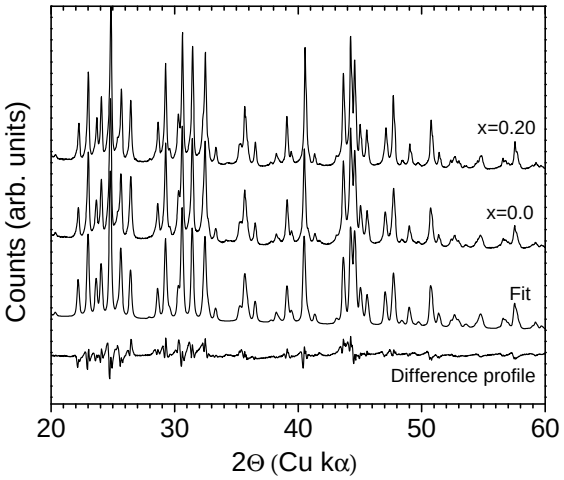

Figure 3.17: $Ca_5Al_{2-x}Zn_xSb_6$ X-ray diffraction patterns ($x = 0, 0.20$), Rietveld fit to the $x = 0$ sample and associated difference profile. No secondary phases are observed for the x range investigated ($0 < x < 0.20$).

predicted (dashed line) as a function of Zn content (x). This is in sharp contrast to the measured hole concentrations in $Ca_{5-x}Na_xAl_2Sb_6$, which are significantly lower than predicted. The maximum hole concentration obtained in Zn-doped $Ca_5Al_2Sb_6$ is twice that obtained by doping with Na.

Figure 3.19 shows high temperature Hall measurements for $Ca_5Al_{2-x}Zn_xSb_6$ samples as well as $Ca_{4.75}Na_{0.25}Al_2Sb_6$ from Section 3.3.1. The Hall carrier concentration (Figure 3.19(a)) of the undoped sample increases with increasing temperature due to minority carrier activation beginning at 400 K. The anomaly in the resistivity at 850 K requires further investigation, but may be due to a phase change. In the doped samples, the carrier concentration remains nearly constant with increased temperature, indicative of degenerate carrier behavior.

The Hall mobility (Figure 3.19(b)) as a function of temperature is calculated from the measured Hall coefficient and resistivity (ρ). When scattering by acoustic phonons dominates, the temperature dependence of μ is described by $\mu_a \propto T^{-\nu_a}$, where ν_a is predicted to vary from 1 to 1.5 for degenerate and nondegenerate semiconductors, respectively [76]. In the case of undoped $Ca_5Al_2Sb_6$, the mobility can be fit using ν_a=1.5, as shown in Figure 3.19(b). Compared with undoped and Na-doped

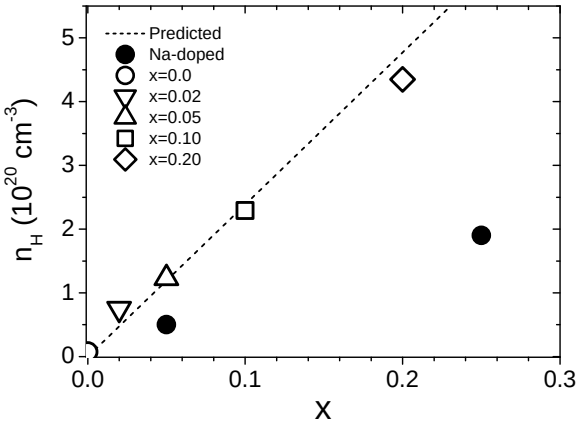

Figure 3.18: With zinc doping, the carrier concentration at 300 K is directly proportional to the level predicted using simple electron counting (dashed line). This is in contrast to the lower doping efficiency with sodium [10].

$Ca_5Al_2Sb_6$, the mobility in Zn-doped samples is suppressed at low temperatures (300-600 K) and rises slightly with increasing temperature.

Dramatic changes to either carrier scattering or the band mass could lead to the decreased mobility in the Zn-doped $Ca_5Al_2Sb_6$ samples. Sources of scattering could include (a) boundary scattering from pores or grain boundaries, (b) activation barriers at grain boundaries ($\mu_{act} \propto e^{E_A/k_BT}$), (c) local strain fields [155], or (d) ionized impurity scattering ($\mu_i \propto T^{\nu_i}$). The temperature dependence of the mobility can be fit with a combination of acoustic phonon scattering and an activation barrier, which is consistent with the small grain size observed in the Zn-doped samples. However, further study of microstructure and transport properties are needed to understand the exact role of scattering in the decreased mobility.

To evaluate the effect of Zn on the band structure, the Seebeck coefficients of Zn- and Na-doped $Ca_5Al_2Sb_6$ are considered at 700 K (Figure 3.20). At this temperature, Zn- and Na-doped samples with equivalent carrier concentrations and scattering mechanism (acoustic phonon scattering) exhibit nearly identical Seebeck coefficients. This suggests that the effective mass is unaffected by Zn doping at high temperature. The pisarenko curve in Figure 3.20 was generated using a single parabolic band (SPB) model with an effective mass of 1.8 m_e, and assuming acoustic phonon scat-

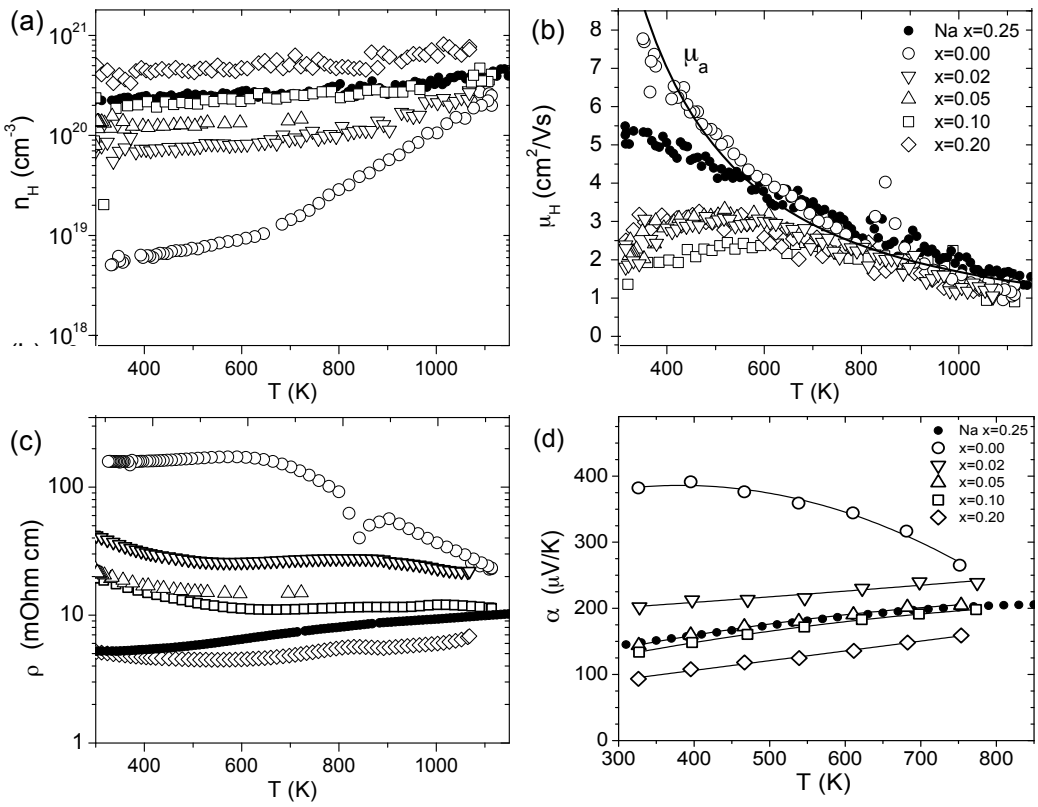

Figure 3.19: (a) The Hall carrier concentration of $Ca_5Al_{2-x}Zn_xSb_6$ samples increases with x. Doped samples exhibit extrinsic behavior to 800 K. (b) Undoped $Ca_5Al_2Sb_6$ exhibits a mobility dominated by phonon scattering across the entire temperature range investigated, while Zn-doped samples show evidence of additional scattering mechanisms at low temperature. (c) High temperature resistivity and (d) Seebeck coefficients decrease with increasing Zn doping level, and show degenerate behavior for the extrinsically doped compositions, similar to the Na-doped analog [10].

tering. It appears that for high carrier concentrations (x=0.2 sample with n_H=4.7 $\times$ 10^{20} h^+cm^{-3}), $Ca_5Al_2Sb_6$ can no longer be described by a single parabolic band model. Shown in Figure 3.3, the pocket of bands at ~ -0.1 eV and the anharmonicity away from the intrinsic band edge may lead to this breakdown of the SPB model at high carrier concentrations. We have not employed this model at low temperatures, as it is difficult to unravel potential changes in the effective mass from the multiple scattering mechanisms.

The Seebeck coefficients are shown in Figure 3.19(d) as a function of temperature. Doped samples exhibit increasing Seebeck coefficients with rising temperature, as

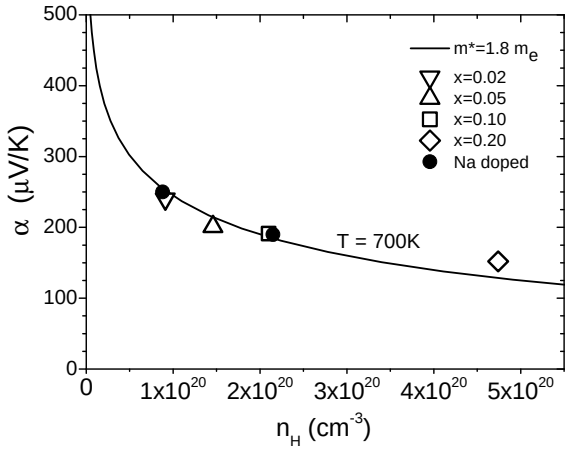

Figure 3.20: Similar Seebeck coefficient values for Na- and Zn-doped $Ca_5Al_2Sb_6$ at equivalent carrier concentrations suggest similar band mass. Curve generated using a single parabolic band approximation and an effective mass of 1.8 m_e [10].

expected for extrinsically doped semiconductors. The Seebeck coefficients of the Na-doped (x=0.25) and Zn-doped (x=0.10) samples are nearly identical across the entire temperature range, consistent with their similar carrier concentrations.

Thermal Transport Properties The thermal conductivity, shown in Figure 3.21, was calculated using $\kappa = DdC_p$, where the thermal diffusivity (D) is measured using the laser flash method, d is the geometric density, and the heat capacity (C_p) is given by the Dulong-Petit value. The total thermal conductivity is a combination of electronic (κ_e), lattice (κ_L), and bipolar contributions (κ_B). As increasing carrier concentration leads to increased κ_e, the largest values of κ are found in the most heavily doped samples. The Wiedemann-Franz relation can be used to estimate $\kappa_e = \frac{LT}{\rho}$. Here, the Lorenz numbers (L) are calculated from experimental Seebeck coefficients, using the single parabolic band approximation described in Section 2.3, and assuming a mobility limited by acoustic phonon scattering. Near room temperature, the presence of other scattering sources may alter L, but are not accounted for in this model. As the Seebeck coefficient was only measured to 773 K, the value of L at 773 K is used to calculate κ_e at higher temperatures.

Subtracting κ_e from the total thermal conductivity yields κ_L+κ_B (Fig. 3.21(b)).

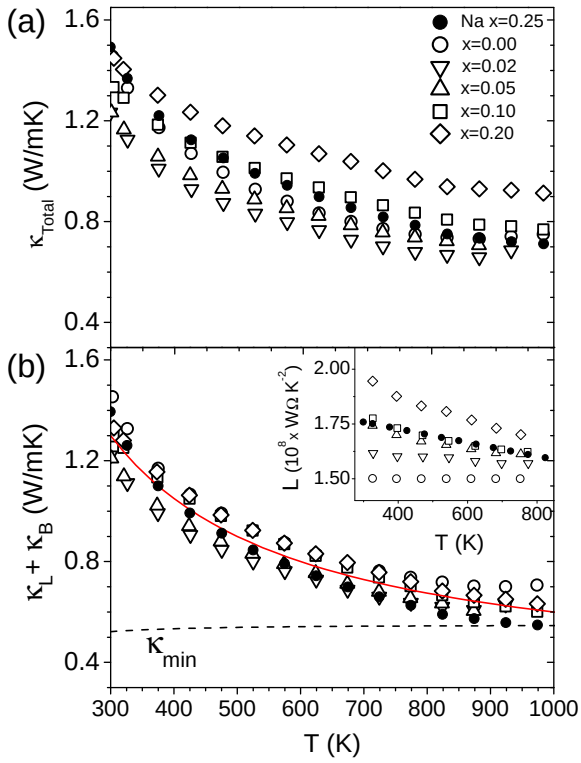

Figure 3.21: (a) Total thermal conductivity of $Ca_5Al_{2-x}Zn_xSb_6$ increases with increasing doping level and thus electronic conductivity. (b) The lattice contribution (κ_L) decays with T^{-1} and approaches a minimum value at high temperature, consistent with prior Na-doped compositions [10]. To calculate κ_L, Lorenz coefficients (inset) were calculated using the single parabolic band approximation.

While undoped $Ca_5Al_2Sb_6$ shows a slight bipolar contribution at high temperature, no such effect is seen in the the heavily doped samples [157]. These are well-described by the T^{-1} relationship expected for Umklapp scattering dominated transport, as shown by the red curve in 3.21(b). As in Na-doped $Ca_5Al_2Sb_6$, the effect of Zn doping on the lattice thermal conductivity is negligible.

An estimated minimum thermal conductivity, κ_{min}, (dashed line) was calculated using Cahill's formulation for the thermal conductivity of glasses, and the previously reported longitudinal and transverse speeds of sound of $Ca_5Al_2Sb_6$ (4170 m/s and 2440 m/s respectively) [10, 80]. For doped samples, the approach of κ_L towards the predicted glassy minimum κ_L is largely due to the structural complexity and high mass contrast of $Ca_5Al_2Sb_6$ (26 atoms per primitive cell), which traps heat in low

velocity optical phonon modes and creates additional scattering channels for Umklapp processes [7, 101, 8].

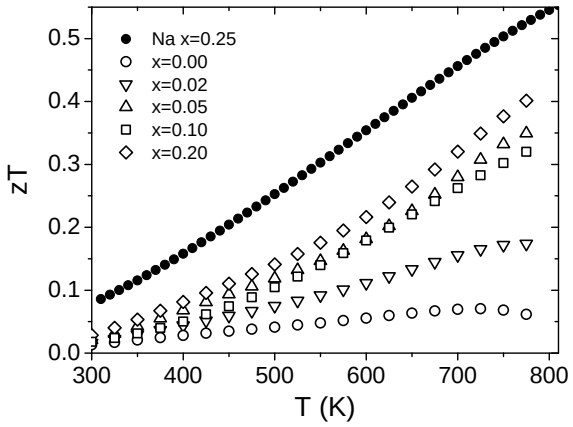

Figure 3.22: Compared to sodium-doped $Ca_5Al_2Sb_6$, the reduced mobility of the samples in this study lead to lower zT. Within the Zn series, the highest doped composition exhibits the largest zT.

Figure of Merit The figure of merit for the x = 0-0.2 compositions, calculated from the high temperature results presented above, is shown in Figure 3.22. Zn doping results in zT values that are lower than the sodium-doped sample (x=0.25). As the Zn x=0.1 and Na x=0.25 have nearly identical n_H, α, and κ_L, the overall decrease in the figure of merit is attributed solely to the reduced mobility in these Zn-doped samples. The x = 0.2 sample exhibits the highest zT values within the $Ca_5Al_{2-x}Zn_xSb_6$ series, suggesting that the limited doping levels available with Na-doping are insufficient to maximize performance.

Conclusion Our investigation of Zn-doped $Ca_5Al_2Sb_6$ shows this dopant provides excellent dopant effectiveness and yields higher hole carrier concentrations than previously obtainable with Na. Similar band mass and lattice thermal conductivity is observed for both Na and Zn dopants. However, the Zn-doped samples in this study exhibit reduced carrier mobility near room temperature compared to Na doping, possibly due to the relative decrease in grain size. Electronic structure calculations

suggest that the observed enhancement of the Seebeck coefficient at high carrier concentrations arises from a complex band structure.

3.3.3 Mn-doped $Ca_5Al_2Sb_6$

Introduction Carrier concentration control in $Ca_5Al_2Sb_6$ has been demonstrated with both Na and Zn as dopants [10, 125]. While Na-doped $Ca_5Al_2Sb_6$ results in the highest figure of merit, Na has the disadvantage of low solubility and low doping effectiveness. In contrast, Zn^{+2} substituted for Al^{+3} is a highly effective dopant, resulting in one free hole per dopant atom, in analogy to Zn substitution in $Yb_{14}MnSb_{11}$ [43].

Seeking to explore further opportunities for carrier concentration control in this material, the current study investigates Mn-doped $Ca_5Al_2Sb_6$. Like Zn, Mn is an appealing alternative dopant from a synthetic perspective, as it is less reactive than Na. Additional motivation for this study stems from the success of complete substitution of Mn for Al in the Zintl compound, $Yb_{14}AlSb_{11}$ [21]. In the $Yb_{14}Al_{1-x}Mn_xSb_{11}$ system, Mn assumes a valence of +2 and is a fully activated p-type dopant at all concentrations ($0< x <1$). However, Mn^{+2} is magnetic with spin $+5/2$, so the detrimental effect of spin disorder scattering may decrease the carrier mobility [43].

Chemical Characterization Ball milling and hot pressing of samples with nominal compositions $Ca_5Al_{2-x}Mn_xSb_6$ (x = 0.05, 0.1, 0.2, and 0.3) yielded polycrystalline ingots with densities above 98% of the theoretical density (4.313 g/cm^3) of $Ca_5Al_2Sb_6$, as determined by geometry. Scanning electron microscopy (SEM) of fracture surfaces (Figure 3.23 a and b) revealed grain sizes averaging between 1 and 10 μm for the x=0.1 sample and >10 μm in the remaining samples (x=0.05, 0.2, 0.3, 0.4). This disparity is attributed to differences in hot-pressing duration. Back-scatter SEM imaging (Figure 3.23c), along with energy dispersive X-ray spectroscopy, identified two secondary phases, $Ca_{11}Sb_{10}$ and $CaSb_2$, in each sample (<5% of each). The XRD

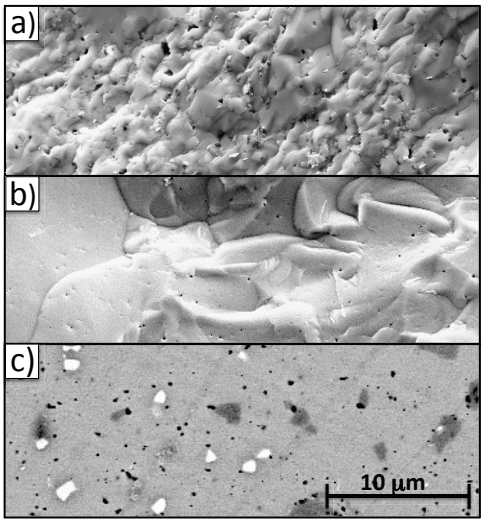

Figure 3.23: SEM images of fracture surfaces of (a) $x = 0.1$ and (b) $x = 0.3$ samples, hot pressed a total of 7 and 9 hours, yielding grain sizes of 1-10 μm and >10 μm, respectively. (c) Backscatter electron image of a polished surface (x=0.4) showing representative phase fractions of $Ca_5Al_{2-x}Mn_xSb_6$ (light grey), $Ca_{11}Sb_{10}$ (dark grey), and $CaSb_2$ (white).

patterns in Figure 3.24 confirm the presence of these two secondary phases in all but the x=0.1 sample.

With increased substitution of Mn on the Al site, Rietveld refinement of these patterns, based on the known $Ca_5Al_2Sb_6$ crystal structure, reveals that the lattice expands in the direction parallel to the tetrahedral chains (c), while the lattice parameter perpendicular to both the chains and the Sb-Sb bonds (b) decreases (Figure 3.25). These trends can be understood as the effect of expanding the $AlSb_4$ tetrahedra as the central Al^{3+} ion is replaced by the larger Mn^{2+} ion [155]. As the tetrahedra enlarge, the chains lengthen. This may cause the lattice parameters to contract in the plane perpendicular to the chains, explaining the observed decrease in b. The shape of the $AlSb_4$ tetrahedra may also change with Mn substitution, as was observed in $Yb_{14}AlSb_{11}$ [4]. The lattice parameter a shows no clear trend with Mn substitution.

Electronic Transport Properties Previous investigations of the electronic and thermal transport properties of undoped $Ca_5Al_2Sb_6$ revealed that it has the proper-

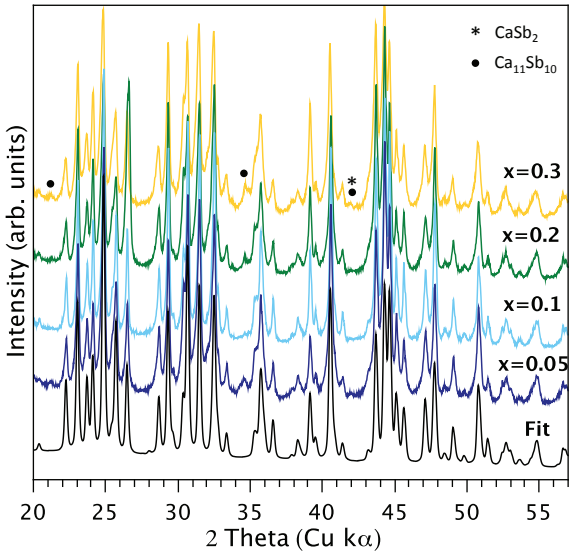

Figure 3.24: XRD patterns of polished polycrystalline samples of $Ca_5Al_{2-x}Mn_xSb_6$ (x = 0.05, 0.1, 0.2, and 0.3) and Rietveld fit using the known $Ca_5Al_2Sb_6$ structure. In most samples (x=0.05, 0.2, 0.3) peaks from minority phases $Ca_{11}Sb_{10}$ and $CaSb_2$ are also present.

ties of an intrinsic semiconductor with a band gap of 0.5 eV determined empirically from measurements of resistivity and Seebeck coefficient. Assuming 100% carrier activation, each Mn^{+2} on an Al^{+3} site should result in one free hole (h^+), yielding the trend in carrier concentration shown by the dashed line in Figure 3.26. Mn successfully hole dopes $Ca_5Al_2Sb_6$, leading to increased carrier concentration with increased dopant concentration. However, it is only partially effective at synthetic concentrations above x = 0.1, displaying a similar trend to that of the previously studied Na-doped system, but plateauing at a slightly lower hole concentration. While the discontinuity in hole concentration above x=0.1 suggests a low solubility limit of Mn in $Ca_5Al_2Sb_6$, such a conclusion is inconsistent with the comparatively linear changes observed in the lattice parameters with increasing Mn content. Although this inconsistency may be explained in part by compensating defects (i.e., $Mn^{2+} + 2e^-$), the full explanation remains unclear, and will require further investigation.

As shown in Figure 3.27a, high temperature Hall measurements of doped samples reveal extrinsic behavior, with relatively constant carrier concentrations to about

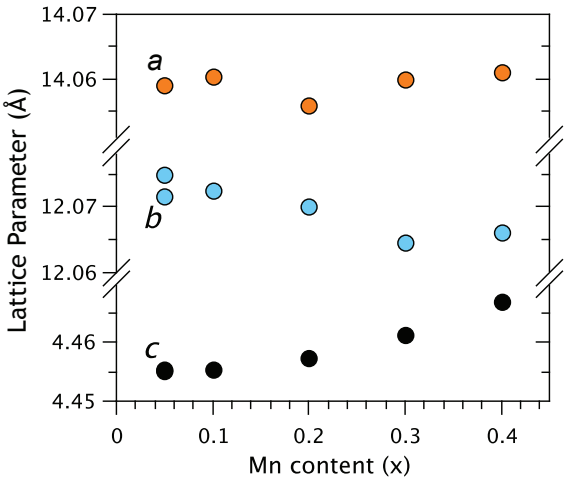

Figure 3.25: With substitution of the larger Mn^{2+} ions on the Al^{3+} site, the unit cell of $Ca_5Al_2Sb_6$ expands in the direction parallel to tetrahedral chains (c) and contracts in the direction perpendicular to both chains and Sb-Sb bonds (b).

850 K, at which temperature a slight increase is observed, possibly due to intrinsic carrier activation. Hall carrier mobility (Figure 3.27b) is found to decrease with temperature in Mn-doped samples according to the $\mu = T^{-\nu_a}$ dependence expected when acoustic phonons dominate scattering events ($\nu_a = 1$ and 1.5 for degenerate and non-degenerate semiconductors, respectively) [76]. As illustrated by the dashed line in Figure 3.27b (assumes ν_a=1), the high temperature mobility is well-described by this model, while the room temperature mobility is slightly lower than predicted. This slight suppression in mobility near room temperature manifests itself clearly in the negative slope of the resistivity between 300-350 K in some Mn-doped samples (Figure 3.27c). A more drastic reduction in mobility was observed in Zn-doped $Ca_5Al_2Sb_6$, attributed to a combination of small grain size and grain boundary oxidation. Indeed, of the samples discussed here, the x=0.1 sample has the smallest average grain size, and also the most apparent increase in resistivity at room temperature.

The inset in Figure 3.27b shows the dependence of Hall mobility on carrier concentration. In general, mobility decreases with increased carrier concentration, as illustrated by a single parabolic band model assuming that acoustic phonon scattering is the sole scattering mechanism (inset, solid curve). Within the accuracy of the

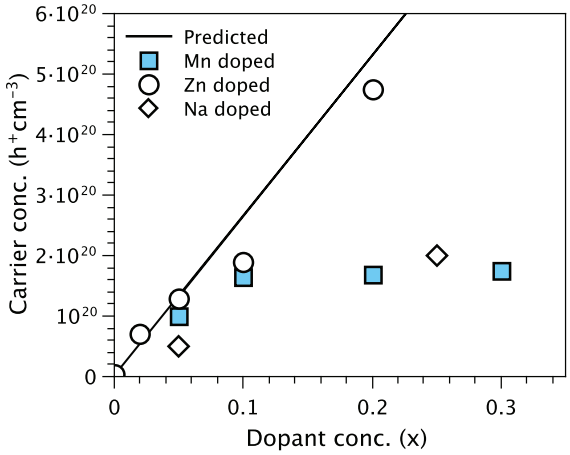

Figure 3.26: Room temperature Hall carrier concentrations increase with dopant concentration for Mn-, Zn-, and Na-doped $Ca_5Al_2Sb_6$. In practice, Na and Mn are not fully activated dopants relative to the predicted relationship assuming one free hole per dopant atom (solid line).

measurements, the Hall mobility of the Mn-doped samples in this study, as well as the Na-doped sample, behave roughly as expected. Given increased accuracy and a larger number of samples, it may be possible to more clearly observe the detrimental effect of boundary scattering and oxidation barriers in samples with small grains, as well as spin-disorder scattering in Mn-doped samples. The resistivity, shown in Figure 3.27c, of both the Mn- and the Na-doped samples generally increased with increasing temperature due to phonon scattering. However, due to its higher carrier concentrations and slightly higher mobility, the Na-doped sample has the lowest resistivity of the samples included here.

The Seebeck coefficients of $Ca_5Al_{2-x}Mn_xSb_6$ samples, shown in Figure 3.27, decrease in magnitude and exhibit a more linear dependence on temperature with increasing carrier concentration. At high temperatures, the Seebeck coefficients reach a broad maximum, as expected, due to thermal activation of minority carriers. A single parabolic band model was used to generate the Pisarenko plots shown in Figure 3.28, which relate carrier concentration to the Seebeck coefficient at 300 and 700 K (temperature regimes with little to no contribution from minority carriers). This model assumes acoustic phonons dominate scattering events, and has previously been

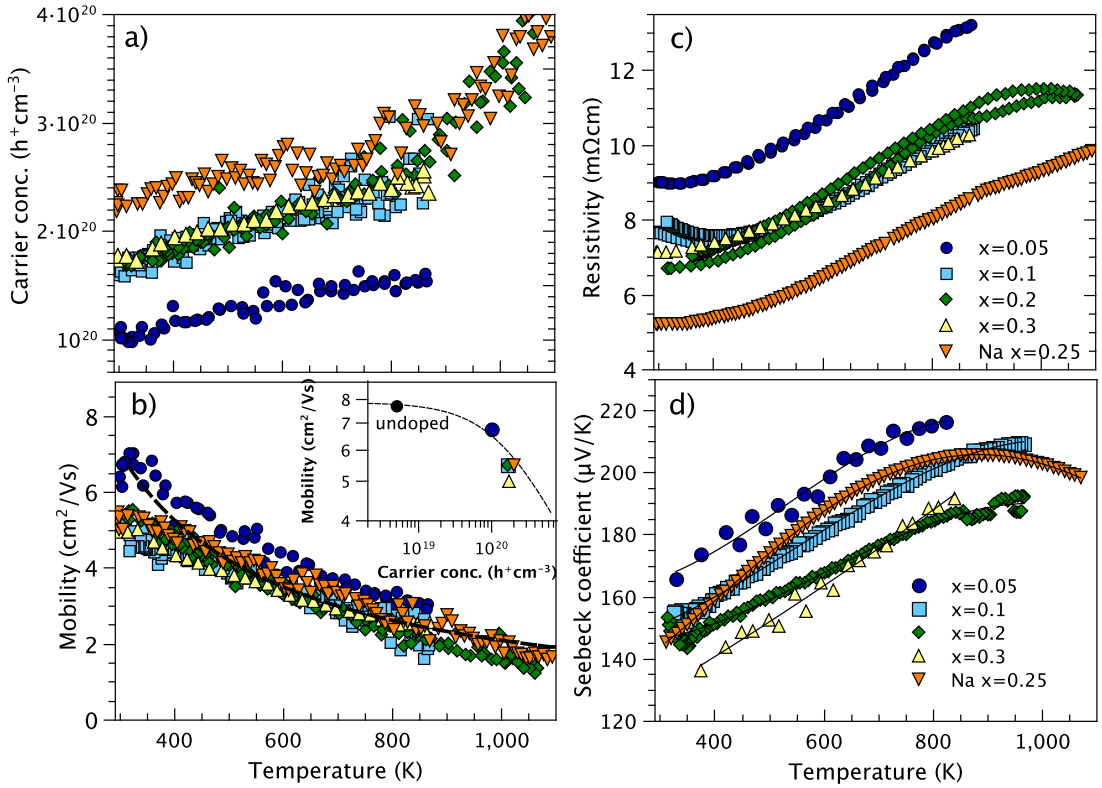

Figure 3.27: (a) Carrier concentrations of Mn- and Na-doped samples exhibit extrinsic behavior below 850 K. (b) Hole mobility decreases with temperature due to increased phonon scattering. Inset: With increasing carrier concentration, mobility decreases as predicted by a single parabolic band model (solid curve). (c) The resistivity in Na-doped $Ca_5Al_2Sb_6$ is significantly lower than in Mn-doped samples. (d) High temperature Seebeck coefficients display increasingly linear behavior and decreased magnitude with increased x.

described in detail for this material [10, 125]. A more thorough description can be found in ref. [6]. Na-, Zn-, and Mn- doped samples are relatively well-described by this model at low carrier concentrations. However, the Na-doped sample appears to have a slightly enhanced Seebeck coefficient relative to the Zn and Mn samples, most likely due to measurement variation resulting from the use of two different Seebeck measurement systems. At high carrier concentrations ($\sim$5x10^{20} h$^+$/cm^3), deviation from a parabolic band model is expected, as electronic structure calculations predict an additional, doubly degenerate band slightly below the valence band edge. Higher degeneracy in the band structure enhances the Seebeck coefficient, without

significantly affecting electronic mobility, potentially resulting in a peak zT at carrier concentrations beyond the optimal concentration predicted by a single band model [17, 19].

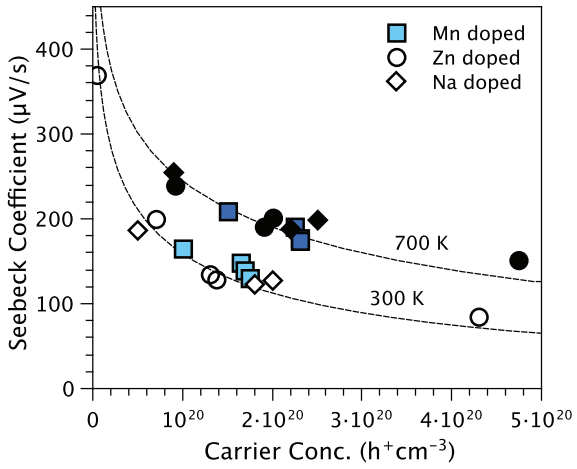

Figure 3.28: Experimental Seebeck coefficients at 300 and 700 K of Mn-, Zn-, and Na-doped $Ca_5Al_2Sb_6$. Solid curves were generated using a single parabolic band model with an effective mass of 1.8 m_e and 2.0 m_e for 300 K and 700 K, respectively.

Thermal Transport Properties The thermal conductivity is shown in Figure 3.29a. The electronic contribution to the thermal conductivity (κ_e) is estimated using the Wiedemann-Franz law ($\kappa_e = LT/\rho$), where the temperature dependent Lorenz numbers (L) are calculated from a single parabolic band model, as shown in the inset in Figure 3.29b. Subtracting κ_e from the total thermal conductivity gives the sum of the lattice (κ_L) and bipolar (κ_B) contributions, displayed in Figure 3.29b. There is no sign of a bipolar contribution in doped samples, and their κ_L follows the $1/T$ dependence expected when phonon transport is dominated only by Umklapp scattering, illustrated by the solid curve. As in the case of Na- and Zn- doped $Ca_5Al_2Sb_6$, no significant trend is observed between lattice thermal conductivity and dopant concentration. Due to their high degree of crystalline complexity, all samples exhibit a lattice thermal conductivity that approaches the minimum thermal conductivity predicted using the method of Cahill [80], at high temperature (dashed curve in Figure 3.29b) [7, 8].

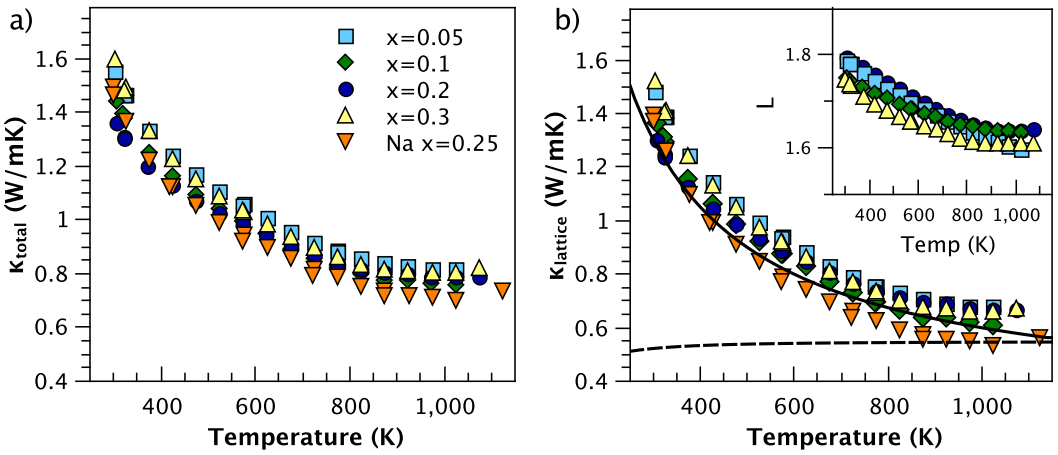

Figure 3.29: (a) Total thermal conductivity and (b) lattice thermal conductivity of $Ca_5Al_{2-x}Mn_xSb_6$ (x = 0.05, 0.1, 0.2, 0.3) and $Ca_{5-x}Na_xAl_2Sb_6$ (x = 0.25) samples. The inset shows the temperature dependence of the Lorenz numbers in units of 10^8 $W\Omega K^{-2}$, calculated using a single para-bolic band model.

Figure of Merit Figure 3.30 compares the figures of merit previously calculated for $Ca_{4.75}Na_{0.25}Al_2Sb_6$ to those calculated for the $Ca_5Al_{2-x}Mn_xSb_6$ samples using polynomial fits to the high temperature measurements of transport properties discussed above. Within the measured temperature range, a maximum zT of 0.4 occurs in x = 0.1 and x = 0.3 Mn-doped samples. These values are lower than those obtained with Na doping, most likely due to the use of a different Seebeck measurement system in this study. In general, the combined measurement uncertainty in the figure of merit is up to 20%.

Conclusions Investigation of the $Ca_5Al_2Sb_6$ Zintl phase reveals that it can be successfully p-doped with Mn. Transport properties follow the expected trends of a p-type, extrinsic semiconductor, and the lattice thermal conductivity approaches the glassy limit at high temperature, as might be expected for a material with a highly complex crystal structure. However, carrier concentration control with Mn is not improved relative to that achieved with Na or Zn, and the transport properties, though comparable, are found to be superior in the Na-doped system.

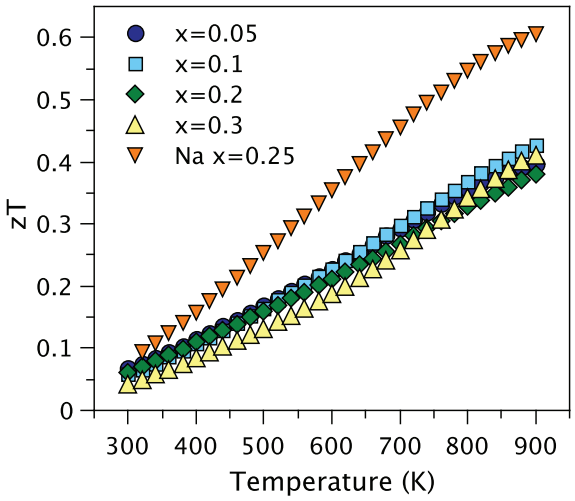

Figure 3.30: The figure of merit of $Ca_5Al_{2-x}Mn_xSb_6$ samples remains below that of $Ca_{5-x}Na_xAl_2Sb_6$ within the measured temperature range.

3.4 Optimization of $Ca_5Ga_2Sb_6$ via Zn doping

Introduction The comparison of undoped $Ca_5M_2Sb_6$ compounds (M =Al, Ga, In) in Section 3.2 showed decreased phonon velocities and improved electronic mobility in the undoped Ga and In analogues relative to undoped $Ca_5Al_2Sb_6$ [74]. This motivates us to study $Ca_5Ga_2As_6$, despite the disadvantage of the increased cost of Ga relative to Al. $Ca_5Ga_2As_6$, like the Al analogue, requires doping to optimize its electronic properties and realize its maximum possible zT. We have previously shown that $Ca_5Al_2As_6$ can be doped with Na on the Ca site, or with Zn or Mn on the Al site, to increase the p-type carrier concentration, thereby drastically improving the zT [125, 64]. Zn doping yielded the best control of the carrier concentration, and is therefore used here. This study explores the properties of $Ca_5Ga_{2-x}Zn_xSb_6$, with x ranging from 0 to 0.3. We use a combination of high temperature electronic and thermal transport measurements and simple modeling assuming a single parabolic band to characterize and optimize the thermoelectric properties of this system.

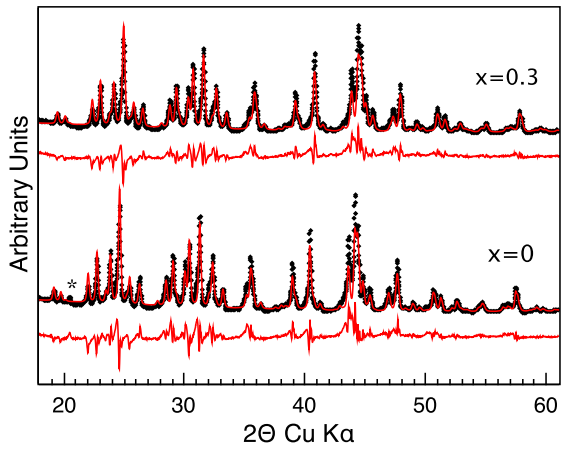

Figure 3.31: XRD patterns of $Ca_5Ga_{2-x}Zn_xSb_6$ ($x = 0$ and $x = 0.3$) are shown in black. A small amount of the secondary phase $CaSb_2$ was observed in all samples. In the sample with $x = 0$, the asterisk denotes a reflection from $CaSb_2$. The simulated Rietveld fits are overlaid in red, and the difference profile is shown in red underneath.

Chemical Characterization The phase purity of the $Ca_5Ga_{2-x}Zn_xSb_6$ ($x = 0$, 0.05, 0.1, 0.2, 0.3) samples and the reference sample was determined by X-ray diffraction (XRD) and scanning electron microscopy (SEM). Representative patterns of the $x = 0$ and $x = 0.3$ samples can be seen in Figure 3.31. The simulated Rietveld fits and difference profiles are also shown. The reflection denoted by an asterisk in the undoped sample is a secondary phase, identified as $CaSb_2$ using energy dispersive spectroscopy (EDS). In all of the $Ca_5Ga_{2-x}Zn_xSb_6$ ($x = 0$, 0.05, 0.1, 0.2, 0.3) samples, a small fraction ($\sim$1 volume %) of this secondary phase was observed during SEM analysis (visually determined from the estimated ratio of the $CaSb_2$ area to that of the matrix phase). The $CaSb_2$ content does not appear to increase with Zn concentration. The geometric density of the samples ranges from 97-98% of the theoretical density, and grain sizes for the samples, estimated from SEM analysis of fracture surfaces, range from 1-5 μm.

For comparison, an Al-based sample ($Ca_5Al_{1.9}Zn_{0.1}Sb_6$) was also synthesized for this study. The Al-based reference sample was synthesized using the method described for the samples in Section 3.3.2 with one exception: the hot pressing temperature was increased from 873 K to 1073 K to correct for the extremely low mobility in our initial

study of Zn-doped $Ca_5Al_2Sb_6$.

Electronic Transport Properties Our initial investigation of the $Ca_5M_2Sb_6$ compounds (M = Al, Ga, In) revealed non-degenerate semiconducting behavior and low p-type carrier concentration ($\sim 10^{18}$ h^+/cm^3) in all three compounds [74]. Relative to the Al- and In-based compounds, $Ca_5Ga_2Sb_6$ samples exhibited both a reduced band gap (E_g), determined from high temperature resistivity and Seebeck measurements, and improved hole mobility. These experimental results were consistent with density functional theory (DFT) calculations, which predicted a lighter valence band effective mass (m^*) and a smaller E_g ($\sim$0.4 eV) arising from the low energy (relative to Al-Sb or In-Sb) Ga-Sb anti-bonding states at the conduction band edge [74]. In thermoelectric materials, light m^* and the corresponding high mobility are desirable in [73], while a small band gap can be detrimental, particularly at high temperature materials.

To optimize the electronic properties of $Ca_5Ga_2Sb_6$, electronic doping is necessary. Motivated by the successful use of Zn^{2+} as a dopant in $Ca_5Al_2Sb_6$ [125], here we substitute Zn^{2+} on the Ga^{3+} site. Simple valence counting predicts that each Zn substitution will yield one free hole. This simple assumption is accurate at low Zn concentrations, as illustrated by the inset in Figure 3.32a. The room temperature Hall carrier concentration, n_H, is similar to the theoretical carrier concentration, n, (dashed line) for $x < 0.2$, but diverges when $x > 0.3$. This divergence might be explained by a low solubility of Zn in this system or by the formation of compensating n-type defects.

As the Hall carrier concentration increases in magnitude, the temperature dependence exhibits a transition from intrinsic to extrinsic semiconducting behavior, as shown in Figure 3.32a. In the undoped sample, n_H increases exponentially due to intrinsic carrier activation, resulting in a change in the majority carrier type above 650 K (unfilled blue symbols indicate negative data) as discussed in Section 3.2. In contrast, the temperature independent carrier concentrations of the doped samples are indicative of metallic behavior with transport dominated by extrinsic carriers.

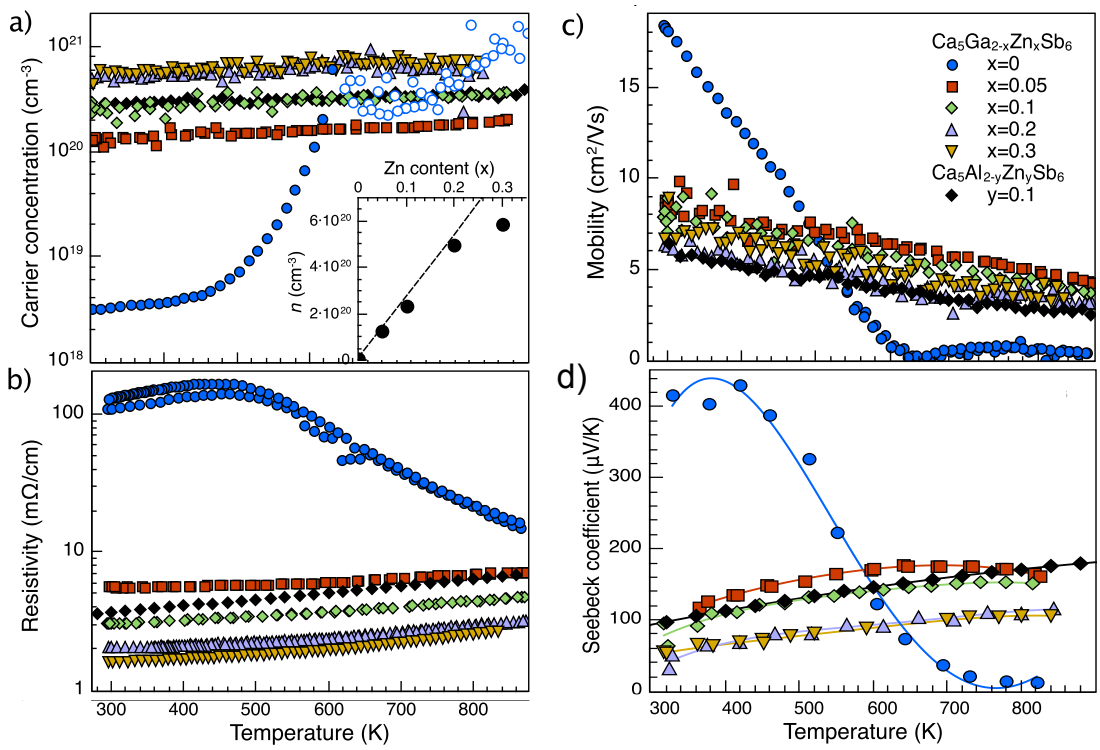

Figure 3.32: (a) The Hall carrier concentration, n_H, increases with increased Zn content, x. Inset: n_H begins to deviate from the expected values shown by the dashed line above x=0.2. (b) Resistivity decreases with increasing n_H, showing a transition from intrinsic semiconducting to metallic behavior. (c) Hall mobility decreases with increasing x, but is improved relative the Al-analogue, $Ca_5Al_{1.9}Zn_{0.1}Sb_6$. (d) The Seebeck coefficient decreases in magnitude and exhibits an increasingly linear temperature dependence with increasing Zn.

For comparison, we have included a representative $Ca_5Al_{2-y}Zn_ySb_6$ sample with $y = 0.1$. In comparably doped Al and Ga analogues, the carrier concentration values and trends are in agreement. As shown in Figure 3.32b, with increasing x, the resistivity (ρ) decreases by nearly two orders of magnitude due to the increase in hole concentration. In the doped samples, resistivity increases with temperature due to decreasing hole mobility (Figure 3.32c).

The Hall mobility (μ) is shown in Figure 3.32c. At room temperature, μ in the undoped sample is more than twice that of the doped samples. The mobility of the doped samples, in general, decreases with increasing x, but remains higher than observed in either Na- or Zn-doped $Ca_5Al_2Sb_6$. Note that the Al-based reference

sample synthesized for this study has higher mobility than the samples in our previous report on Zn-doped $Ca_5Al_2Sb_6$ [125]. This may be due to improved microstructure (larger grain size) resulting from the increased hot pressing temperature used in the current study. Compared with $Ca_5Al_{1.9}Zn_{0.1}Sb_6$, the mobility of $Ca_5Ga_{1.9}Zn_{0.1}Sb_6$ is improved by $\sim$20%, which is beneficial to the compound's performance and figure of merit. In all doped samples, the temperature dependence of μ is indicative of acoustic phonon scattering [76]. For all Zn-doped samples in this study, ν ranges from 1.3 to 1.7. Note that the near-zero mobility above 600 K in the undoped sample stems from the assumption of a single carrier type, and does not represent the true drift mobility of the holes (See Chapter 3.2).

The Seebeck coefficients (α) are shown in Figure 3.32 up to 873 K. With increasing x, the Seebeck coefficients decrease and exhibit increasingly linear temperature dependences. Relative to $Ca_5Al_{2-y}Zn_ySb_6$ (plotted for $y = 0.10$ case), the reduction of α in $Ca_5Ga_{2-x}Zn_xSb_6$ samples due to minority carriers begins at lower temperature as a result of the smaller band gap in the latter system.

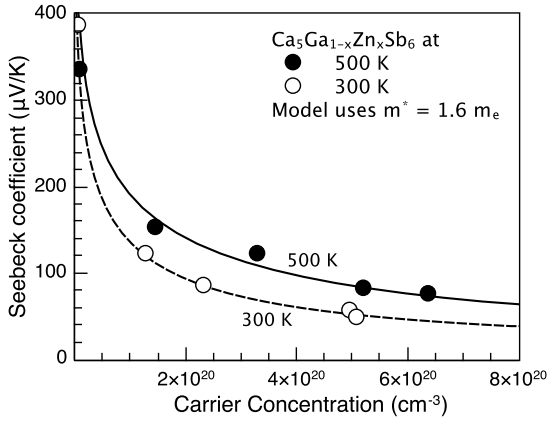

Figure 3.33: The experimental Seebeck coefficients of $Ca_5Ga_{2-x}Zn_xSb_6$ at $T = 300$ and 500 K are compared with a single parabolic band model, showing general agreement. An effective mass of 1.6 m_e was used for both temperatures.

The relationship between α and n_H (shown in Figure 3.33) is well-described by a single parabolic band model (SPB), assuming an effective mass of 1.6 m_e and that acoustic phonons are the primary scattering source. A more detailed description of

this model can be found in references [6, 10]. A single band model cannot account for minority carriers effects at high temperature, and is thus only used to 500 K. Consistent with prior DFT results, which predicted a lighter valence band in $Ca_5Ga_2Sb_6$ relative to both the In and Al analogues, our experimental effective mass of 1.6 m_e is significantly lower than that observed in $Ca_5Al_2Sb_6$ samples (2.2 m_e). In all $Ca_5M_2Sb_6$ compounds, the calculated band structures predict significant deviations from parabolic behavior when the Fermi energy is far from the band edge, as expected from heavy doping. Since higher carrier concentrations were obtained in $Ca_5Ga_2Sb_6$ compared with the Al analogue, this system provides an opportunity, in principle, to experimentally probe deeper into the valence band. However, we are unable to confirm the expected non-parabolic behavior, as even the most heavily doped samples are reasonably well-described by a constant effective mass, within experimental error.

Thermal Transport Properties The total thermal conductivity is shown in Figure 3.34a. The total thermal conductivity is the sum of three components: the electronic (κ_e), bipolar (κ_B), and lattice (κ_L) contributions. The electronic component is estimated from the Wiedemann-Franz equation, $\kappa_e = \frac{LT}{\rho}$, where L is the Lorenz number calculated using the SPB model (shown in the inset in Figure 3.34). Thus, the total thermal conductivity tends to increase with increasing dopant concentration, as ρ decreases. Comparison with the y=0.1 case of $Ca_5Al_{2-y}Zn_ySb_6$ is shown as well.

Lattice thermal conductivity (Figure 3.34b) is obtained by subtracting κ_e from κ_{total}, providing that the bipolar contribution is negligible. This is clearly not the case for the undoped material, in which κ_{total}-κ_e rises with temperature above 600 K, indicating that there is a significant bipolar contribution. In contrast, the Zn-doped samples show no obvious indication of a bipolar contribution; in these, κ_{total}-κ_e decreases with temperature approximately as 1/T, characteristic of lattice thermal conductivity limited by Umklapp phonon-phonon scattering [8].

The minimum lattice thermal conductivity (κ_{min}) [80, 121] places a theoretical lower limit on κ_L, which derives from the minimum allowed scattering distance ($l = \lambda/2$) for phonons with wavelength λ. At high temperatures, κ_{min} can be approximated

by 3.9, where V is the average volume per atom and ν_T and ν_L are the transverse and longitudinal sound velocities, respectively. Ultrasonic measurements of ν_T and ν_L for undoped $Ca_5M_2Sb_6$ compounds (M = Al, Ga, In) are detailed in Ref. [74]. Relative to $Ca_5Al_2Sb_6$, the higher density and lower stiffness in $Ca_5Ga_2Sb_6$ lead to lower speed of sound, and thus lower κ_{min}:

$$\kappa_{min} = \frac{1}{2}\left(\frac{\pi}{6}\right)^{1/3} k_B V^{-2/3}(2\nu_S + \nu_L) \tag{3.9}$$

The dashed line in Figure 3.34b denotes the estimated κ_{min} for $Ca_5Ga_2Sb_6$. Unlike in doped $Ca_5Al_2Sb_6$ samples (of which the x=0.10 case is plotted), which reach the predicted κ_{min} at high temperatures, κ_L in Zn-doped $Ca_5Ga_2Sb_6$ remains conspicuously high. This may suggest that a small, but not negligible, bipolar contribution is present even in the most heavily Zn-doped samples.

Figure of merit The figures of merit for $Ca_5Ga_{2-x}Zn_xSb_6$ samples, calculated using polynomial fits to the experimental data, are shown in Figure 3.35. At low temperatures, the effect of the increased mobility in the Ga compound dominates, leading to an apparent improvement in zT from 400 to 750 K relative the Al-based material. This may be due to the reduced effective mass in $Ca_5Ga_2Sb_6$: when acoustic phonons dominate the charge carrier scattering, the quality factor, which determines the zT of optimally doped materials, is given by $\beta \propto \frac{N_v}{m_i^* \kappa_L}$ [73](m_i^* is the mass of a single hole pocket along the conduction direction and N_v is the number of bands contributing to transport). Note however that the zT improvement in this study is within the generally accepted uncertainty in zT of about 20%.

Compared with optimally Zn-doped $Ca_5Al_2Sb_6$, the zT in Zn-doped $Ca_5Ga_2Sb_6$ is detrimentally affected by minority carriers at high temperature, leading to a lower peak zT. A maximum zT of about 0.35 is reached at 775 K in the samples with x = 0.05 and x = 0.1 sample. Beyond x = 0.1, the maximum zT decreases, suggesting that the optimal doping level for this compound is surpassed. Using an SPB model at 500 K with m^* = 1.6 m_e, and an intrinsic mobility of 9 cm^2/Vs, we estimate an optimal carrier concentration of $\sim 10^{20}$ $h^+ cm^{-3}$. This corresponds to the most lightly

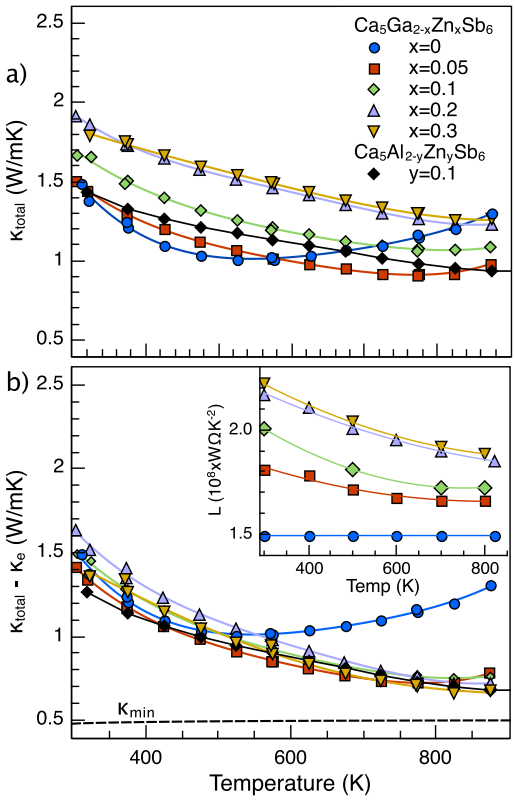

Figure 3.34: (a) The total and (b) lattice thermal conductivity in $Ca_5Ga_{2-x}Zn_xSb_6$. The inset shows the Lorenz numbers, calculated from the SPB model using experimental Seebeck coefficients.

doped sample ($x = 0.05$), consistent with the experimental results.

Conclusion In this study, $Ca_5Ga_2Sb_6$ was successfully p-doped with Zn, leading to metallic behavior and greatly improved thermoelectric properties. The Ga-based material, when optimally doped, exhibits an increased mobility over the Al analogue, attributed to the reduced effective mass predicted by DFT calculations. The reduction in effective mass was also reflected in the measured Seebeck coefficients at 300 K and 500 K; a single band model yielded $m^* = 1.6$ m$_e$ in Zn-doped $Ca_5Ga_2Sb_6$ in contrast to m* = 2.0me in $Ca_5Al_2Sb_6$. Additionally, detrimental effects from the smaller band gap in $Ca_5Ga_2Sb_6$ were observed: minority carrier activation leads to both compensated Seebeck coefficients and bipolar thermal conductivity at high temperatures. The high cost of Ga must also be considered. Ultimately, the improved electronic mobility of the

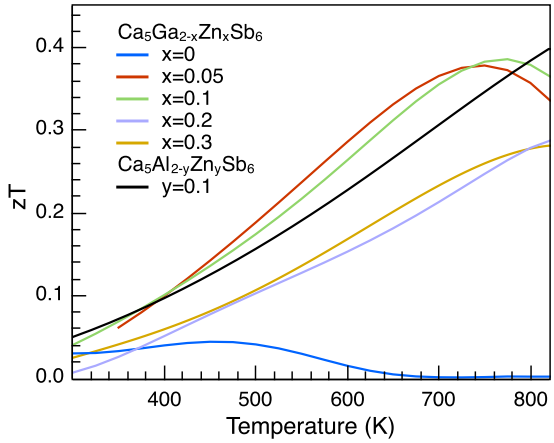

Figure 3.35: The figure of merit of $Ca_5Ga_{2-x}Zn_xSb_6$ reaches a maximum of ∼0.35 at 750 K for samples with $x = 0.05$ and $x = 0.1$. The magnitude and temperature of the peak zT are reduced relative to the Al analogue due to the smaller band gap in $Ca_5Ga_2Sb_6$.

Ga compound yields a small increase in zT between 400-800 K relative to Zn-doped $Ca_5Al_2Sb_6$ analogue. However, due to the reduced band gap, and hence the reduced Seebeck coefficient and high bipolar thermal conductivity of $Ca_5Ga_{1-x}Zn_xSb_6$, the peak zT is lower than the Al analogue.

3.5 Optimization of $Ca_5In_2Sb_6$ via Zn doping

Reproduced with permission from *Dalton Trans.* **42**, 9713-9719 (2013).

Introduction Relative to $Ca_5Al_2Sb_6$, the In- and Ga-based compounds exhibit improvements to both the electronic and thermal properties; the lattice thermal conductivity was reduced due to higher density and reduced stiffness, which in turn decreases the speed of sound ($\nu \propto \sqrt{E/d}$, where E is stiffness and d is density), and the electronic mobility was improved. In contrast to $Ca_5Ga_2Sb_6$, which had a significantly reduced band gap relative to the Al analogue and thus reduced performance at high temperatures [126], the band gap of $Ca_5In_2Sb_6$ is very similar to that of the Al analogue. Upon optimization of the carrier concentration through doping,

$Ca_5In_2Sb_6$ is thus expected to have an improved peak zT relative to both $Ca_5Al_2Sb_6$ and $Ca_5Ga_2Sb_6$.

The current study investigates the electronic and thermal properties of $Ca_5In_{2-x}Zn_xSb_6$ (x=0, 0.02, 0.05, 0.1, 0.2). Zn^{2+} acts as a p-type dopant on the In^{3+} site in the otherwise charge-balanced $Ca_5In_2Sb_6$, allowing the study of samples with a wide range of carrier concentrations. We use solutions to the Boltzmann transport equation, assuming rigid, single parabolic band behavior to analyze transport data and to guide in the optimization of the carrier concentration and the figure of merit.

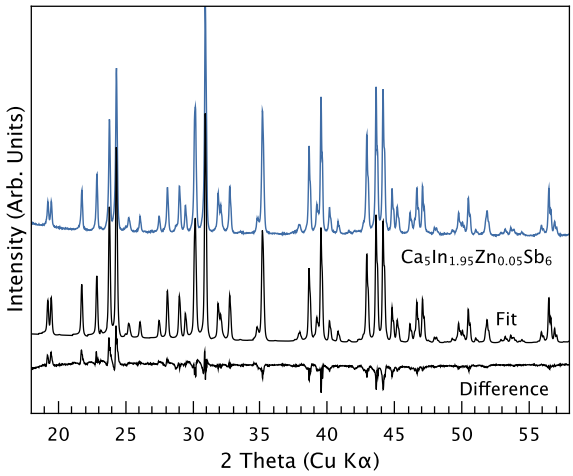

Figure 3.36: XRD pattern of a polycrystalline slice of the $x = 0.05$ sample, Rietveld fit using the known $Ca_5In_2Sb_6$ structure, and difference profile.

Chemical Characterization The phase purity of the hot-pressed $Ca_5In_{2-x}Zn_xSb_6$ (x=0, 0.02, 0.05, 0.1, 0.2) samples was confirmed by X-ray diffraction (XRD) and scanning electron microscopy (SEM). Figure 3.36 shows a representative XRD pattern, a Rietveld fit using the known crystal structure of $Ca_5In_2Sb_6$ [9], and the difference profile. From the XRD patterns, all of the samples in this study appear to be phase pure. However, an unidentified secondary phase is visible as ∼100 nm white flecks in the backscatter electron image in Figure 3.37a. This impurity appears to make up less than 1 vol.% of the sample, and is not expected to have a significant impact on transport properties. The lattice parameters obtained from Rietveld refine-

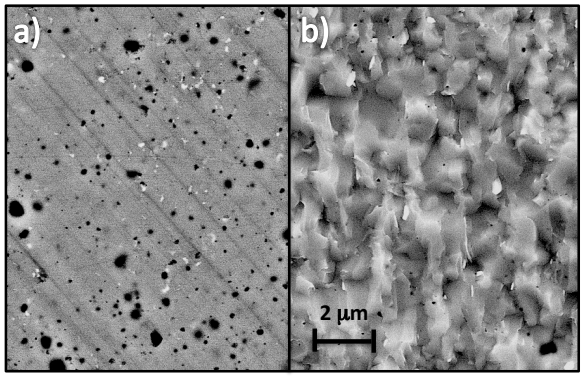

Figure 3.37: (a) Backscattered electron image of a polished surface of $Ca_5In_{1.9}Zn_{0.1}Sb_6$ showing representative fractions of $Ca_5In_2Sb_6$ (grey), a secondary phase (light grey), and pores (black). (b) Secondary electron image of a fracture surface of the same sample reveals grain sizes on the order of 1 μm.

ments suggest that the $Ca_5In_{2-x}Zn_xSb_6$ system is a solid solution up to only $x = 0.05$. The ionic radii of four-coordinated Zn^{2+} and In^{3+} are respectively 0.60 and 0.62 Å. As expected, with increasing Zn content, the unit cell volume was found to decrease. However, above $x = 0.05$ the volume remained constant. The light grey impurity observed in SEM images appears in similar concentrations in all samples (both doped and undoped), and is therefore not likely to be due to the addition of Zn. However, given the low solubility of Zn in $Ca_5In_2Sb_6$, additional, Zn-rich secondary phases are likely present in the samples with x=0.1 and x=0.2.

The samples' geometric densities range from 95-97% of the theoretical density (4.90 g/cm^3), consistent with the fraction of pores observed in SEM analysis. SEM images of fracture surfaces (Figure 3.37b) reveal grain sizes on the order of a few microns. This is similar to Zn-doped $Ca_5Al_2Sb_6$ samples [125], but small compared to Na-doped $Ca_5Al_2Sb_6$, which had average grains sizes of 50-100 μm [10]. Attempts to increase the grain size in $Ca_5In_2Sb_6$ by doubling the hot pressing time did not lead to an appreciable difference. Neither the density nor grain size appear to be a function of Zn concentration.

Electronic Transport Properties $Ca_5In_2Sb_6$ is a classic, valence-precise Zintl compound, in common with the Al and Ga analogues of the same structure. In prac-

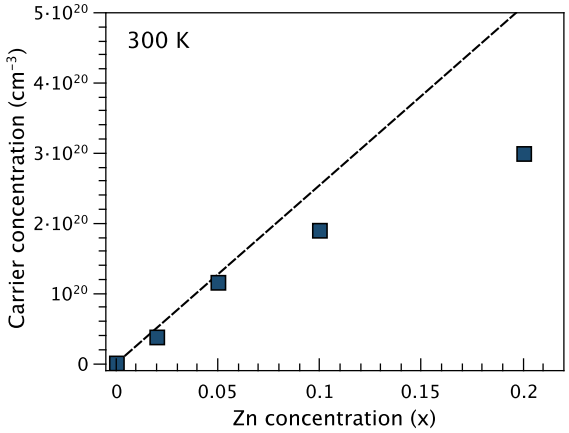

Figure 3.38: With increasing Zn content, the Hall carrier concentration at 300 K in $Ca_5In_{2-x}Zn_xSb_6$ increases as predicted by simple charge counting (dashed line) up to $x = 0.05$

tice, nominally undoped $Ca_5In_2Sb_6$ samples were found to be lightly hole doped (n = 5x10^{18} h$^+$/cm^3) at room temperature. The room temperature carrier concentrations were shown to be similar in all three $Ca_5M_2Sb_6$ compounds, suggesting that the M atom does not affect the equilibrium concentration of intrinsic crystalline defects [74].

Upon doping, simple charge counting predicts that each Zn^{2+} on an In^{3+} site will lead to one free hole. The predicted relationship between carrier concentration (n) and x is shown as a dashed line in Figure 3.38. At low doping levels, the measured Hall carrier concentration (n_H) increases according to the predicted trend, but n_H diverges downwards for $x > 0.05$ (Figure 3.38). The reduced doping effectiveness above $x = 0.1$ is most likely a result of limited Zn solubility. This is qualitatively consistent with our XRD data, which suggests that $Ca_5In_{2-x}Zn_xSb_6$ is only a true solid solution up to x=0.05.

Shown in Figure 3.39a, n_H in undoped $Ca_5In_2Sb_6$ increases strongly as a function of temperature due to activation of minority carriers across the band gap. This leads to the decrease in resistivity (ρ) with temperature characteristic of intrinsic semiconductors (Figure 3.39b). As discussed in Section 3.2, the discontinuity in the Hall and resistivity measurements at 725 K is due to a reversible phase transition, confirmed by DSC measurements in both undoped and doped $Ca_5In_2Sb_6$. With increasing Zn

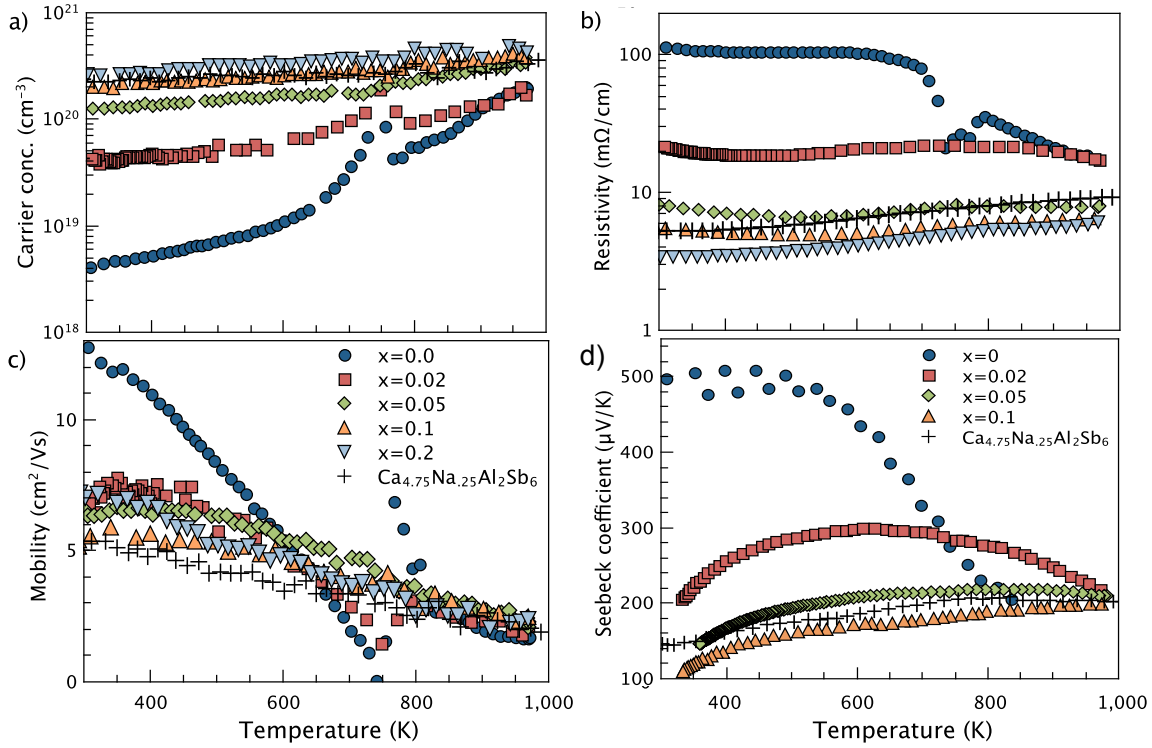

Figure 3.39: (a) With increasing x in $Ca_5In_{2-x}Zn_xSb_6$, the carrier concentration increases and (b) the resistivity decreases by an order of magnitude. (c) The Hall mobility decreases with Zn content, becoming comparable to Na-doped $Ca_5Al_2Sb_6$ at high temperatures. (d) High temperature Seebeck coefficients of $Ca_5In_{2-x}Zn_xSb_6$ samples display increasingly linear behavior and decreased magnitude with increased Zn concentration.

content, n_H in $Ca_5In_{2-x}Zn_xSb_6$ increases by nearly two orders of magnitude, and becomes less temperature dependent, as shown in Figure 3.39a. Correspondingly, the resistivity decreases and the temperature dependence transitions from semiconducting to metallic. Shown for comparison, the carrier concentration of optimally doped $Ca_{4.75}Na_{0.25}Al_2Sb_6$ from Chapter 3.3.1 (reference [10]) is equivalent to that of $Ca_5In_{1.9}Zn_{0.1}Sb_6$. Note that doping with Zn in $Ca_5In_2Sb_6$ increases n_H more effectively than Na in $Ca_5Al_2Sb_6$. Higher doping effectiveness is the primary reason that Zn, rather than Na, was used as a dopant in this study.

The Hall mobility (μ_H), calculated from $\rho = 1/n_H e\mu_H$, is shown in Figure 3.39c. In both doped and undoped $Ca_5In_{2-x}Zn_xSb_6$ samples, the temperature dependence of μ at high temperatures is consistent with acoustic phonon scattering ($\mu \propto T^{-\nu}$, where

ν ranges from 1.5 to 2.5). At room temp, the mobility of undoped $Ca_5In_2Sb_6$ is nearly twice that of undoped $Ca_5Al_2Sb_6$ (see ref [74]). With increased Zn doping however, the mobility decreases rapidly. Comparing $Ca_5Al_2Sb_6$ and $Ca_5In_2Sb_6$ samples with the same carrier concentrations reveals that $Ca_5In_{2-x}Zn_xSb_6$ has slightly higher mobility than Na-doped $Ca_5Al_2Sb_6$. However, the improvement is not as strong as observed in the undoped samples.

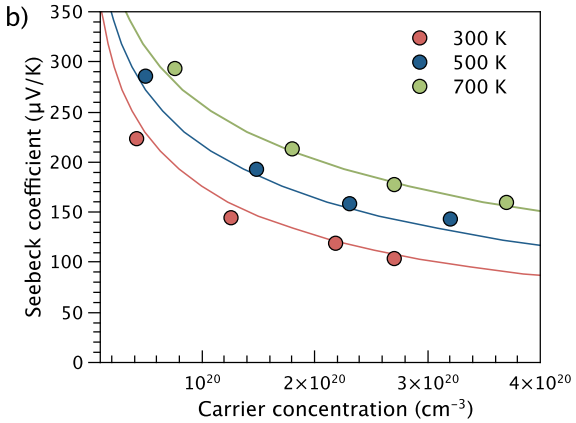

Figure 3.40: The Seebeck coefficients decrease as a function of n as predicted by a single parabolic band model (solid curves). Effective masses of 2.0 m_e (at 300 K and 500 K) and 1.8 m_e (at 700 K) were calculated from the experimental α and n_H of the $x = 0.05$ sample.

$Ca_5In_2Sb_6$ has a large, positive Seebeck coefficient, which decreases with temperature due to thermally activated minority carriers (Figure 3.40d). With doping, the transition from non-degenerate to degenerate behavior leads to a decrease in the magnitude of the Seebeck coefficients, as well as a more linear temperature dependence. Due to their similar carrier concentrations, the samples $Ca_5In_{1.9}Zn_{0.1}Sb_6$ and $Ca_{4.75}Na_{0.25}Al_2Sb_6$ have comparable Seebeck coefficients.

In ref [74], we reported a slight decrease in both the band gap and effective mass of $Ca_5In_2Sb_6$ relative to the Al analogue. This could be understood qualitatively in terms of the electronegativity difference between Al and In (1.61 and 1.78 respectively on the Pauling scale) and was supported by Density Functional calculations. While the influence of the modified electronic band structure was observed experimentally

in undoped $Ca_5M_2Sb_6$ compounds, it does not appear to have a large influence on the electronic mobility and Seebeck coefficients of the doped samples.

Figure 3.40 illustrates the dependence of the Seebeck coefficient on n_H, which is determined by the geometry of the valence band. The solid curves show the predicted dependence at selected temperatures, assuming a parabolic valence band edge. This model assumes that acoustic phonons are the dominant scattering source. A more complete description of this SPB model can be found in ref [6, 10]. The effective mass of $Ca_5In_2Sb_6$, as determined by an SPB model ($m^* = 2\ m_e$ at 300 and 500 K, and 1.8 m_e at 700 K) is similar to that found in $Ca_5Al_2Sb_6$.

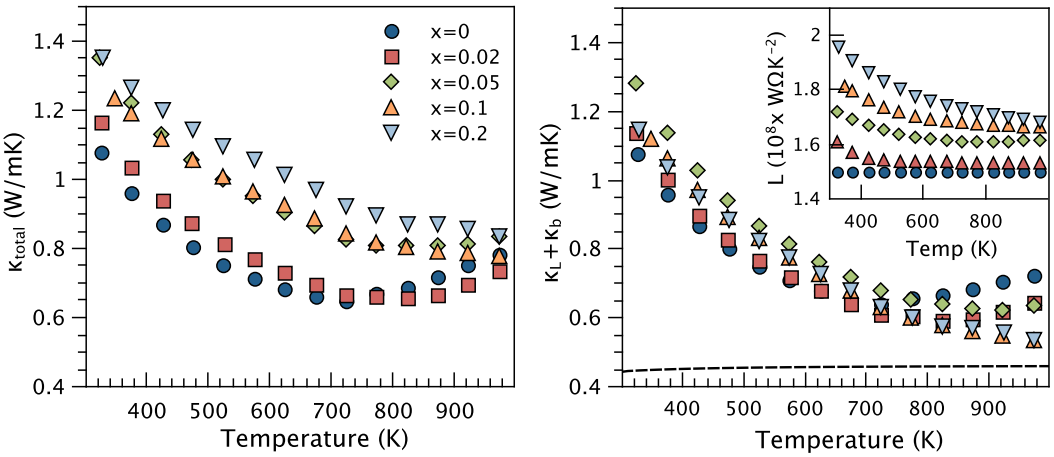

Figure 3.41: (a) The total thermal conductivity and (b) the combined lattice and bipolar thermal conductivity of $Ca_5In_{2-x}Zn_xSb_6$. The inset shows the temperature dependence of the Lorenz numbers in units of 10^8 WΩK^{-2}, calculated using an SPB model.

Thermal Transport Properties Due primarily to the complexity of its unit cell (26 atoms per cell), the lattice thermal conductivity in $Ca_5Al_2Sb_6$ was found to approach κ_{min} at the temperature corresponding to its maximum zT ($\sim$ 1000 K) [8, 7]. While nanostructuring or point defect scattering may further reduce κ_L at low temperatures, such strategies are not expected to reduce the high temp κ_L beyond the minimum (κ_{min}) predicted by Eq. 3.10. One potential route to further reductions

in κ_L at high temperature is to reduce κ_{min} itself, which can be accomplished by lowering the speed of sound.

$$\kappa_{min} = \frac{1}{2}\left(\frac{\pi}{6}\right)^{1/3} k_B V^{-2/3}(2\nu_S + \nu_L) \tag{3.10}$$

The speed of sound in a solid increases with stiffness and decreases with density according to equations 3.11 and 3.12. The substitution of In for Al in $Ca_5M_2Sb_6$ led to a 10% reduction in the speed of sound due to both increased density and decreased stiffness [74].

Table 3.3: For $Ca_5In_2Sb_6$ and $Ca_5Al_2Sb_6$, d is theoretical density, D is thermal diffusivity at 325 K and κ_{min} is the minimum lattice thermal conductivity at high temperature ($T > \Theta_D$)

	d	G	K	ν_T	ν_L	D	κ_{min}
	g/cm^3	GPa	GPa	m/s	m/s	mm^2/s	W/mK
Al	4.31	25	40	2400	4100	0.98	0.53
In	4.90	22	38	2115	3710	0.82	0.46

$$\nu_S = \sqrt{\frac{G}{d}} \tag{3.11}$$

$$\nu_L = \sqrt{\frac{K + \frac{4}{3}G}{d}} \tag{3.12}$$

The total thermal conductivity is shown in Figure 3.41a. The electronic component of the thermal conductivity is estimated from the Wiedemann-Franz relation ($\kappa_e = LT/\rho$), where the Lorenz number (L) is determined using the SPB model described in ref [6] (Inset in Figure 3.41b). At temperatures beyond the onset of minority carrier activation, L was determined by extrapolation. Subtracting the electronic contribution from κ leaves both the lattice and bipolar terms, shown in Figure 3.41b. In the undoped and lightly doped $Ca_5In_2Sb_6$, the bipolar term manifests itself as a rise in thermal conductivity at high temperatures. In the most heavily doped samples there is little evidence of a bipolar contribution. Despite the lower speed of sound in $Ca_5In_2Sb_6$ and the reduction in κ_L relative to undoped $Ca_5Al_2Sb_6$, the lattice thermal conductivity of Zn-doped $Ca_5In_2Sb_6$ is comparable to that of Na-doped

$Ca_5Al_2Sb_6$.

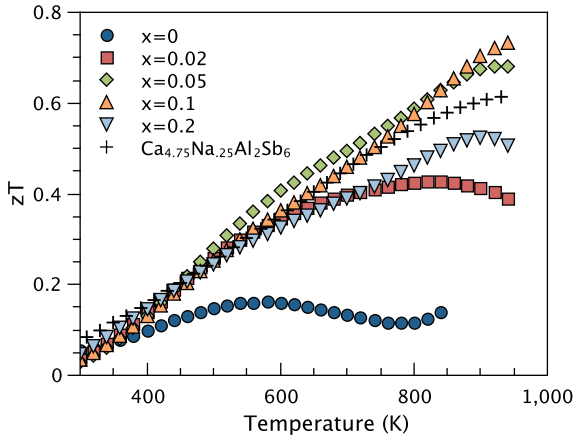

Figure 3.42: The figure of merit of $Ca_5In_{2-x}Zn_xSb_6$ samples is comparable to Na-doped $Ca_5Al_2Sb_6$ within the measured temperature range.

Figure of Merit The figure of merit of $Ca_5In_{2-x}Zn_xSb_6$ is shown as a function of temperature in Figure 3.42, calculated from polynomial fits to the data. Doping with Zn leads to an increase from a maximum of $zT = 0.15$ in the undoped sample to a peak zT of approximately 0.7 in the x=0.05 and x=0.1 samples at 973 K. While the peak zT is also improved somewhat relative to the Al analogue, the difference is within the $\sim$20% measurement uncertainty in zT. To determine the optimal carrier concentrations required for maximum efficiency in $Ca_5In_2Sb_6$, the dependence of the Seebeck coefficient, mobility, and Lorenz number on n were calculated using the SPB model described above. From these, zT was calculated as a function of n at various temperatures, shown as solid curves in Figure 3.43. This predicted optimum carrier concentration of $\sim 2\times10^{20}$ $h^+\text{cm}^{-3}$ at high temperature is in agreement with our experimental results and suggests that further tuning of n is not necessary.

Conclusion Doping $Ca_5In_2Sb_6$ with Zn allows for rational control of the transition from non-degenerate to degenerate semiconducting behavior, providing a route to carrier concentration optimization in this material. Ultimately, a maximum zT of 0.7 was achieved at 950 K in optimally Zn-doped $Ca_5In_2Sb_6$. Although Zn-doped

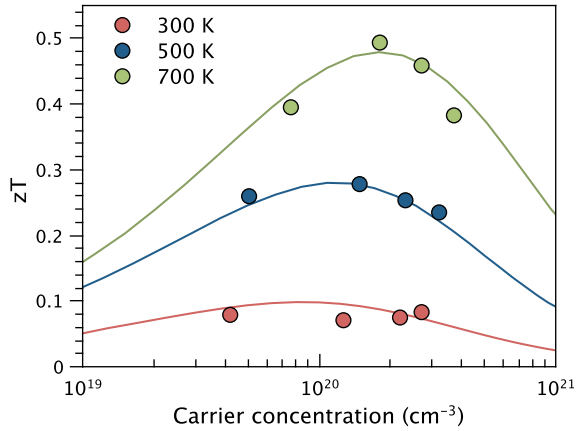

Figure 3.43: The figure of merit at 700 K is optimized at $2{\times}10^{20}$ $h^{+}\mathrm{cm}^{-3}$, in agreement with the SPB model. The parameters used at 300, 500, and 700 K, respectively were $m^{*} = 2.0$, 2.0, 1.8 m_e, $\kappa_L = 1.2$, 0.9, and 0.7 W/mK, and intrinsic mobilities of 7.6, 6.9, and 5.3 cm^2/Vs.

$Ca_5In_2Sb_6$ was expected to have higher mobility and lower lattice thermal conductivity than the Al analogue, the properties of the two systems were comparable within measurement uncertainty, leading to only a moderate improvement in the figure of merit.

Chapter 4

Thermoelectric Properties of $Sr_5Al_2Sb_6$

4.1 Introduction

Among $A_5M_2Sb_6$ Zintl compounds, (A = Ca, Sr, Ba, Eu, Yb, M = Al, Ga, In, and Pn = As, Sb, Bi) most form either the $Ca_5Al_2As_6$ or $Ca_5Al_2Bi_6$ structure type, both of which contain infinite, ladder-like double chains and differ only in the packing arrangement of the "ladders." $Sr_5Al_2Sb_6$ is the only exception, forming instead a completely unique structure type containing winding chains, shown in Figure 4.1. In the original report of the $Sr_5Al_2Sb_6$ structure type [11], Cordier and Stelter argue that the cation size alone cannot account for the formation of this third structure type. Rather, the combination of a large cation (Sr) and a small triel element (Al) may cause the transition from the $Ca_5Al_2As_6$ structure type to the $Sr_5Al_2Sb_6$ structure type.

The structure of $Sr_5Al_2Sb_6$ (space group Pnma) is characterized by infinite anionic chains aligned in the [100] direction. The chains are formed from alternately corner- and edge-sharing $AlSb_4$ tetrahedra, and oscillate back and forth along the c-axis (Figure 4.1b)). $Sr_5Al_2Sb_6$ is orthorhombic, in common with the $Ca_5Al_2As_6$ and $Ca_5Al_2Bi_6$ structure types, but each $Sr_5Al_2Sb_6$ primitive cell contains twice as many formula units (4 formula units, 52 atoms per cell). The valence balance in $Sr_5Al_2Sb_6$ can be understood as follows: each tetrahedrally coordinated Al has a formal valence

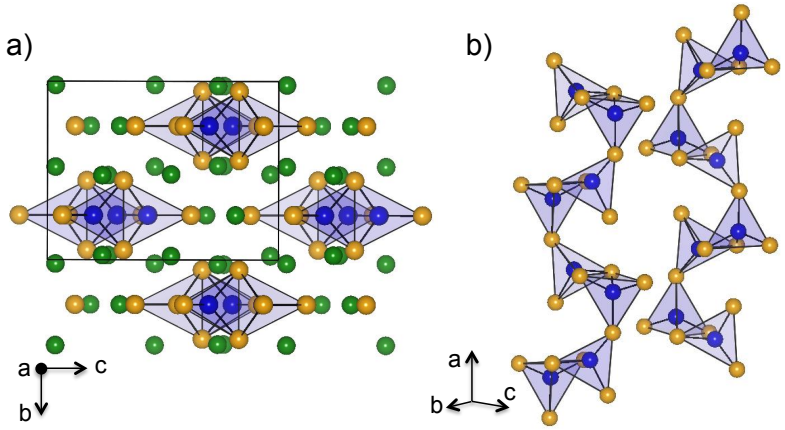

Figure 4.1: (a) The orthorhombic crystal structure of $Sr_5Al_2Sb_6$ (space group $Pnma$) is characterized by infinite anionic chains aligned in [100] direction. (b) Each chain is formed from alternately corner- and edge-sharing $AlSb_4$ tetrahedra [11]. Sr atoms are shown in green, Sb in orange, and Al in blue.

of -1, the two Sb that are singly-bonded to Al have a formal valence of -2, and the "corner sharing" and "edge sharing" Sb (four per formula unit) each have a valence of -1. The anionic unit can thus be written as $[Al_2Sb_6]^{10-}$, while the five Sr^{2+} atoms provide overall charge balance.

We have previously reported excellent thermoelectric properties in other chain-forming Zintl compounds ($Ca_5M_2Sb_6$, Sr_3GaSb_3, Ca_3AlSb_3). These compounds benefits from extremely low lattice thermal conductivity and sufficiently large band gaps for high temperature applications. By optimizing the charge carrier concentration through doping, figures of merit as high as $zT = 0.9$ were obtained. Motivated by the success of these materials, the current study investigates the thermoelectric properties of $Sr_5Al_2Sb_6$ using both high temperature transport measurements and density functional theory.

4.2 Results and Discussion

Electronic Structure Within the Zintl-Klemm concept, the donation of valence electrons from the Sr cations to the polyanions is assumed to be complete in $Sr_5Al_2Sb_6$.

From a band theory approach, the valence band should thus exhibit predominantly anionic character, while the conduction band will be dominated by the unfilled cation states. Consistent with the Zintl-Klemm electron counting concept, Density Functional theory (DFT) shows that $Sr_5Al_2Sb_6$ has a fully filled valence band (Fermi energy in the band gap). As shown in the density of states of Figure 4.2, the valence band edge is made up of primarily Al and Sb electronic states, while the Sr character is most apparent in the conduction band. The conduction band minimum, however, appears to be determined by Al and Sb states. The predicted band gap, E_g, is approximately 0.8 eV. This is comparable to Sr_3GaSb_3 [129] and Sr_3AlSb_3 [65], and significantly larger than that predicted for $Ca_5M_2Sb_6$ (M = Al, Ga, In) [74] or Ca_3AlSb_3 [5].

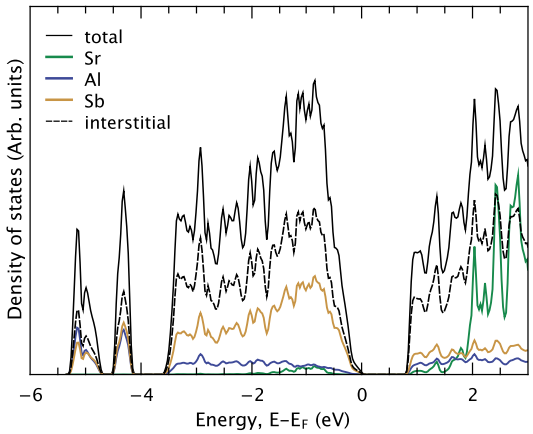

Figure 4.2: The density of states of $Sr_5Al_2Sb_6$ reveals a fully filled valence band and a relatively large band gap of 0.8 eV.

Synthetic Results The $Sr_5Al_2Sb_6$ samples synthesized by directly hot pressing the ball-milled elements were both dense and phase pure. A representative X-ray diffraction pattern is shown in Figure 4.3. Rietveld analysis suggests that the samples are phase pure, containing no visible impurity phases. Since surface oxidation occurred rapidly, care was taken not to expose the samples to air for any period longer than a few minutes.

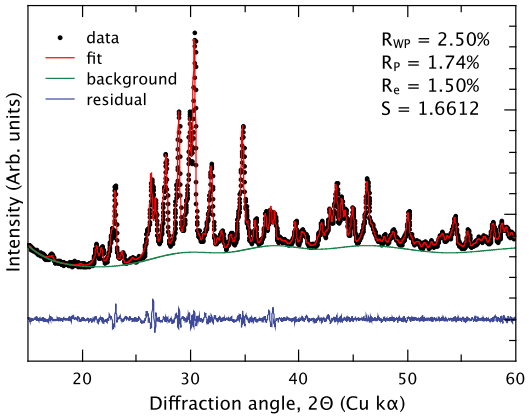

Figure 4.3: Rietveld analysis of the X-ray diffraction data for hot-pressed $Sr_5Al_2Sb_6$ suggests that the samples are phase pure with no significant impurities.

Electronic Transport Consistent with the calculated density of states, $Sr_5Al_2Sb_6$ samples are found to behave as intrinsic semiconductors. The resistivity, ρ, shown in Figure 4.4a, is very high at room temperature and decreases exponentially with increasing temperature. Using the relation $\rho \propto e^{E_g/2k_BT}$ for intrinsic semiconductors, a band gap of $E_g \sim 0.5$ eV can be obtained from the resistivity at high temperature.

The Hall carrier concentration, n_H, and mobility, μ_H, are shown in Figure 4.4b. The carrier concentration is positive, indicating that $Sr_5Al_2Sb_6$ is naturally slightly p-type in common with most Zintl compounds, most likely due to small deviations from the nominal stoichiometry. At room temperature, n_H is extremely low (less than 10^{18} holes/cm^3), and increases with increasing temperature due to the thermal activation of carriers across the band gap. The Hall mobility decreases with increasing temperature, indicating that acoustic phonons are the primary scattering source. The magnitude of the mobility (8 cm^2/Vs at 300 K) is comparable to that of $Ca_5Al_2Sb_6$ and $Ca_5In_2Sb_6$ [74].

The Seebeck coefficients of $Sr_5Al_2Sb_6$ are large and positive, consistent with the low p-type carrier concentration and high resistivity. Above 600 K, the Seebeck coefficients begin to decrease due to minority carrier effects. Estimating the band gap from the peak Seebeck coefficient (E_g=$2\alpha_{max}T_{max}$) yields E_g=0.4 eV, significantly less than the value predicted by DFT calculations. This estimate assumes the same band

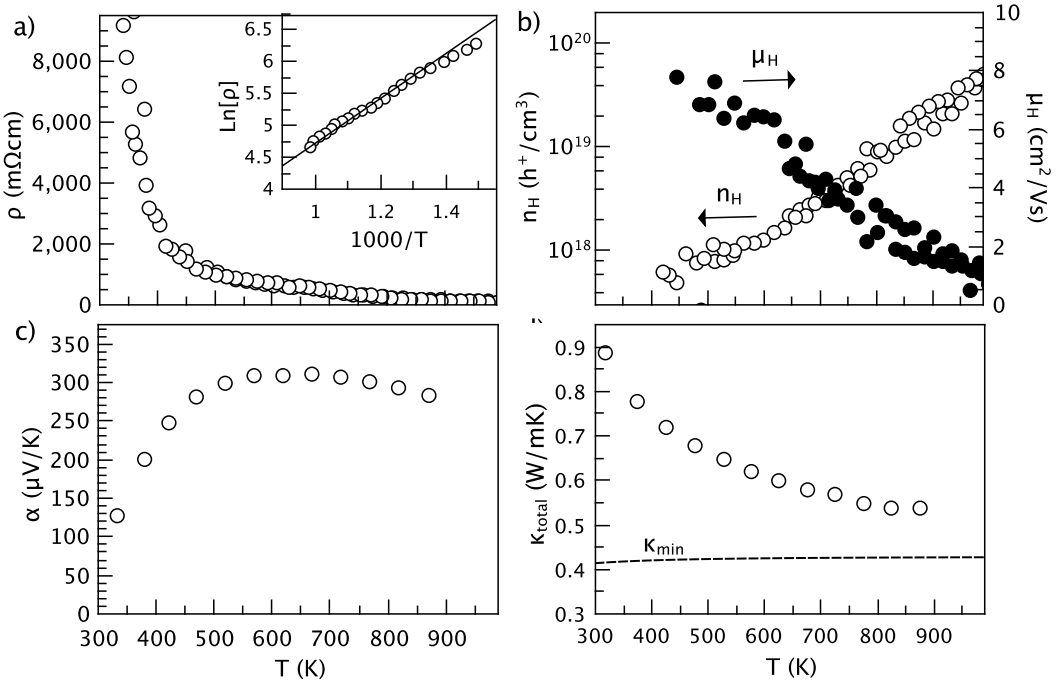

Figure 4.4: (a) The resistivity decreases with temperature, confirming that $Sr_5Al_2Sb_6$ is an intrinsic semiconductor. (b) The carrier concentration increases with temperature due to minority carrier activation, while the mobility decreases due to acoustic phonon scattering. (c) The high, positive Seebeck coefficient is consistent with low, p-type n_H. (d) The thermal conductivity of $Sr_5Al_2Sb_6$ decreases as 1/T due to Umklapp phonon-phonon scattering.

mass in both n- and p-type carriers, and can greatly underestimate E_g if the electrons make a stronger contribution to α.

Thermal Transport The primary attraction of Zintl compounds for thermoelectric applications is the extremely low lattice thermal conductivity (κ_L) that arises from their complex crystal structures [8]. We have previously reported exceptionally low κ_L in a number of compounds related to $Sr_5Al_2Sb_6$, including the $Ca_5M_2Sb_6$ series (Chapter 3), Sr_3AlSb_3 (Chapter 7), Sr_3GaSb_3 (Chapter 6), and Ca_3AlSb_3 (Chapter 5). The κ_L in each of these compounds behaves similarly as a function of temperature, decreasing as 1/T with increasing temperature due to Umklapp scattering, and approaching the predicted minimum κ_L (κ_{min}) at high temperature.

The total thermal conductivity of $Sr_5Al_2Sb_6$ is shown in Figure 4.4d. The elec-

tronic contribution to κ is negligible due to the high electrical resistivity, and κ can thus be considered equivalent to the lattice thermal conductivity at low temperatures. At high temperatures, a bipolar contribution likely increases κ. The minimum lattice thermal conductivity (dashed line in Figure 4.4d) of $Sr_5Al_2Sb_6$ was calculated using the measured longitudinal and transverse speeds of sound, 3720 m/s and 2050 m/s respectively [121].

The temperature dependence of κ_L in $Sr_5Al_2Sb_6$ is very similar to that of other $A_5M_2Sb_6$ and A_3MSb_3 compounds. The magnitude, however, depends on fundamental material parameters, such as the speed of sound (which is determined by density and stiffness) and the unit cell size. The unit cell size and density of $Sr_5Al_2Sb_6$ (52 atoms, 4.49 g/cm^3) are most similar to that of Sr_3AlSb_3 (56 atoms, 4.57 g/cm^3), suggesting that κ_L should be very similar in these two materials, despite their different structure types. Indeed, at high temperature, κ_L is nearly identical, reaching values of 0.54 W/mK and 0.60 W/mK in $Sr_5Al_2Sb_6$ and Sr_3AlSb_3 respectively. However, the room temperature κ_L of $Sr_5Al_2Sb_6$ is lower than that observed in the any other chain-forming Zintl compound discussed here. This may be inherent to the material, or it may be due to microstructural differences, which particularly influence low temperature κ_L.

4.3 Conclusion

$Sr_5Al_2Sb_6$ is a valence-precise Zintl phase that exhibits promising thermoelectric properties that are comparable with previously investigated $A_5M_2Sb_6$ and A_3MSb_3 compounds. Density Functional theory (DFT) shows that $Sr_5Al_2Sb_6$ has a fully filled valence band dominated by Sb and Al electronic states, consistent with the Zintl-Klemm electron counting concept and a band gap of 0.8 eV. The resistivity, Hall, and Seebeck coefficient measurements reveal intrinsic semiconducting behavior and a small p-type type carrier concentration. The magnitude of the electronic mobility and Seebeck coefficients are comparable to that of undoped $Ca_5Al_2Sb_6$. Due to its large, complex unit cell and low speed of sound, $Sr_5Al_2Sb_6$ has exceptionally low lattice

thermal conductivity. The intrinsic thermal and electronic properties of $Sr_5Al_2Sb_6$ suggest that high zT values can potentially be obtained in optimally doped $Sr_5Al_2Sb_6$.

Chapter 5

Thermoelectric Properties of Ca_3AlSb_3

5.1 Introduction

Ca_3AlSb_3 crystallizes in the Ca_3InP_3 structure type (space group $Pnma$), which is characterized by simple linear chains of corner-sharing $AlSb_4$ tetrahedra that extend infinitely in the [010] direction (Figure 5.1) [12]. Compared with $Ca_5Al_2Sb_6$, the extra Ca cation, and thus additional electrons in Ca_3AlSb_3, means that covalent Sb-Sb bonds between adjacent chains are not required to satisfy valence. Although Ca_3AlSb_3 is the only antimonide with the Ca_3InP_3 structure type, a number of arsenides and phosphides crystallize with the same structure, including A_3InP_3 (A = Ca, Sr, Eu) [158, 122, 159], Ca_3MAs_3 (M = Al, Ga) [160, 158], and Ba_3InAs_3 [161].

Within the Zintl formalism, Ca_3AlSb_3 can be expressed as $Ca_3^{+2}Al_1^{-1}Sb_2^{-2}Sb_1^{-1}$, treating Al as part of the covalent anionic substructure. The aluminum atoms are bound to four antimony atoms, and therefore have a formal valence of -1. Within the chains of $AlSb_4$ tetrahedra, the antimony atoms that are shared between two tetrahedra have two bonds and can be considered to have a valence state of -1. The remaining antimony have only one bond, corresponding to an valence state of -2. Situated between the chains are Ca^{+2} ions, which provide overall charge balance. The formal valence states given here are a convenient construct. However, the actual extent of charge transfer is determined by electronegativity and the degree of ionic

or covalent bonding. Treating Al as a cation yields the same conclusion; namely, Ca_3AlSb_3 is charge balanced.

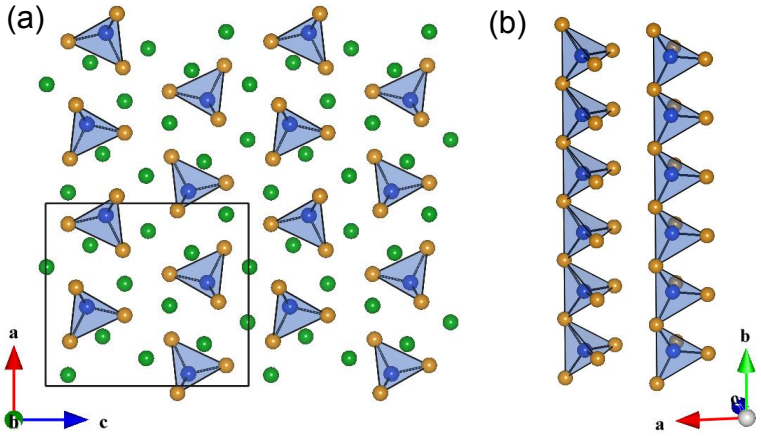

Figure 5.1: (a) The orthorhombic structure of Ca_3AlSb_3 (Space group Pnma) viewed in the [010] direction. (b) Infinite chains of corner-sharing $AlSb_4$ tetrahedra extend in the [010] direction. Sb atoms are orange, Ca are green, and Al are blue.

5.2 Na-doped Ca_3AlSb_3

Introduction Inspired by our previous investigation of the thermoelectric properties of sodium-doped $Ca_5Al_2Sb_6$ [10], this work focuses on the high temperature thermal and electronic properties of $Ca_{3-x}Na_xAlSb_3$ (x = 0, 0.03, 0.06, and 0.15). In addition to transport measurements, this study employs a combination of classic transport theory and electronic structure calculations to improve our understanding of the relationship between chemical bonding and transport in Ca_3AlSb_3. Beyond Ca_3AlSb_3 and $Ca_5Al_2Sb_6$, a variety of structure types with distinct tetrahedra moieties exist within the A_3MPn_3 and $A_5M_2Pn_6$ compounds, offering further opportunities for developing structure-property relationships in Zintl compounds [35, 162, 163].

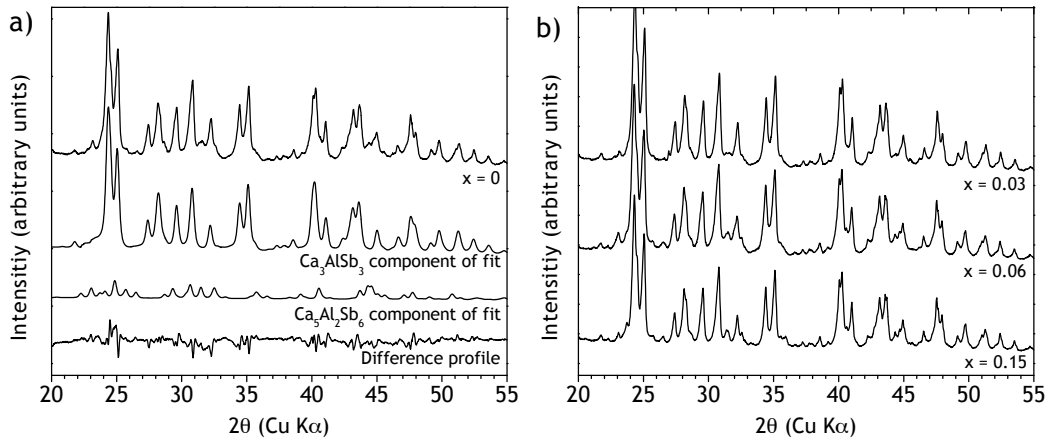

Figure 5.2: (a) XRD pattern of $x = 0$ sample and Rietveld fit using known crystal structures of Ca_3AlSb_3 and $Ca_5Al_2Sb_6$ [12, 13]. (b) Similar amounts of $Ca_5Al_2Sb_6$ impurity phase are observed in all sodium-doped samples

Results and Discussion Ball milling of elemental reagents followed by hot pressing resulted in samples with densities in excess of 95%. X-ray diffraction (XRD) patterns of each polycrystalline sample ($x = 0$, 0.03, 0.06, 0.15) are shown in Figure 5.2. As the ionic radii of Na^{+1} and Ca^{+2} are nearly identical, no change in lattice parameter is expected from doping. XRD patterns were subject to Rietveld refinement using the known structures of Ca_3AlSb_3 and $Ca_5Al_2Sb_6$. Figure 5.2a shows the Ca_3AlSb_3 and $Ca_5Al_2Sb_6$ components of the Rietveld fit for the $x = 0$ sample, as well as a difference profile.

All compositions were found to contain approximately 10 wt.% of the closely related $Ca_5Al_2Sb_6$ phase, possibly due to inadvertent Ca deficiency. Cordier et al. also reported $Ca_5Al_2Sb_6$ as a secondary phase in their efforts to synthesize pure Ca_3AlSb_3 [12].

SEM images of polished and fracture surfaces of the $x = 0.06$ sample are shown in Figure 5.3. Scanning electron microscopy confirms the high density of the samples and reveals grains with diameters of approximately 1 μm. The small grain size may be due to the presence of $Ca_5Al_2Sb_6$ impurity phase pinning grain boundaries during growth, or due to the relatively low hot-pressing temperature (973 K).

Microprobe analysis with wavelength dispersive spectroscopy (WDS) was used

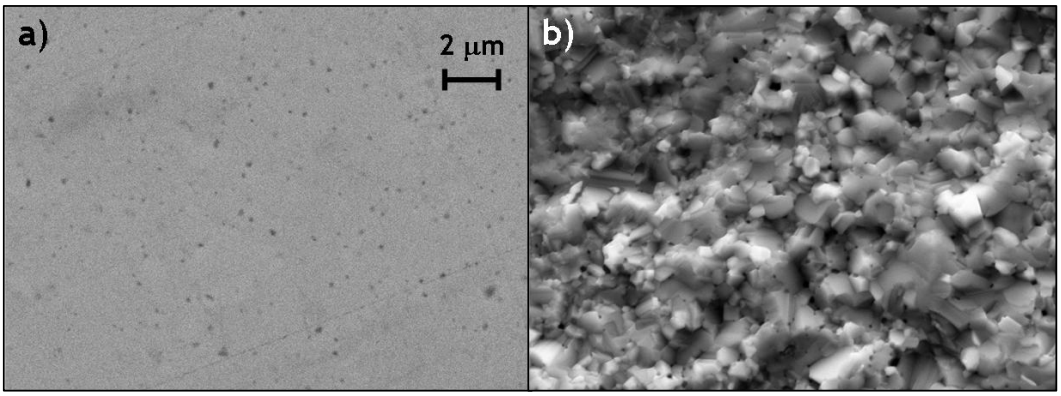

Figure 5.3: Scanning electron micrographs of a) polished and b) fractured surfaces of the $x = 0.06$ sample reveal high density material and approximately 1 μm diameter grains. Black dots in (a) are voids revealed by polishing.

to verify stoichiometry and to quantify the incorporation of sodium in Ca_3AlSb_3. Microprobe analysis also confirmed the presence of the $Ca_5Al_2Sb_6$ impurity phase in all samples. This phase appears as approximately 1 μm grains, evenly distributed within the Ca_3AlSb_3 majority phase. In the $x = 0.15$ sample, a sodium-rich impurity phase was also identified, suggesting that this sample exceeded the solubility limit of sodium in Ca_3AlSb_3. Figure 5.4 shows the sodium concentration obtained from WDS versus the synthetic sodium content. The unfilled symbols represent the average sodium concentration of each sample (including the sodium-rich phase in the $x = 0.15$ sample), obtained using a spot size of 30 μm averaged over 25 points on each sample. The deviation of the average sample sodium content from the expected composition is attributed to sodium loss during synthesis. The filled symbols show the sodium content of the matrix, which consists of the Ca_3AlSb_3 and $Ca_5Al_2Sb_6$ phases. The large discrepancy between the average and matrix sodium concentration for the x=0.15 sample is due to the formation of the sodium rich impurity phase which makes up an estimated 5 to 10 volume % of the sample.

Electronic Transport Properties The electronic and thermal properties of sodium-doped $Ca_5Al_2Sb_6$ have been previously investigated, [10] and are similar to those reported here for sodium-doped Ca_3AlSb_3. In light of this, and as the volume fraction

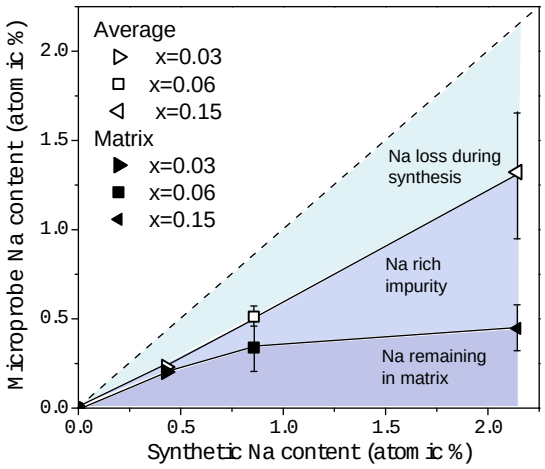

Figure 5.4: Microprobe analysis suggests that some sodium loss occurs during synthesis, and that the solubility limit of sodium in $Ca_{3-x}Na_xAlSb_3$ is exceeded for $x > 0.06$ (0.8 atomic %). Filled symbols indicate Na content of the matrix phases (Ca_3AlSb_3 and $Ca_5Al_2Sb_6$), while unfilled symbols represent total Na concentration, including the Na-rich impurity phase.

of the Ca_3AlSb_3 phase is far greater than that of the $Ca_5Al_2Sb_6$ minority phase, the properties reported here should be close to those expected from phase pure Ca_3AlSb_3.

From the Zintl valence-counting formalism, nominally undoped Ca_3AlSb_3 is expected to be an intrinsic semiconductor. In practice, extrinsic defects lead to a measured Hall carrier concentration ($n_H = 1/R_He$, where R_H is the Hall coefficient) of 10^{18} h^+/cm^3 at room temperature. The room temperature n_H versus microprobe sodium content is shown in Figure 5.5. The carrier concentration expected from simple charge counting, assuming that each sodium atom contributes one free hole, is shown as a dashed line. Comparing the measured carrier concentrations to those predicted from charge counting, one finds that the experimental n_H is significantly less than predicted. This is analogous to the low doping effectiveness observed in sodium-doped $Ca_5Al_2Sb_6$ [10].

Figure 5.6a) illustrates the temperature dependence of n_H. Nominally undoped Ca_3AlSb_3 exhibits increasing carrier concentration due to carrier activation beginning at 500 K. For the sodium-doped samples, n_H remains constant with temperature to approximately 800 K, indicative of extrinsic doping. The abrupt increase in carrier

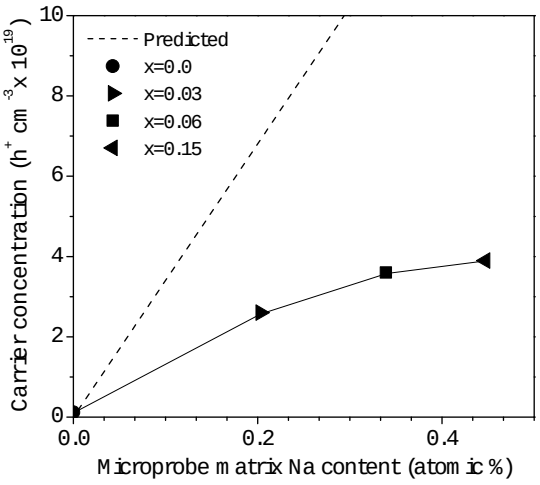

Figure 5.5: Hall carrier concentration (300 K) increases as a function of sodium content, although doping effectiveness is less than predicted by charge counting.

concentration beyond 800 K may be due to activation of minority carriers across the band gap, an increase in majority carrier concentration due to dopant solubility variation, or a phase change.

The Hall mobility as a function of temperature, calculated from measured R_H and resistivity (ρ), is shown in Figure 5.6c). Matthiessen's rule approximates electronic mobility as the reciprocal sum of multiple mobility terms, each having an independent scattering mechanism ($\frac{1}{\mu} = \sum_i \frac{1}{\mu_i}$). Generally, one scattering mechanism limits the total mobility at extreme temperature ranges. In Ca_3AlSb_3, the mobility increases with temperature up to 600 K, possibly due to activation barriers such as oxide layers at the grain boundaries. Such an activated mobility would exhibit an exponential temperature dependence ($\mu = \mu_o e^{E_A/k_B T}$). At high temperatures, mobility is generally limited by acoustic phonon scattering, for which the temperature dependence is given by the power law, $\mu_H \propto T^{-\nu}$, where ν is 1.5 for nondegenerate semiconductors and 1 for degenerate semiconductors [76]. A power law fit to the high temperature mobility data shown in Figure 5.6c) results in an exponent larger than 1.5. This may be related to the abrupt increase in carrier concentration above 800 K observed in Figure 5.6, or a temperature dependent effective mass.

The temperature dependence of the resistivity (Figure 5.6c)) follows from the car-

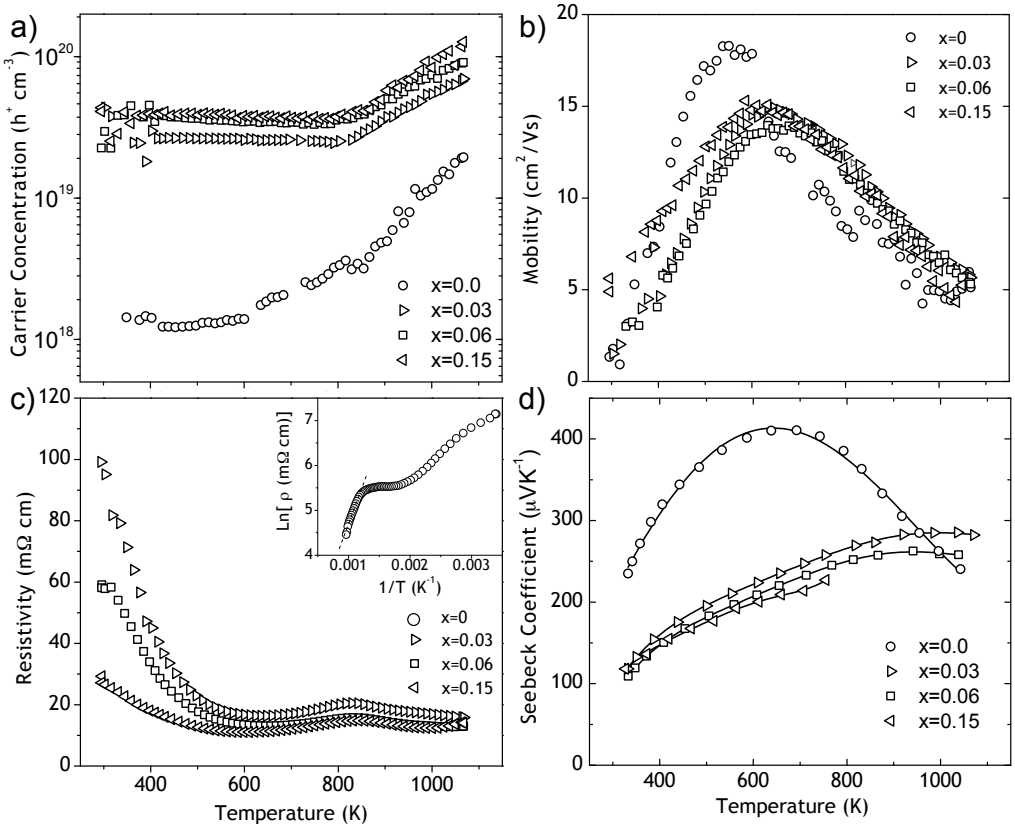

Figure 5.6: (a) Hall carrier concentration of $Ca_{3-x}Na_xAlSb_3$ as a function of temperature. (b) Temperature dependence of the Hall mobility suggests an activated mobility at low temperature, and a mobility limited by phonon scattering at high temperature. (c) The resistivity as a function of temperature for $x = 0.03$, 0.06, 0.15. Inset: Ln[ρ] versus 1/T for $x = 0$ sample. The high temperature linear fit results in a band gap of 0.6 eV. (d) The high temperature Seebeck coefficients show degenerate behavior for the extrinsically doped, p-type compositions.

rier concentration and mobility ($\rho = 1/ne\mu$). At high temperature, the resistivity of the nominally undoped sample exhibits an exponential decrease due to carrier activation across a band gap (Figure 5.6c), inset). A band gap of ∼0.6 eV was estimated from the slope of the resistivity in this presumably intrinsic high temperature regime ($\rho \propto e^{E_g/2k_BT}$). This is similar to the band gap observed in both $Yb_{14}AlSb_{11}$ (0.5 eV) and in $Ca_5Al_2Sb_6$ (0.5 eV). Doping Ca_3AlSb_3 with sodium results in reduced resistivity due to increased carrier concentration. For the undoped and doped compositions, the negative slope of the resistivity at low temperatures is due to the increasing mobility in that temperature range. From 600-800 K, the resistivities of the sodium-doped

samples begin to increase with temperature, as is expected for a degenerate semiconductor with mobility limited by phonon scattering. However, above 800 K, this trend is reversed, and the resistivity begins to decrease again due to the carrier activation discussed above.

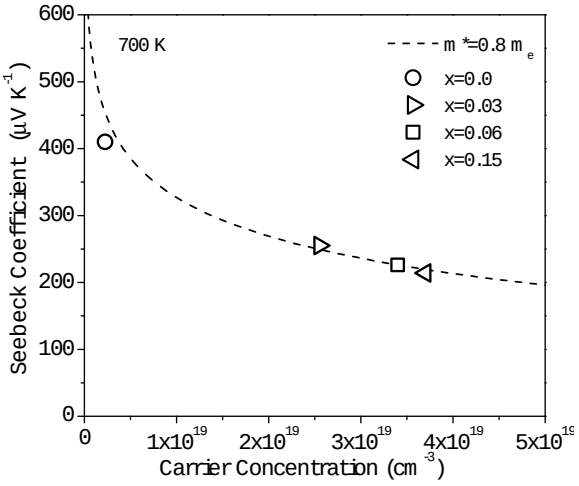

Figure 5.7: Experimental Seebeck coefficients of $Ca_{3-x}Na_xAlSb_3$ as a function of carrier concentration. The dotted line was generated using a single parabolic band approximation and an effective mass of 0.8 m_e.

Figure 5.7 illustrates the effect of doping on the Seebeck coefficients measured at 700 K. The Seebeck coefficients are large and positive, consistent with the relatively low carrier concentrations revealed by Hall effect measurements. As expected, increasing carrier concentration leads to a decrease in the Seebeck coefficient. Solutions to the Boltzmann transport equation within the relaxation time approximation have been used to model the relationship between carrier concentration and the Seebeck coefficient via the reduced chemical potential, η [6, 164]. Here, we assume a single carrier type is dominant, allowing use of a single parabolic band (SPB) model, and we assume acoustic phonon scattering.

We employ this model at 700 K because in this temperature regime acoustic phonon scattering becomes the dominant scattering mechanism, and extrinsic carriers still dominate electronic transport. An effective mass of 0.8 m_e was calculated for this temperature using the measured α and n_H from the $x = 0.06$ sample. The resulting

Pisarenko relationship is shown as the dashed curve in Figure 5.7. All of the samples fall on or near this curve, suggesting that the effective mass remains fairly constant within this carrier concentration range.

The trends in Seebeck coefficient as a function of temperature are shown in Figure 5.6d. The Seebeck coefficient of the nominally undoped sample peaks at 650 K, at which point thermally activated electrons cause a reduction in thermoelectric voltage, and a decaying Seebeck coefficient results. Samples with $x = 0.03$ - 0.15 exhibit increasing Seebeck coefficients to high temperature, as expected for extrinsic semiconductors. At 1000 K, the $x = 0.06$ sample appears to peak at 260 μV/K. From this, a band gap of 0.5 eV is estimated using $E_g = 2e\alpha_{max}T_{max}$ [154].

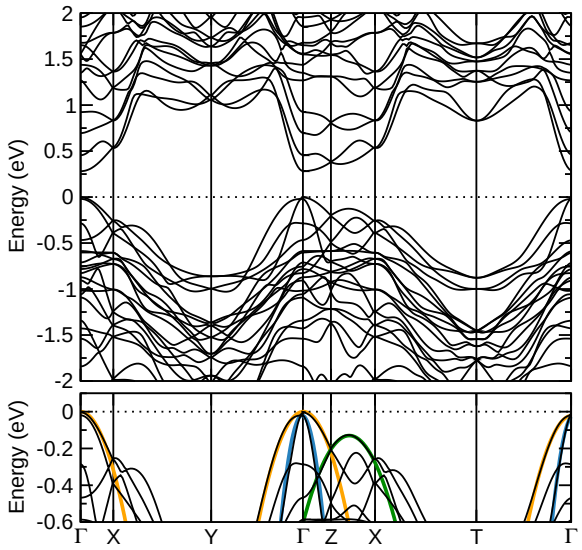

Figure 5.8: Top panel: Calculated band structure of Ca_3AlSb_3. Bottom panel: Magnified band structure at the top of the valence band. The highest carrier concentration obtained experimentally corresponds to ∼0.1 eV below the valence band edge. The blue, yellow, and green dashed curves are parabolas with effective masses of 0.15, 0.75, and 0.9 m_e.

Electronic Structure Calculations Density functional theory calculations (DFT) are used here to gain a better understanding of electronic behavior in this compound and to guide chemical strategies for further optimization. The band structure of Ca_3AlSb_3 is shown in the top panel of Figure 5.8, while the bottom panel displays

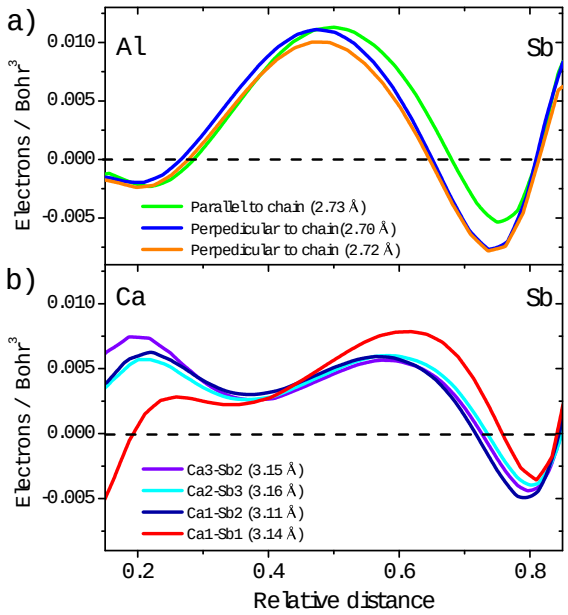

Figure 5.9: (a) EDD line-scans show charge accumulation and depletion along a chain-forming Al-Sb bond (green), and two distinct Al-Sb bonds perpendicular to the chains (blue and orange). (b) Representative Ca-Sb bonds (site designations correspond to ref. [12].

only the top of the valence band. Centered at the Γ point, the valence band edge contains two asymmetric, overlapping bands which give the appearance of nested, parabolic light and heavy bands, as well as an offset band with a maximum at -0.13 eV. Parabolic fits are used to estimate the band masses of the effective light and heavy bands, as well as the offset band. The blue, yellow, and green solid curves in the bottom panel of Figure 5.8 are parabolas with effective masses of 0.15, 0.75, and 0.9 m_e, respectively. The most heavily doped sample in this study has a carrier concentration of 4×10^{19} h^+/cm^3, corresponding to a Fermi level of approximately $\sim$0.1 eV below the valence band edge. This suggests that the doped samples in this study have energies spanning the three highlighted bands at the top of the valence band. The electronic transport data reported here is reasonably well-described by a single parabolic band model (Figure 5.7). However, from Figure 5.8, one might expect to observe a carrier concentration dependent effective mass. In particular, by doping to higher carrier concentrations ($>5\times10^{19}$ h^+/cm^3) to probe deeper into the

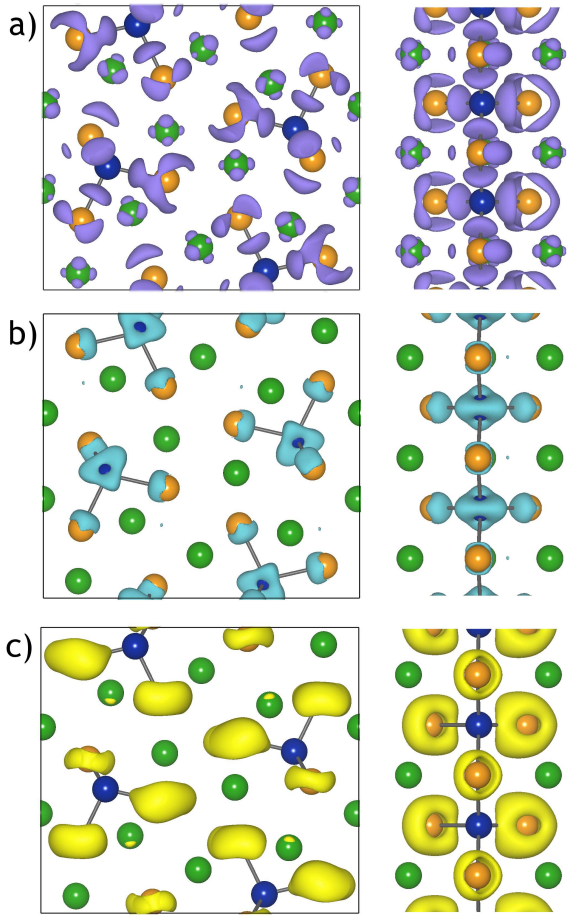

Figure 5.10: EDD isosurfaces show (a) accumulation and (b) depletion regions. (c) Electron density map of valence band edge (-0.1 eV). Images are projections along [010] (left side) and [201] (right side) directions.

valence band, a larger effective mass and non-SPB behavior may result, due to the ever-increasing influence of the offset band (highlighted by the green curve in Figure 5.8). This would be similar to the offset band behavior observed in La_3Te_4 [23].

The Ca_3InP_3 structure type accommodates a considerable number of substitutions: Ca can be replaced by Sr, Ba, and Eu; In by Al and Ga; and P by As and Sb. Considering both isoelectronic substitutions and potential dopants, there are numerous routes to influencing the transport properties of this compound. To understand the potential effects of these substitutions, investigation of the bonding character in Ca_3AlSb_3 is essential.

The traditional quantum mechanical description of covalent bonding is character-

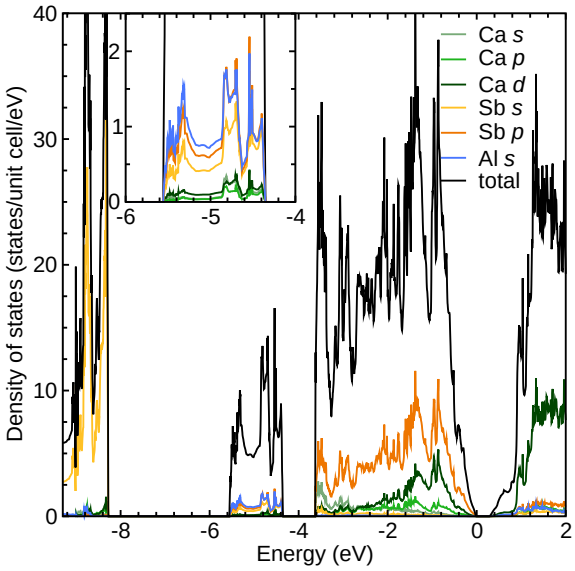

Figure 5.11: Density of states of Ca_3AlSb_3 reveals a band gap at the Fermi level with a valence band edge dominated by Sb p states. The inset highlights interacting Al-Sb bonding states.

ized by charge build-up between atoms. Thus, an intuitive approach to locating covalent bonds is to determine the location of increased electron density. This approach is pursued here through post-processing of DFT calculations, which aids in the visualization of electron density reorganization. Electron density difference (EDD) maps have been generated by subtracting the super-positioned, non-interacting, atomic electron densities (procrystal) from the calculated electron density of Ca_3AlSb_3 [140]. EDD line-scans, shown in Figure 5.9, illustrate the charge accumulation and depletion along both Al-Sb and Ca-Sb bonds. Part Figure 5.9a shows an Al-Sb bond forming the backbone of a tetrahedral chain (green curve) and two distinct Al-Sb bonds perpendicular to the chain (blue and orange curves). Symmetric accumulation of electron density between the atoms indicates that the Al-Sb bonds have covalent character, consistent with our understanding of bonding within the Zintl construct. This electron accumulation shows surprising symmetry, considering the large disparity in electronegativity of Al and Sb. In contrast, representative Ca-Sb line scans, shown in Figure 5.9b, exhibit significant asymmetry in charge distribution, with the principle charge build-up nearer to the Sb side. EDD line scans of $SrZn_2Sb_2$ have shown similar features

[75]. To further illustrate the bonding environment in Ca_3AlSb_3, EDD isosurfaces in Figure 5.10 depict (a) charge accumulation and (b) depletion. Charge build-up at the mid-point between the Al and Sb atoms, indicative of covalent bonding, is readily observed.

As discussed above in reference to Figure 5.8, the effective mass at the band edge is fundamental to electron transport. To engineer transport properties in this material, it is therefore important to have some understanding of the character of the valence band edge. Density of states calculations (DOS) (Figure 5.11) indicate that Sb p states are a major component of the valence band edge, analogous to the calculated density of states for the AZn_2Sb_2 Zintl antimonides [75]. The isosurfaces in Figure 5.10c illustrate the electron charge density at a specific energy near the valence band edge (-0.1 eV). The electron charge density is highest around the Sb sites, where oriented donut-like isosurfaces form, suggesting that hole transport, and therefore hole mobility, is centered around the tetrahedral Sb, as has been found in the structurally related $A_{14}MPn_{11}$ [63]. It is interesting to note that the light bands shown in the DOS span the Γ-Y, Γ-Z, and Γ-T directions, corresponding to the y-z plane containing the donut-like charge density isosurfaces.

Thermal Transport Properties The total thermal conductivity, shown in Figure 5.12a, is a combination of lattice, electronic, and bipolar contributions ($\kappa_{total} = \kappa_L + \kappa_e + \kappa_B$). The Wiedemann-Franz relation ($\kappa_e = \frac{LT}{\rho}$) is used to estimate the electronic contribution to the thermal conductivity. Temperature dependent Lorenz numbers (L) were calculated within a single parabolic band approximation. The reduced chemical potential, η, was calculated from experimental Seebeck coefficients.

In both doped and undoped Ca_3AlSb_3, κ_e is small (< 0.08 W/mK) due to the relatively high electrical resistivity and small Lorenz values (inset, Figure 5.12b). Subtracting κ_e from κ_{total} leaves the lattice and bipolar contributions (Figure 5.12b). There appears to be a significant bipolar contribution at temperatures above 900 K in the undoped material, while κ_L is the dominant contribution in the doped samples. The temperature dependence of κ_L is well-described by the $1/T$ relationship expected

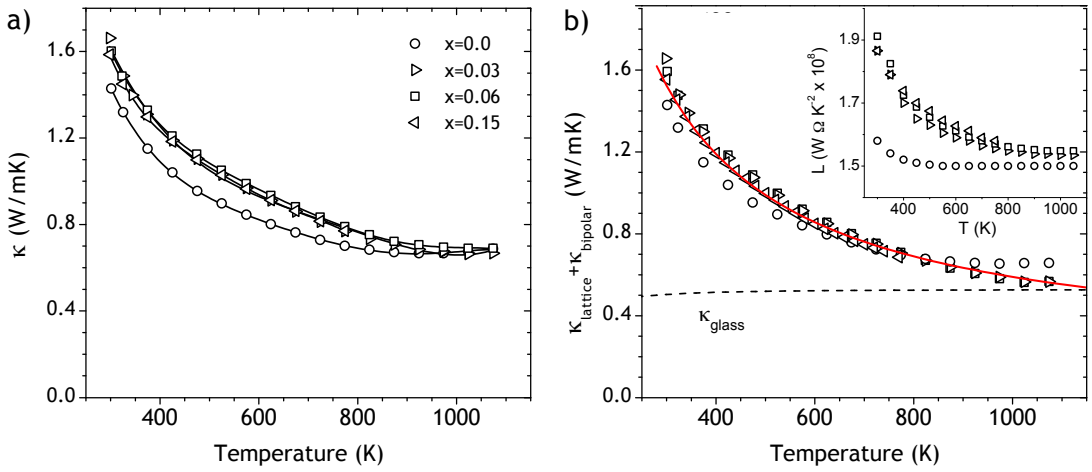

Figure 5.12: (a) Total thermal conductivity of $Ca_{3-x}Na_xAlSb_3$ (x= 0, 0.03, 0.06, 0.15). (b) κ_L exhibits 1/T temperature dependence (dashed red curve). At high temperatures, $\kappa_L + \kappa_B$ approaches the glassy limit (dashed black curve). The inset illustrates the temperature dependence of the Lorenz numbers in units of 10^8 WΩK^{-2}.

for Umklapp scattering (solid red curve). Doping with sodium does not result in a significant change in lattice thermal conductivity, as might be expected for low dopant concentrations and small mass contrast.

Room temperature ultrasonic measurements of undoped Ca_3AlSb_3 yield longitudinal and transverse speeds of sound of 4170 m/s and 2440 m/s, respectively. From these, a mean speed of sound of 2710 m/s and an effective Debye temperature of 261 K are calculated using Eq. 5.1 and Eq. 5.2.

$$\nu_m^3 = \frac{3}{\nu_l^{-3} + 2\nu_t^{-3}} \tag{5.1}$$

$$\theta_D = \frac{\nu_m \hbar}{k_B}\left(\frac{6\pi^2}{V}\right)^{1/3} \tag{5.2}$$

An estimate of the lower bound for the lattice thermal conductivity can be made using Eq. 5.3, where the sum is over three vibrational modes (one longitudinal and two transverse) and where $\theta_i = \nu_i(\hbar/k_B)(6\pi^2/V)^{1/3}$. Because this model assumes a minimum scattering length as a function of phonon frequency, this is termed the

glassy limit of the thermal conductivity [80].

$$\kappa_{min} = \left(\frac{\pi}{6}\right)^{1/3} \frac{k_B}{V^{2/3}} \sum_i \nu_i \left(\frac{T}{\theta_i}\right)^2 \int_0^{\theta_i/T} \frac{x^3 e^x}{(e^x - 1)^2} dx \tag{5.3}$$

At high temperature, κ_L approaches the predicted glassy limit. This low lattice thermal conductivity is most likely a result of the complex crystal structure and large unit cell size of Ca_3AlSb_3. [7, 101]. In addition to structural complexity, defect scattering may also have a significant influence on κ_L in this compound.

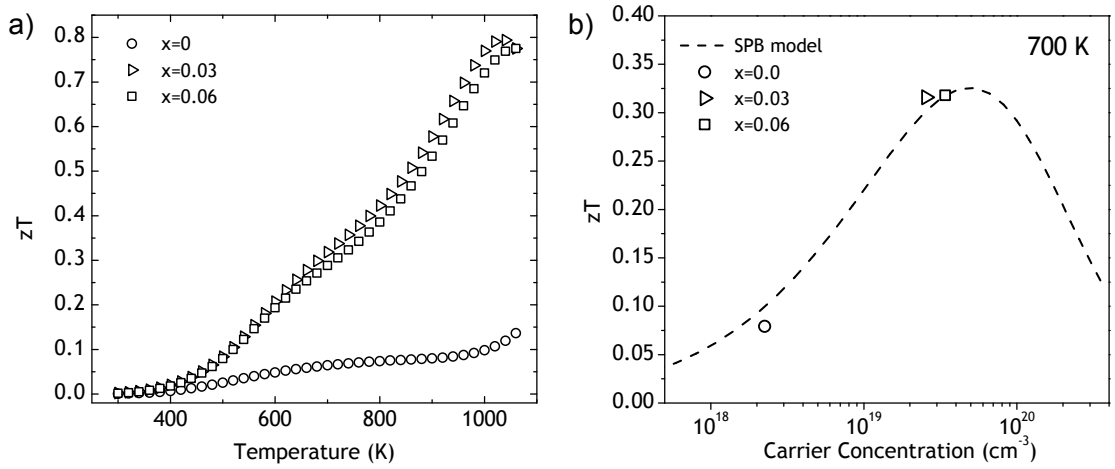

Figure 5.13: (a) High temperature figure of merit of $Ca_{3-x}Na_xAlSb_3$ yields a maximum value of 0.8 at 1050 K. (b) Experimental zT versus carrier concentration for $Ca_{3-x}Na_xAlSb_3$. The dashed line was generated using a single parabolic band model, with an effective mass of 0.8 m_e, and intrinsic mobility 15 cm^2/Vs and lattice thermal conductivity of 0.78 W/mK.

Figure of Merit The figures of merit of the $x = 0$ - 0.06 compositions, calculated from the high temperature results presented above, are shown in Figure 5.13a. The $x = 0.15$ data is not included here, due to the significant presence of the sodium-rich impurity phase. A maximum zT value of 0.8 is obtained at 1050 K for the samples with $x = 0.03$ and $x = 0.06$. In Figure 5.13b, the experimental zT versus carrier concentration is compared to a single parabolic band model (dashed line). We have again focused on transport at 700 K to avoid error associated with activated carriers at higher temperatures, and to clearly be in a regime where transport is limited by

phonon scattering. The $x = 0.06$ sample was used to obtain the parameters for this model: an effective mass of 0.8 m_e, a constant lattice thermal conductivity of 0.78 W/mK, and an intrinsic mobility, $\mu_o = 15$ cm^2/Vs.

The maximum carrier concentration obtained experimentally, 4×10^{19} holes/cm^3, is close to the optimum carrier concentration of 5×10^{19} holes/cm^3 predicted by the model at 700 K. However, the maximum zT of this material occurs at higher temperatures, at which point lightly doped material is susceptible to reduction in thermoelectric voltage due to minority carrier activation. A single parabolic band model does not take carrier activation into account, and therefore, while accurate at 700 K, it likely underestimates the optimum carrier concentration for a maximum zT at higher temperatures. This, in addition to the likelihood of a heavy band located near -0.13 eV, suggests that higher carrier concentrations will result in higher zT values than reported here.

Conclusion The exploration of complex Zintl compounds ($Yb_{14}MnSb_{11}$, $CaZn_2Sb_2$, $Ba_8Ga_{16}Ge_{30}$, $CsBi_4Te_6$, $Ca_5Al_2Sb_6$) [21, 4, 42, 10, 32, 165, 6] continues to reveal good thermoelectric materials, with properties that can be readily rationalized through simple chemical principles. Here we have described a new thermoelectric material, Ca_3AlSb_3, a *p*-type semiconductor composed of Earth-abundant, non-toxic elements. Electronic structure calculations suggest that the valence band edge is effectively two nested parabolic bands, which are dominated by Sb p states. Carrier concentration control has been achieved by substituting Ca^{2+} with Na^{1+}. High temperature transport properties can be modeled with parabolic bands and acoustic phonon scattering of charge carriers to guide further optimization of the material. The lattice thermal conductivity is found to approach the glassy minimum at high temperature (0.6 W/mK at 1050 K), behavior attributed to a complex unit cell. The combination of low lattice thermal conductivity, and a sufficiently large band gap to maintain degenerate behavior at high temperature, leads to a zT of 0.8 at 1050 K, with higher zT likely at higher carrier concentrations.

5.3 Zn-doped Ca_3AlSb_3

Introduction In the family of Zintl antimonides, Ca_3AlSb_3 is a promising compound, with a peak zT of 0.8 obtained at 1050 K upon doping with Na^+ for Ca^{2+}.[5] Our initial investigation of Ca_3AlSb_3 showed an intrinsic semiconductor with a band gap of 0.6 eV and very low lattice thermal conductivity (0.6 W/mK at 870 K) due to a relatively complex crystal structure. While doping with sodium leads to the formation of holes and degenerate transport behavior, a solubility limit leads to a maximum of $4x10^{19}$ holes/cm^3, whereas the optimum carrier density for a maximum zT is expected to be greater than $5x10^{19}$ holes/cm^3.[5]

Inspired by our previous investigation of Ca_3AlSb_3 and the doping studies with sodium and zinc in $Ca_5Al_2Sb_6$,[5, 10, 125], here we explore the influence of the substitution of Al^{3+} with Zn^{2+} on the thermoelectric transport properties of the $Ca_3Al_{1-x}Zn_x$-Sb_3 system, and compare the effects of Na and Zn doping. Furthermore, we report on the influence of the grain size in these materials on the thermoelectric transport.

Results and Discussion Following ball milling and hot pressing, $Ca_3Al_{1-x}Zn_xSb_3$ samples with $x = 0.00$, 0.01, 0.02, and 0.05 have geometric densities of at least 97% of the theoretical densities. As reported in Ref. [5], X-ray diffraction (XRD) and scanning electron microscopy (SEM) reveal secondary phases of $Ca_5Al_2Sb_6$ and $Ca_{14}AlSb_{11}$ with 5-10 wt% and 2-5 wt%, respectively. The XRD patterns and Pawley refinements (using all three phases) are shown in Figure 5.14. SEM analysis of fracture surfaces reveals small grains (< 1 μm in diameter) and porosity ($\sim 1\mu$m in diameter) at the grain boundaries. Anomolously, the sample with the nominal composition of $Ca_3Al_{0.99}Zn_{0.01}Sb_3$ contains grains that are at least an order of magnitude larger than the other samples, as shown in the inset of Figure 5.16. The relatively small grains found in all samples in this study are in accordance with the broad profiles of the

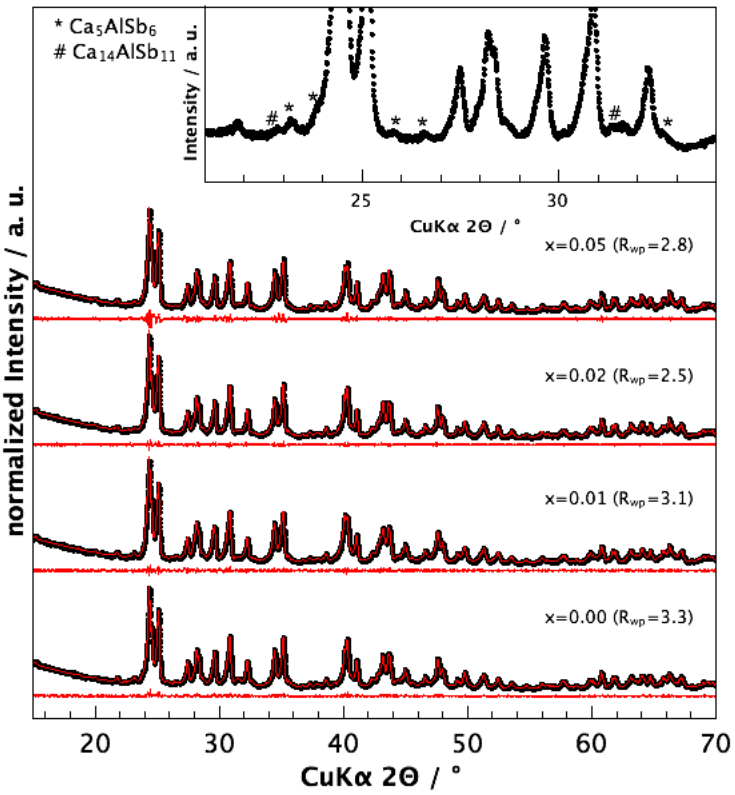

Figure 5.14: X-ray diffraction data for $Ca_3Al_{1-x}Zn_xSb_3$ including profile fit, profile difference, and profile residuals from the corresponding Pawley refinement including the secondary phases of $Ca_5Al_2Sb_6$ and $Ca_{14}AlSb_{11}$. The inset shows the reflections indexed to the impurity phases.

reflections in Figure 5.14, and therefore no significant change of the lattice parameters upon substitution with Zn can be observed.

Electronic Transport Properties The electronic properties of sodium-doped Ca_3AlSb_3 have previously been investigated and are largely similar to those reported here with zinc as a dopant. In the following results we have included the transport properties of the Na-doped sample that resulted in the highest figure of merit (nominal composition $Ca_{2.94}Na_{0.06}AlSb_3$) as a basis for comparison.[5]

Figure 5.15 shows the measured Hall carrier concentrations as a function of temperature. Though Ca_3AlSb_3 is a classic, valence-precise Zintl compound, the undoped material has a p-type carrier concentration of 10^{18} holes/cm^3 at room temperature

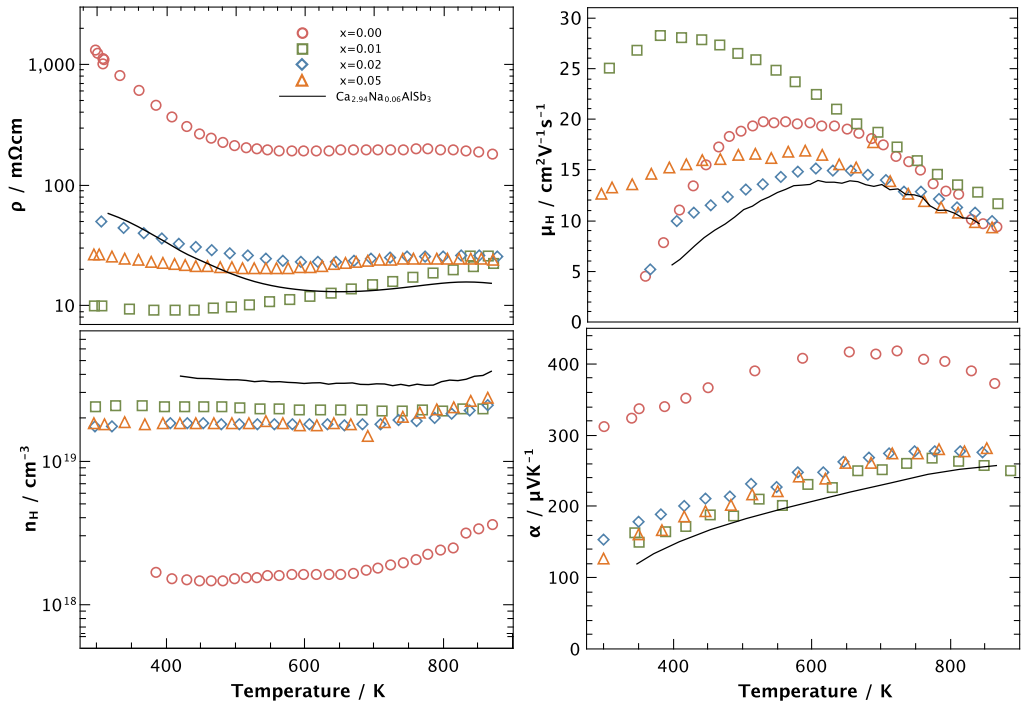

Figure 5.15: Temperature dependence of the electrical resistivity, ρ, the Hall carrier concentration, n_H, the Hall mobility, μ_H, and the Seebeck coefficient, α, of $Ca_3Al_{1-x}Zn_xSb_3$. Experimental data is compared to $Ca_{2.94}Na_{0.06}AlSb_3$ data (black line).[5]

due to intrinsic defects. As expected, the carrier concentration increases upon substitution of Zn^{2+} on the Al^{3+} site due to the introduction of holes. Doped samples behave extrinsically, with temperature independent carrier concentrations up to 700 K, after which the carrier concentration increases abruptly, likely due to carrier excitation across the band gap (E_g ~0.6 eV[5]). Zinc doping introduces significantly fewer holes than predicted. Ultimately, the maximum carrier concentration achieved by doping with zinc is lower than that achieved upon sodium doping, suggesting a lower solubility limit for zinc.

Impurities at grain boundaries, such as oxidation or possibly phases that are too small to observe by SEM, are already known to impede charge transport in Ca_3AlSb_3, leading to reduced mobility at low temperatures.[5] Grain boundaries are also a likely place for Zn to accumulate, potentially causing the reduced doping effectiveness ob-

served in this study. This supposition is supported by the anomalous carrier concentration of the $x = 0.01$ sample, which is higher than that of the samples with $x = 0.02$ and 0.05, and may be attributable to its large grain size and thus lower interfacial surface area.

Grain size also correlates with the carrier mobility of the $Ca_3Al_{1-x}Zn_xSb_3$ samples in this study. The Hall mobility, calculated from the measured Hall coefficient (R_H) and resistivity (ρ), is shown in Figure 5.15. For samples with sub-micron grains ($x = 0.0$, $x = 0.02$, and $x = 0.05$), the Hall mobility at low temperatures exhibits an exponential temperature dependence ($\mu_H = \mu_0 e^{-E_A/k_B T}$) indicative of a barrier at the grain boundaries, such as an oxide layer, requiring an activation energy to overcome. At higher temperatures (> 600 K) the mobility is limited by acoustic phonon scattering, for which the temperature dependence is given by $\mu_H \propto T^{-\nu}$, with ν between 1 and 1.5 for degenerate and non-degenerate behavior, respectively.[76] However, the sample with the nominal composition of $Ca_3Al_{0.99}Zn_{0.01}Sb_3$ exhibits larger Hall mobilities than all other compositions, with acoustic phonon scattering dominating transport above 400 K. This suggests that since larger grains (inset of Figure 5.16) result in a lower interfacial surface area, a less pronounced activation process in the temperature dependence of the Hall mobility in this sample leads to higher mobility at lower temperatures. Larger grain sizes may also reduce grain boundary scattering in the $x = 0.01$ sample.

The electrical resistivity exhibits a negative slope at low temperatures (Figure 5.15), due to the activated mobility behavior ($\rho = 1/ne\mu$). At higher temperatures the resistivity behaves as expected for a heavily-doped semiconductor.

The Seebeck coefficients are positive, consistent with the p-type carrier concentrations, and the temperature dependence is shown in Figure 5.15. The Seebeck coefficients of undoped Ca_3AlSb_3 increases up to a temperature of 700 K, at which point thermally activated electrons reduce the thermoelectric voltage, resulting in a decay of the Seebeck coefficient. As expected for a heavily doped semiconductor, the Seebeck coefficients decrease with increasing carrier concentrations. In order to compare the influence of Zn and Na as dopants on the electronic structure of this ma-

terial, the Pisarenko relation is shown in Figure 5.17. The experimental Seebeck and carrier concentrations were measured at 700 K, and the dashed line was generated using the single parabolic band model described in Section 2.3, with a valence band effective mass of $m^* = 0.8\ m_e$. Both Zn- and Na-doped materials are well-described by the same model, suggesting that using Zn as a dopant does not effect the band structure of the compound.

Thermal Transport Properties The total thermal conductivities are shown in Figure 5.16. The electronic contribution, κ_{el}, to the total thermal conductivity can be estimated from the Wiedemann-Franz relation ($\kappa_{el} = LT/\rho$). In this study, the Lorenz numbers L are calculated from the experimental Seebeck coefficients. Subtracting the electronic term from the total thermal conductivity leaves the lattice thermal conductivity and the bipolar contribution. No significant bipolar contribution can be observed in this temperature range, and therefore the resulting term is hereafter referred to as lattice thermal conductivity.

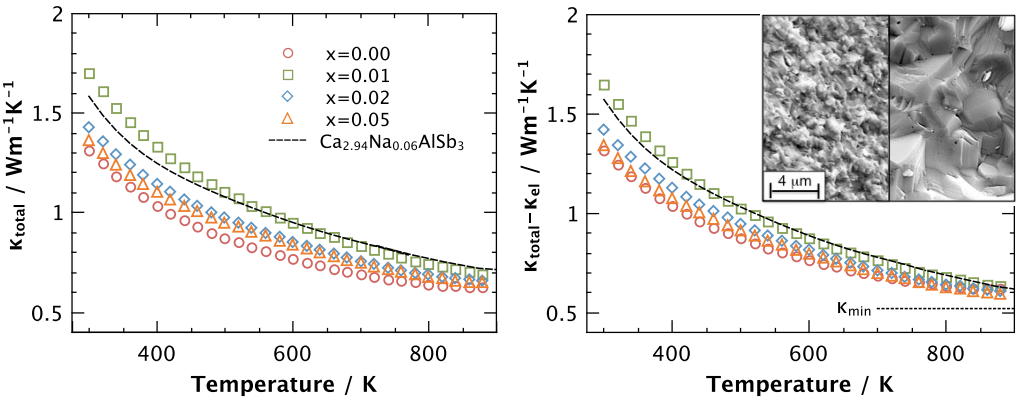

Figure 5.16: Total thermal conductivity (top) and lattice thermal conductivity (bottom) of $Ca_3Al_{1-x}Zn_xSb_3$. The inset illustrates the smaller grains (left) for the compositions with $x = 0.00$, 0.02, and 0.05 and larger grain sizes for $x = 0.01$ (right).

The lattice thermal conductivity is well-described by a T^{-1} dependence, characteristic of phonon-phonon Umklapp scattering.[79] The influence of Zn on the lattice thermal conductivity seems to be negligible, as reported in the sodium-doped

Ca_3AlSb_3. However, the sample with nominal composition $Ca_3Al_{0.99}Zn_{0.01}Sb_3$ exhibits a higher thermal conductivity at lower temperatures. This can be attributed to the larger grains in this sample. In contrast, the sub-micron grains in the other samples result in more boundary scattering, and thus reduced lattice thermal conductivities at lower temperatures. In all samples, the lattice thermal conductivities approach the minimum thermal conductivity κ_{min}, which was calculated using speed of sound measurements and Cahill's formula for disordered crystals.[5, 121]

Figure of Merit The figure of merit of $Ca_3Al_{1-x}Zn_xSb_3$ is shown in Figure 5.17. Doping with zinc increases the figure of merit, leading to a zT of 0.5 at 900 K for $x = 0.01$. Compared with the Na-doped samples of our previous investigation, all of the Zn-doped samples exhibit enhanced zT at intermediate temperatures, which can be attributed to their higher carrier mobilities. The $x = 0.01$ sample, which has the largest grain size and thus the highest mobility, shows the largest degree of zT enhancement. However, the peak zT values of the sodium-doped Ca_3AlSb_3 samples cannot be achieved with zinc due to its limited dopant effectiveness when compared to Na.

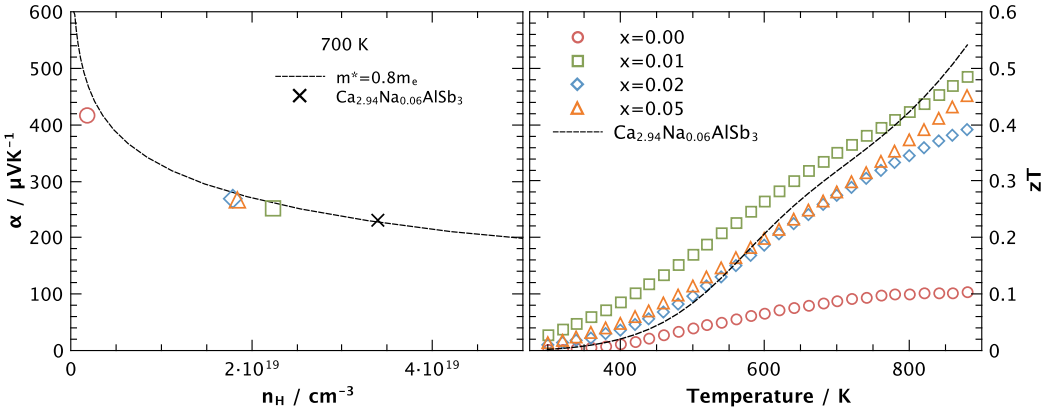

Figure 5.17: Experimental Seebeck coefficients as a function of carrier concentration (left) and figure of merit zT with temperature of $Ca_3Al_{1-x}Zn_xSb_3$.

Conclusion The thermoelectric properties of Zn-doped Ca_3AlSb_3 were compared to the previous report of Na-doped Ca_3AlSb_3. A similar band mass and lattice thermal conductivity is observed regardless of whether Zn or Na is the dopant. However, zinc exhibits a lower solubility limit than sodium, resulting in lower carrier concentrations and a lower peak figure of merit, because the optimum carrier concentration for this material cannot be reached via doping with zinc. This study also shows the effect of different grain sizes on the thermoelectric transport properties, with larger grains leading to higher thermal conductivities and higher mobilities at lower temperatures, due to reduced scattering of phonons and electrons at the grain boundaries. Ultimately, we find that while larger grain size has little effect on the high temperature properties, the reduction of grain boundary surface area improves the figure of merit at intermediate temperatures. This work shows that the common strategy to use nanostructured materials does not always lead to an improved figure of merit. Other competing factors such as a reduction in mobility may overwhelm the improvement of the lattice thermal conductivity.

Chapter 6

Thermoelectric properties of Sr_3GaSb_3

6.1 Introduction

The previous chapters reported on the thermoelectric properties of several compounds with promising figures of merit, including Ca_3AlSb_3 and $Ca_5Al_2Sb_6$ (M=Al, Ga, In) compounds, which form structures characterized by infinite, parallel chains of corner-sharing $AlSb_4$ tetrahedra. Further improvements to zT in this class of compounds might be achieved by further reducing the acoustic contribution to the lattice thermal conductivity ($\kappa_{acoustic}$), given by Eq. 6.1 in the limit of Umklapp scattering.

$$\kappa_{acoustic} = \frac{(6\pi^2)^{2/3}}{4\pi^2} \frac{\bar{M}\nu_s^3}{TV^{2/3}\gamma^2} \frac{1}{N^{1/3}} \tag{6.1}$$

Here, $\bar{M}$ and V are average atomic mass and atomic volume, respectively, ν_s is the average speed of sound, γ is the Grüneisen parameter, and N is the number of atoms per unit cell [8]. Since $\nu_s \propto \sqrt{E}/\sqrt{d}$, where E is stiffness and d is density, heavy atoms and soft bonds lead to low ν_s and thus low κ_L. This motivates our current study of the compound Sr_3GaSb_3, which has not been previously investigated for thermoelectric applications [122]. While Sr_3GaSb_3 is a chain-forming compound

similar to Ca_3AlSb_3 and $Ca_5Al_2Sb_6$, it has twice as many atoms per unit cell (N=56), and significantly higher density. Additionally, our previous study of the $Ca_5M_2Sb_6$ system suggests that M = Ga leads to a greater degree of covalent bonding in the anionic sub-structure than M = Al, which leads in turn to a lighter band mass and higher mobility, further motivating the current study [74, 73].

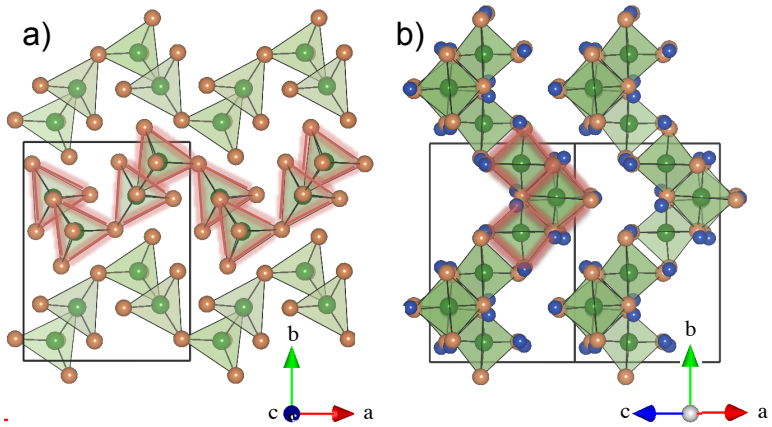

Figure 6.1: (a) Sr_3GaSb_3 contains unique chains of corner-sharing $GaSb_4$ tetrahedra, formed from four-tetrahedra repeat units. Ga atoms are green, Sb are orange, and Sr atoms are not shown. (b) The structure of Sr_3GaSb_3 viewed down the [101] axis, with chains going into the page (Sr atoms shown in blue). In both views, a single chain is highlighted in red.

Sr_3GaSb_3 is the only compound known to crystallize in a unique, chain-based structure that, according to Schäfer *et al.*, can be considered a connecting link between the structures based on either linear chains or isolated tetrahedra-pairs formed by all other known A_3MPn_3 compounds (A = Ca, Sr, Ba, M = Al, Ga, In, and Pn = P, As, Sb) [122]. The monoclinic structure of Sr_3GaSb_3 (space group $P2_1/n$, lattice parameters a = 11.855 Å, b = 14.649 Å, c = 11.876 Å, and β angle = 109.963°) contains infinite, close packed, non-linear chains of corner sharing tetrahedra, characterized by four-tetrahedra repeat units, as shown in Figure 7.1a). This four-tetrahedra periodicity in Sr_3GaSb_3 leads to a larger unit cell than that of Ca_3AlSb_3, which is only one tetrahedron wide along the chain direction. The chains in Sr_3GaSb_3 are aligned along the [101] direction, shown pointing into the page in Figure 7.1(b)). A single chain is highlighted in red. Note that while the chains appear to overlap with

nearby chains to form zigzagging planes, staggering along the [101] direction prevents strong interactions between neighboring chains.

Here we use high temperature thermal and electronic transport measurements to characterize the thermoelectric properties of Sr_3GaSb_3. Doping with Zn^{2+} on the Ga^{3+} site is used to optimize the electronic properties according to a single band model. In addition, we have employed electronic structure calculations to shed light on the role of bonding in the electronic transport properties of Sr_3GaSb_3.

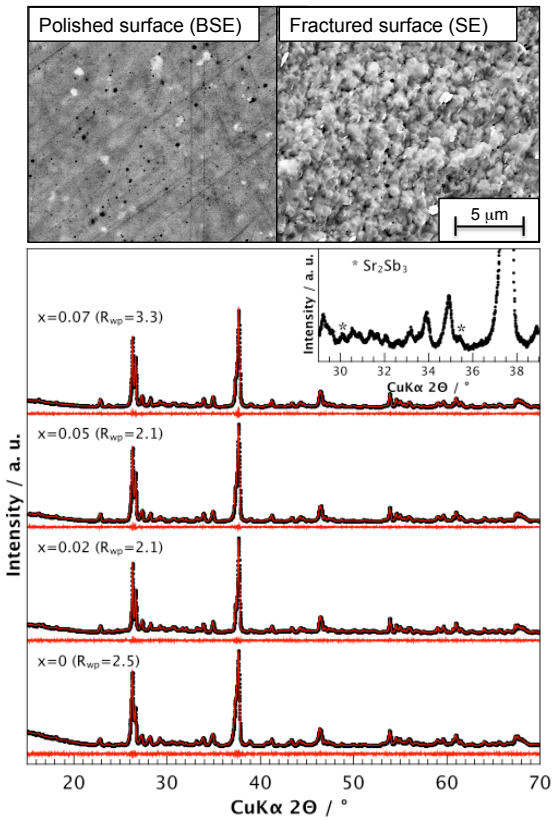

Figure 6.2: Top: back-scattered electron image of a polished Sr_3GaSb_3 sample reveals the secondary phase Sr_2Sb_3 as white specks, while secondary electron imaging of a fracture surface shows the very small grain size ($< 1\,\mu m$). Bottom: X-ray diffraction data for $Sr_3Ga_{1-x}Zn_xSb_3$, including profile fit, profile difference, and profile residuals from the corresponding Pawley refinement, including the secondary phase Sr_2Sb_3. Inset: the reflections indexed to the impurity phase are marked by asterisks.

6.2 Results and Discussion

Following ball milling and hot pressing, the polycrystalline $Sr_3Ga_{1-x}Zn_xSb_3$ (x = 0, 0.02, 0.05, and 0.07) samples had geometric densities of $\sim$ 98% of the theoretical density. Scanning electron microscopy analysis using backscattered electrons reveals small, light-colored precipitates (see upper left panel of Figure 6.2), identified by energy dispersive spectroscopy as the Zintl phase Sr_2Sb_3. This phase appears to comprise approximately 1-3 vol% of each sample. X-ray diffraction (XRD) confirms that Sr_3GaSb_3 and Sr_2Sb_3 were the only phases present in samples with x = 0.0 - 0.07 (shown in Figure 6.2). The inset shows a magnified view in which the most prominent Sr_2Sb_3 peaks are marked with asterisks. The fraction of this phase was comparable in each of the samples with x = 0.0 - 0.07. In the sample with nominal composition $Sr_3Ga_{0.9}Zn_{0.1}Sb_3$, additional phases were present, including $SrZn_2Sb_2$, indicating that the solubility limit of Zn in Sr_3GaSb_3 was exceeded. We have therefore not included the transport properties of this composition. In all samples, the grain size after hot pressing was extremely small, estimated from fracture surfaces to be in the sub-micrometer range (upper right panel in Figure 6.2), in accordance with the broad profiles of the XRD reflections. No obvious texturing was seen in the diffraction patterns, despite the anisotropic crystal structure.

Electronic Structure Sr_3GaSb_3 forms a valence precise crystal structure that can be described within the Zintl formalism as follows: the highly electropositive Sr (3 Sr^{2+}) atoms donate their valence electrons to the anionic chains. Two of the Sb atoms making up the chains have only one covalent bond, leading to a valence state of -2, while one Sb atom is shared between two tetrahedra, leading to two covalent bonds and a valence state of -1. Assigning a valence state of -1 to the four-bonded Ga leads to overall charge balance and the formation of the covalent anionic chains [35].

The basic features of this simple bonding description are reflected in the calculated density of states, shown in Figure 6.3a. The prominent Ga and Sb electronic states deep in the valence band (-4 to -6 eV) and at the conduction band minimum

likely correspond to Ga-Sb bonding and anti-bonding interactions, respectively. The valence band maximum is dominated by Sb states, likely arising from non-bonding Sb lone-pairs. In contrast, the conduction band is formed primarily by Ga-Sb anti-bonding states and by Sr states at higher energies, consistent with the assumption that Sr donates its valence electrons to form the anionic substructure. A band gap of $\sim 0.75\,\text{eV}$ is predicted, qualitatively consistent with the experimentally observed behavior described below.

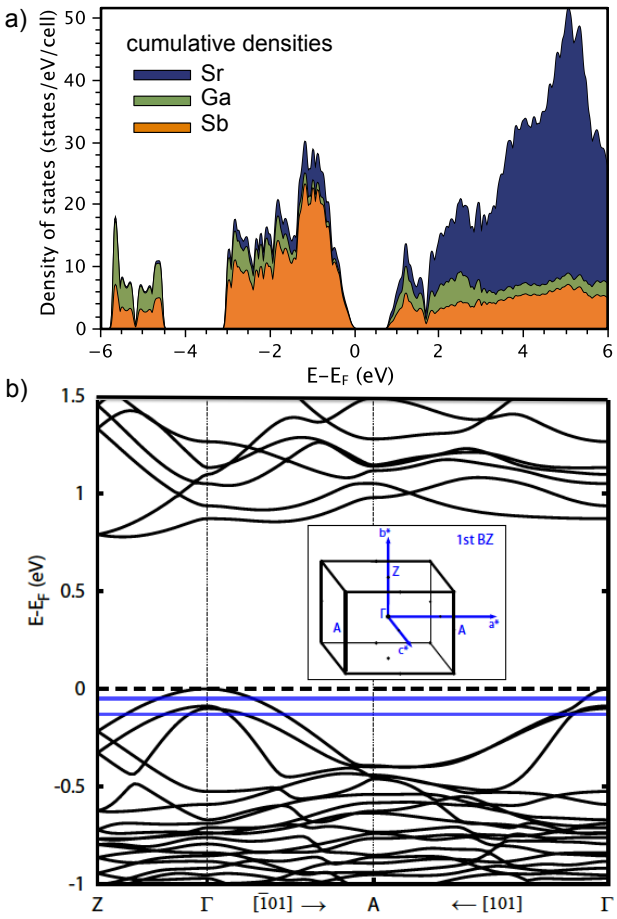

Figure 6.3: (a) Density of states and (b) band structure of Sr_3GaSb_3 reveal an indirect band gap of $\sim 0.75\,\text{eV}$. The upper and lower blue lines correspond to carrier concentrations of 10^{19} and 10^{20} holes/cm^3, respectively. Inset: Brillouin zone of Sr_3GaSb_3 with selected k-space directions labeled.

The electronic band structure of Sr_3GaSb_3 is shown in Figure 6.3b in the k-space direction parallel to the $GaSb_4$ chains (Γ-$A_{[101]}$), and in the two perpendicular direc-

tions (Γ-Z and Γ-$A_{[\bar{1}01]}$). The k-space points Γ, A, and Z are labeled in the Brillouin zone shown in the inset. The band structure is characterized by an indirect band gap ($\sim$0.75 eV), with the valence band maximum at Γ and the conduction band minimum between Γ and Z. The upper and lower blue lines correspond to carrier concentrations of 10^{19} and 10^{20} holes/cm^3, respectively. At energies very close to the valence band maximum (0 to -0.1 eV), the dispersion is anisotropic, with the effective mass along the chains ($m^*_{[101]} = 0.18\,m_e$) smaller than the mass in the perpendicular directions ($m^*_{[\bar{1}01]} = 0.57\,m_e$ and $m^*_{[010]} = 0.66\,m_e$). In contrast, the two additional bands with maxima at $\sim$ -0.1 eV are nearly isotropic in the directions considered. When electrons are scattered primarily by acoustic phonons, as is the case in most known thermoelectric materials, the improvement in carrier mobility conferred by a light band mass outweighs the detrimental effect that low m^* has on α. In this case, the thermoelectric quality factor is given by $\beta \propto \frac{N_v}{m_i^* \kappa_L}$, where m_i^* is the mass of a single hole pocket along the conduction direction [73, 166]. This suggests that the light band mass in Sr_3GaSb_3, particularly in the direction of the chain substructures ($m^*_{[101]}$), may be advantageous.

The number of bands contributing to transport (N_v) at a given carrier concentration influences a material's figure of merit, as illustrated by the thermoelectric quality factor. If N_v is high, it is possible to simultaneously have light bands (small m_i^*) and large density of states effective mass. In Sr_3GaSb_3, only one band contributes to transport at energies very close to the valence band maximum. In heavily doped Sr_3GaSb_3 ($n_H > 10^{20}$ holes/cm^3), the contribution from the two bands with maxima at about -0.1 eV could potentially lead to $N_v = 3$.

Electronic Transport Properties Figure 5.15b shows the measured Hall carrier concentrations (n_H) of $Sr_3Ga_{1-x}Zn_xSb_3$ samples as a function of temperature. Despite Sr_3GaSb_3 being a valence-precise Zintl compound, the undoped material has an extrinsic p-type carrier concentration of 4×10^{18} holes/cm^3 at room temperature, most likely due to intrinsic defects in the crystal structure. The resistivity of undoped Sr_3GaSb_3 is very high (Figure 5.15a), decreasing due to thermal activation of carriers

into the conduction band only at temperatures above 800 K.

With each substitution of Zn^{2+} on a Ga^{3+} site we expect to introduce one additional free hole (h^+), due to the difference in valence states [37]. In many Zintl compounds, this simple assumption works well for predicting n_H of doped samples (i.e. $Yb_{14}Al_{1-x}Mn_xSb_{11}$, $Ba_8Ga_{16-x}Ge_{30+x}$[21, 6]), indicating that the dopant primarily substitutes on the intended crystallographic sites. However, in Sr_3GaSb_3, in common with Ca_3AlSb_3 [128], doping with Zn results in only a fraction of the predicted hole concentration. For example, when x=0.07 (equivalent to a synthetic concentration of 1 at.% Zn) we would predict $n = 2.1\text{x}10^{20}\,h^+/cm^3$. However, the measured n_H is only $5\text{x}10^{19}\,h^+/cm^3$. If each measured hole is assumed to result from a Zn atom on a Ga site, then only *one fourth* of the synthetic Zn content resides on the intended site, while the remainder may form secondary phases too small to identify, or perhaps become trapped at grain boundaries. However, estimating the matrix Zn content from the measured Hall coefficient can be misleading. Sources of error might include Zn defects with an effective charge other than +1, formation of compensating n-type defects [167], or a Hall factor (r_H=n/n_H) that deviates significantly from unity.

As a function of temperature, n_H in $Sr_3Ga_{1-x}Zn_xSb_3$ is constant at low temperatures, indicative of extrinsic transport, and increases at high temperature as intrinsic carriers are activated across the band gap. The increase in n_H leads to the decrease in electrical resistivity with Zn-doping shown in Figure 6.4b.

The Hall mobility, μ_H, is shown in Figure 6.4c, calculated from $\rho = 1/n_H e\mu_H$. At low temperatures (T < 500 K), μ_H exhibits a positive temperature dependence that can be fit using $\mu_H \propto e^{E_A/k_BT}$, where E_A is the activation energy associated with a potential barrier [168]. Such behavior may arise from barriers at the grain boundaries, such as oxide layers or secondary phases, requiring an activation energy to overcome. Our previous study of Ca_3AlSb_3 indicates that with the correct microstructure, it is possible to avoid this activated behavior, drastically increasing electrical conductivity [128]. At higher temperatures (> 600 K) the mobility in $Sr_3Ga_{1-x}Zn_xSb_3$ is limited by acoustic phonon scattering, for which the temperature dependence is given by $\mu_H \propto T^{-\nu}$, with ν between 1 and 1.5 for degenerate and non-degenerate behavior,

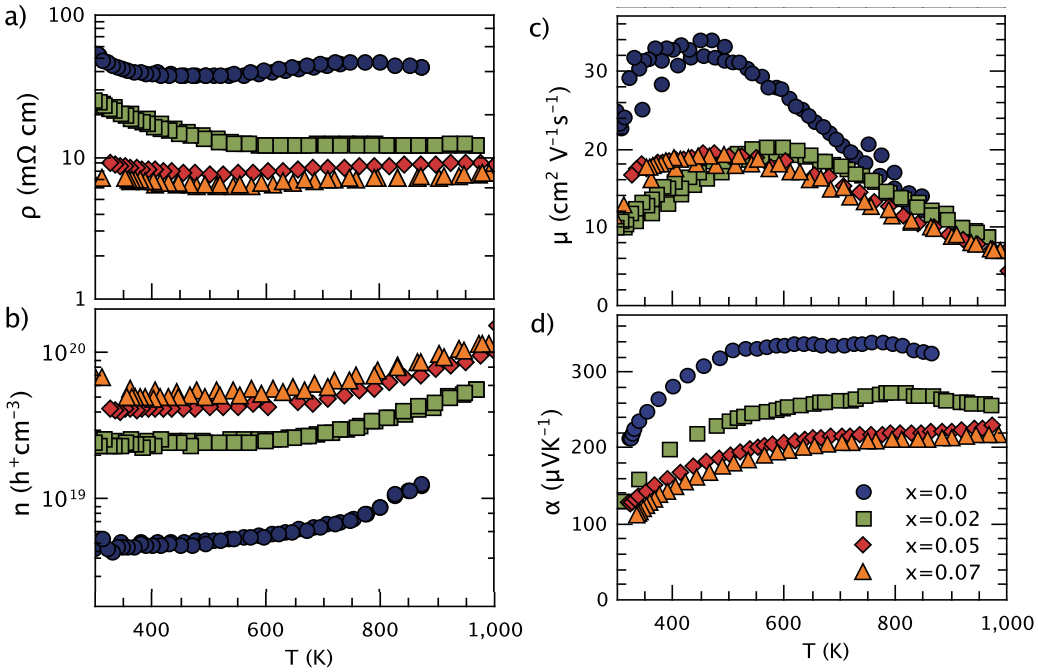

Figure 6.4: The temperature dependence of (a) the electrical resistivity, ρ, and (b) the Hall carrier concentration, n_H, in $Sr_3Ga_{1-x}Zn_xSb_3$ illustrates the transition towards degenerate semiconducting behavior upon Zn doping. (c) The Hall mobility, μ_H, reveals activated behavior at low temperature and (d) the Seebeck coefficient, α, becomes more metallic with increasing Zn.

respectively [76].

The Seebeck coefficients, α, of $Sr_3Ga_{1-x}Zn_xSb_3$ samples, shown in Figure 6.4d), are positive, consistent with the p-type carrier concentrations. The Seebeck coefficient of undoped Sr_3GaSb_3 increases up to a temperature of 700 K, at which point thermally activated electrons result in a decay of α. From the resulting maximum (α_{max}=340 μVK^{-1}, T_{max}=700 K), a rough estimate of the band gap using $E_g = 2e\alpha_{max}T_{max}$ [154] yields $E_g \sim 0.5$ eV, which is in general agreement with the results of the DFT calculations (see Figure 6.3). As expected, the Seebeck coefficients decrease with increasing carrier concentrations. This is best illustrated by the Pisarenko relation shown in the left panel of Figure 6.6a, with experimental α and n_H (diamond symbols) obtained at 700 K. The solid curve was generated using the single parabolic band (SPB) model described in Section 2.3, with a valence band effective mass of $m^* = 0.9\, m_e$. All of the doped samples in this study appear to be well-described by m^*=$0.9\, m_e$ at 700 K, sug-

gesting that, within experimental uncertainty, it is not possible to see any evidence of multi-band behavior at these doping levels. While not shown here, the same effective mass also provides a good fit for the experimental Seebeck coefficients at 300 K and 500 K.

To investigate the possibility of anisotropic transport properties, the Hall and Seebeck coefficients of $Sr_3Ga_{0.93}Zn_{0.07}Sb_3$ were measured on disks cut in different directions (perpendicular and parallel to the hot pressing direction). A ∼5% disparity in resistivity measured to 1000 K appeared to stem from a higher hole concentration in the perpendicular slice, while the mobility was identical in both directions. The difference in the Seebeck coefficients at 300 K was within the measurement uncertainty of 5%. Together, these results suggest that the anisotropy of Sr_3GaSb_3 does not significantly influence transport properties in our polycrystalline samples. This is in agreement with XRD measurements, which show no signs of preferred grain orientation (Figure 6.2).

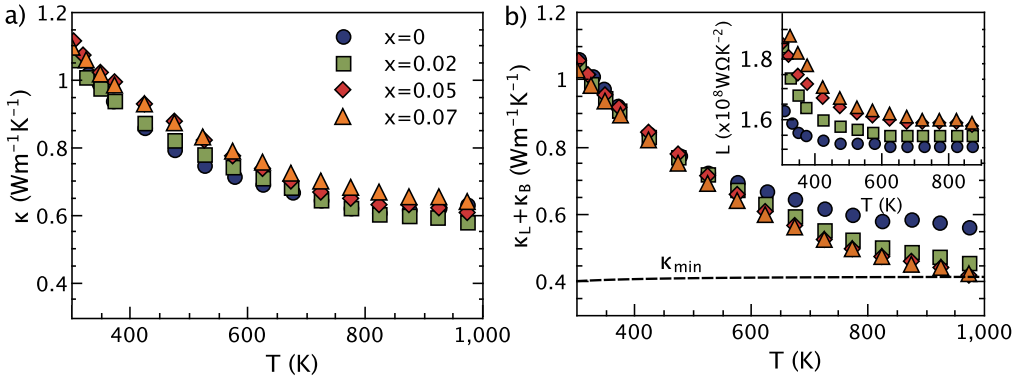

Figure 6.5: (a) Total thermal conductivity and (b) lattice thermal conductivity of $Sr_3Ga_{1-x}Zn_xSb_3$. The calculated minimum lattice thermal conductivity κ_{min} is shown as a broken line, and the inset shows the calculated Lorenz numbers generated using an SPB model [6].

Thermal Transport Properties The total thermal conductivity (κ) is shown in Figure 6.5a. The electronic contribution to the thermal conductivity (κ_e) was estimated using the Wiedemann-Franz relation $\kappa_e = LT/\rho$, where the Lorenz number,

L, was determined from experimental Seebeck coefficients using an SPB model (inset of Figure 6.5) [6]. Subtracting κ_e from κ leaves the combined lattice (κ_L) and bipolar (κ_B) contributions shown in Figure 6.5b). Of the samples in this study, only undoped Sr_3GaSb_3 exhibits a significant bipolar contribution, as evidenced by the increase in $\kappa_L + \kappa_B$ at high temperatures relative to the doped samples [157]. In the remaining compositions (x = 0.02, 0.05, 0.07), the lattice thermal conductivity is the dominant term, decreasing with the 1/T temperature dependence expected when scattering is dominated by Umklapp processes (Eq. 6.1) [8].

The large number of atoms per unit cell in Sr_3GaSb_3 (N=56), leads, by definition, to a phonon dispersion with 3 acoustic modes and 55×3 optical modes. Such complexity in the dispersion leads to both enhanced Umklapp scattering and flattened, low velocity optical modes that contribute very little to heat transport [8, 7]. These features, combined with the small grain size in our Sr_3GaSb_3 samples, lead to the extremely low lattice thermal conductivity observed in this material. To estimate the minimum lattice thermal conductivity, κ_{min}, for Sr_3GaSb_3, and thus to determine whether further nano structuring would be beneficial, we have employed Cahill's formula for disordered crystals [121, 80]. κ_{min} is dependent on the longitudinal and transverse sound velocities, which were determined from ultrasonic measurements to be 3750 m/s and 2130 m/s, respectively. These yield an estimated Debye temperature of θ_D = 243 K and κ_{min}=0.43 $Wm^{-1}K^{-1}$. At high temperature, the lattice thermal conductivity of Sr_3GaSb_3 approaches the estimated κ_{min}, in common with Ca_3AlSb_3 and $Ca_5Al_2Sb_6$, adding to the growing body of evidence suggesting that large unit cell size leads to the glass-like high temperature κ_L observed in a number of thermoelectric materials.

Figure of Merit The figure of merit of $Sr_3Ga_{1-x}Zn_xSb_3$ is shown in Figure 6.6b) as a function of temperature. The transition from nondegenerate behavior to degenerate semiconducting behavior upon doping with zinc leads to an increase in the maximum zT from 0.4 for x=0 to greater than 0.9 when x=0.07. To provide a rough estimate of the optimal carrier concentration in this material, we have employed an SPB model at

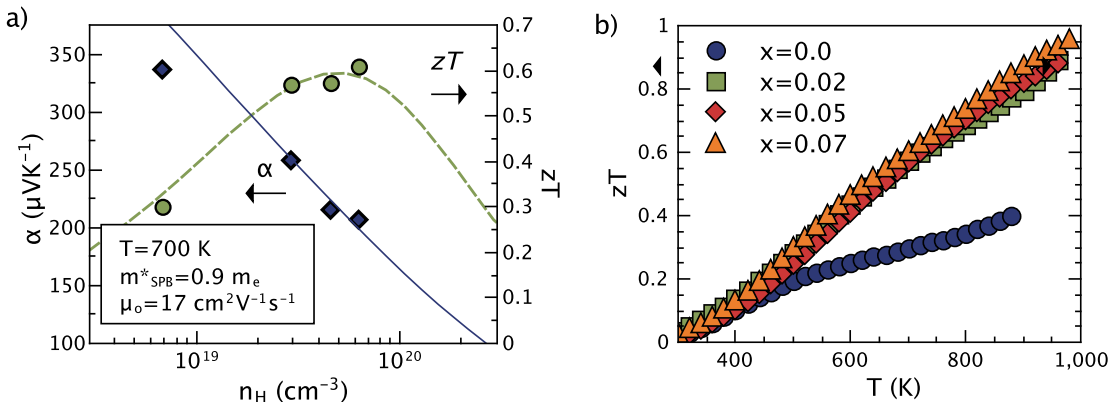

Figure 6.6: (a) Seebeck coefficients (diamonds) and zT (circles) vary with carrier concentration approximately according to an SPB model at 700 K. The solid and broken curves represent the predicted SPB behavior of α and zT, respectively, assuming $m^* = 0.9\,m_e$, $\mu_0 = 17\,\mathrm{cm^2V^{-1}s^{-1}}$ and $\kappa_L = 0.55\,\mathrm{Wm^{-1}K^{-1}}$. (b) The measured figure of merit of $Sr_3Ga_{1-x}Zn_xSb_3$ exceeds 0.9 when heavily doped.

700 K (see Figure 6.6a). At 700 K, it is reasonable to assume that extrinsic carriers still dominate transport and acoustic phonons are the primary scattering source. Using input parameters $m^* = 0.9\,m_e$, $\mu_0 = 17\,\mathrm{cm^2V^{-1}s^{-1}}$, and $\kappa_L = 0.55\ \mathrm{Wm^{-1}K^{-1}}$, the predicted optimum carrier concentration is approximately $5\mathrm{x}10^{19}\,\mathrm{h^+/cm^3}$. The doped samples in this study have carrier concentrations clustered around this optimum, explaining their similar zT values.

6.3 Conclusion

Here, we have described a new thermoelectric material, Sr_3GaSb_3, which has a crystal structure characterized by chains of corner-linked tetrahedra, similar to the polyanions found in the previously studied Zintl compounds, $Ca_5Al_2Sb_6$ and Ca_3AlSb_3. In Sr_3GaSb_3, however, the chains are characterized by a repeating unit containing four tetrahedra, as opposed to the single tetrahedra repeat-unit found in $Ca_5Al_2Sb_6$ and Ca_3AlSb_3. The resulting large unit cell and comparatively high density in Sr_3GaSb_3 combine to yield the exceptionally low lattice thermal conductivity observed in this study ($\kappa_L = 0.45\,\mathrm{Wm^{-1}K^{-1}}$ at 1000 K). High temperature transport measurements

reveal that Sr_3GaSb_3 is a nondegenerate p-type semiconductor, with a relatively large band gap ($E_g > 0.5\,\mathrm{eV}$) and high electronic mobility. Density Functional calculations are in qualitative agreement, predicting a band gap of $\sim$0.75 eV and a light valence band edge ($\sim 0.5\,m_e$). Doping with Zn^{2+} on the Ga^{3+} site leads to degenerate semiconducting behavior, allowing us to obtain p-type carrier concentrations near the optimum value predicted by a single parabolic band model. The combination of low lattice thermal conductivity, reasonable electronic mobility, and a sufficiently large band gap to maintain degenerate behavior at high temperature leads to a zT of 0.9 at 1000 K. Compared with previously studied chain-based Zintl compounds, both the peak zT and integrated zT of Zn-doped Sr_3GaSb_3 samples are significantly higher.

Chapter 7

Thermoelectric properties of Sr_3AlSb_3

7.1 Introduction

Among compounds with the A_3MPn_3 stoichiometry (A = Ca, Sr, Ba, M = Al, Ga, In, and Pn = P, As, Sb), three distinct types of polyanionic structures are known. The relationship between the size of each atomic species and the resulting structure type is rationalized by G. Cordier and H. Schäfer et al. in ref. [122]. When the cation is small (e.g., Ca_3AlSb_3, Ca_3AlAs_3 [12, 160]) or when the pnictogen species is small (e.g., Sr_3InP_3 [122]), infinite simple chains of corner-linked MPn_4 tetrahedra are formed. In contrast, very large cations lead to the formation of isolated M_2Pn_6 moieties formed from two edge-sharing tetrahedra (e.g., Ba_3AlSb_3, Ba_3GaSb_3 [160, 158]). Less clear-cut is the case when the pnictogen species is large but the cation is of an intermediate size, such as in the compounds Sr_3GaSb_3 [122] and Sr_3AlSb_3 [14]. Here, the slight size difference of the metal species (M) leads to two different polyanion types; Sr_3GaSb_3 forms unique tetrahedral chains (distinct from those of Ca_3AlSb_3), while Sr_3AlSb_3 forms the tetrahedral pairs that are also found in the Ba-based compounds.

Here we report on the properties of Sr_3AlSb_3 (space group *Cmca* [14]), which, like Ca_3AlSb_3, is appealing for thermoelectric applications due to its earth abundant, non-toxic elements. As shown in Figure 7.1, the anionic units in Sr_3AlSb_3 are isolated,

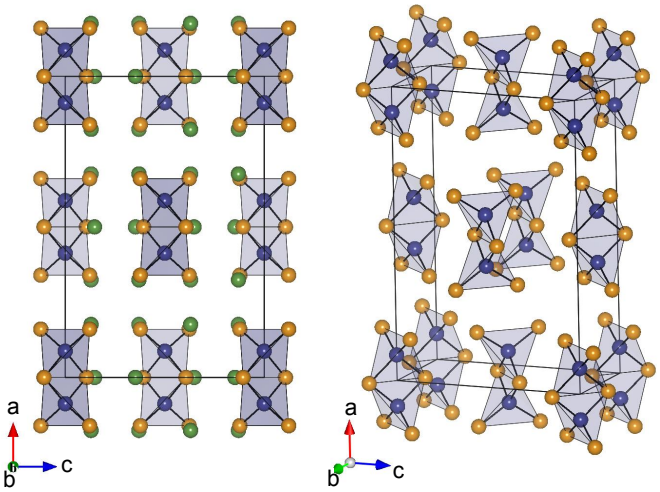

Figure 7.1: (a) The orthorhombic crystal structure of Sr_3AlSb_3 (space group *Cmca*) contains 56 atoms per primitive cell [14]. Sr atoms are shown in green, Sb in orange, and Al in blue. (b) Each isolated anionic moieties is made up of two edge-sharing tetrahedra (for clarity, Sr is not shown) [14].

edge-sharing, tetrahedral pairs, aligned in the [100] direction (a-axis). The tetrahedral pairs can be described as $[Al_2Sb_6]^{12-}$ units. Each pair contains two tetrahedrally coordinated Al with a formal valence of -1, four Sb^{2-} bonded to a single Al atom, and two "bridging" Sb^{1-} bonded to two Al atoms. The six surrounding Sr^{2+} cations provide overall charge balance, fulfilling the Zintl valence counting requirements. Each Sr_3AlSb_3 primitive cell contains 8 formula units (56 atoms) in common with Sr_3GaSb_3, suggesting an extremely low lattice thermal conductivity.

The current investigation of Sr_3AlSb_3 may shed additional light on the relationship between transport properties in Zintl phases and the connectivity of their covalently bonded substructures. With regard to dimensionality, the anionic unit in Sr_3AlSb_3 can be considered a connecting link between the 0-dimensional, isolated tetrahedra in $Yb_{14}MnSb_{11}$ and the 1-dimensional tetrahedral chains in Ca_3AlSb_3 and Sr_3GaSb_3. The effective mass in $Yb_{14}MnSb_{11}$ is quite high ($m^* \sim 3\ m_e$), leading to both a high Seebeck coefficient and low carrier mobility [21]. In contrast, both Ca_3AlSb_3 and Sr_3GaSb_3 have relatively low m^* ($< 1\ m_e$) and high mobility [5, 129]. Here, we use a combination of high temperature transport measurements and density functional

calculations to characterize the thermoelectric properties of Sr_3AlSb_3 and compare its properties to that of related Zintl compounds.

7.2 Results and Discussion

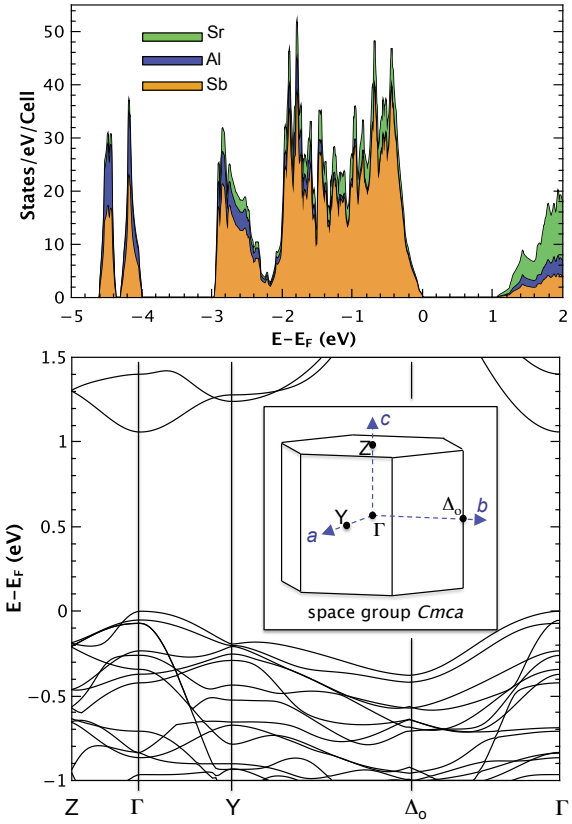

Figure 7.2: (top) Calculated site-projected density of states and (bottom) electronic band structure along the primary axes. The inset shows the 1st Brillouin zone with the k-points corresponding to each primary axis labeled.

Electronic Structure As a classic, valence-precise Zintl compound, Sr_3AlSb_3 is expected to be a semiconductor with a fully-filled valence band and empty conduction band. Density Functional calculations confirm these expectations, placing the Fermi level (E_F) within the band gap. As shown in the top panel of Figure 7.2, the calculated density of states exhibits a band gap of approximately 1.0 eV — significantly larger than that of Ca_3AlSb_3 or Sr_3GaSb_3. In common with other Sb-derived Zintl phases

[5, 129, 169], the valence band is heavily dominated by electronic states associated with the Sb anions, while the conduction band is primarily characterized by the cation, Sr.

The electronic band structure of Sr_3AlSb_3 is shown in Fig 7.2b in three perpendicular directions: Γ-Y, Γ-Δ_o, and Γ-Z, which correspond to the a, b, and c axes, respectively. A direct band gap is located at the Γ point. Parabolic fits to the top of the valence band along each axis yield the following values for the effective mass: $m^*_{\Gamma-Z}$= 0.21 m_e, $m^*_{\Gamma-Y}$= 1.80 m_e, $m^*_{\Gamma-\Delta}$= 1.25 m_e. The lowest band mass is in the Γ - Z direction, indicating that transport along the c-axis (perpendicular to the tetrahedral pairs) is preferred, rather than parallel to the tetrahedral pairs (a-axis). This suggests that, as each tetrahedral pair in Sr_3AlSb_3 is isolated, there may be no charge transport benefit relative to isolated tetrahedra. With regard to the number of bands contributing to transport (band degeneracy, N_V [17]), Sr_3AlSb_3 is comparable to Sr_3GaSb_3. Both phases have electronic dispersions with a single band forming the valence band edge and two additional bands with maxima at $E_F \sim$ -0.1 eV. If the Fermi level were lowered sufficiently via doping, an effective band degeneracy of N_v=3 could potentially be realized in Sr_3AlSb_3.

Synthetic Results Initial attempts to synthesis phase-pure Sr_3AlSb_3 via ball milling and hot pressing of stoichiometric quantities of Sr, Al, and Sb resulted in samples with a high fraction of impurity phases (>20%). We found that a drastic reduction in the impurity concentration could be achieved by increasing the amount of aluminum by 5%. In the following discussion, we refer to the undoped sample by its nominal, rather than its synthetic, composition: "Sr_3AlSb_3". An additional sample was synthesized by replacing 5% of the total Al content with Zn, and is referred to as "Zn-doped Sr_3AlSb_3".

The resulting samples were dense, but oxidized quickly in air. Figure 7.3 shows representative X-ray diffraction (XRD) patterns of both an undoped and Zn-doped sample in red. Rietveld fits using the reported structure of Sr_3AlSb_3 [14] are shown in black, while the difference profiles are given beneath. From the XRD patterns,

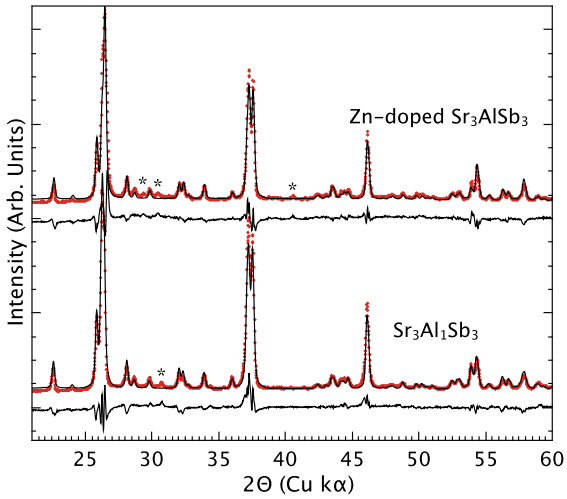

Figure 7.3: Comparing the XRD patterns of polycrystalline slices of Zn-doped and undoped Sr_3AlSb_3 (red symbols) with Rietveld fits (black curves) [14] reveals a small fraction of one or more secondary phases (marked by asterisks). The difference profiles are shown beneath each pattern.

both samples appear to crystallize primarily as Sr_3AlSb_3 with a small amount ($<$ 5 vol%) of one or more unidentified impurity phases (marked by asterisks in Figure 7.3). Additional peaks in the Zn-doped sample suggest that some or all of the Zn may have precipitated out as a secondary phase rather than occupying the intended Al site.

Electronic Transport Properties High temperature electronic transport measurements indicate that undoped Sr_3AlSb_3 is a nondegenerate semiconductor, consistent with the filled valence band and large band gap predicted from DFT. As shown in Figure 7.4 (a) and (d), the undoped sample exhibits high resistivity, ρ, that decreases with increasing temperature, and a large Seebeck coefficient, α, peaking at approximately 700 K. Estimating the band gap from the peak Seebeck coefficient (E_g=$2\alpha_{max}T_{max}$) of undoped Sr_3AlSb_3 yields E_g=0.6 eV.

Figure 7.4 (b) and (c) shows the Hall carrier concentration, n_H, and mobility, μ_H, of undoped Sr_3AlSb_3. The carrier concentration is low, and increases with temperature due to thermal activation of minority carriers. At high temperatures, μ_H

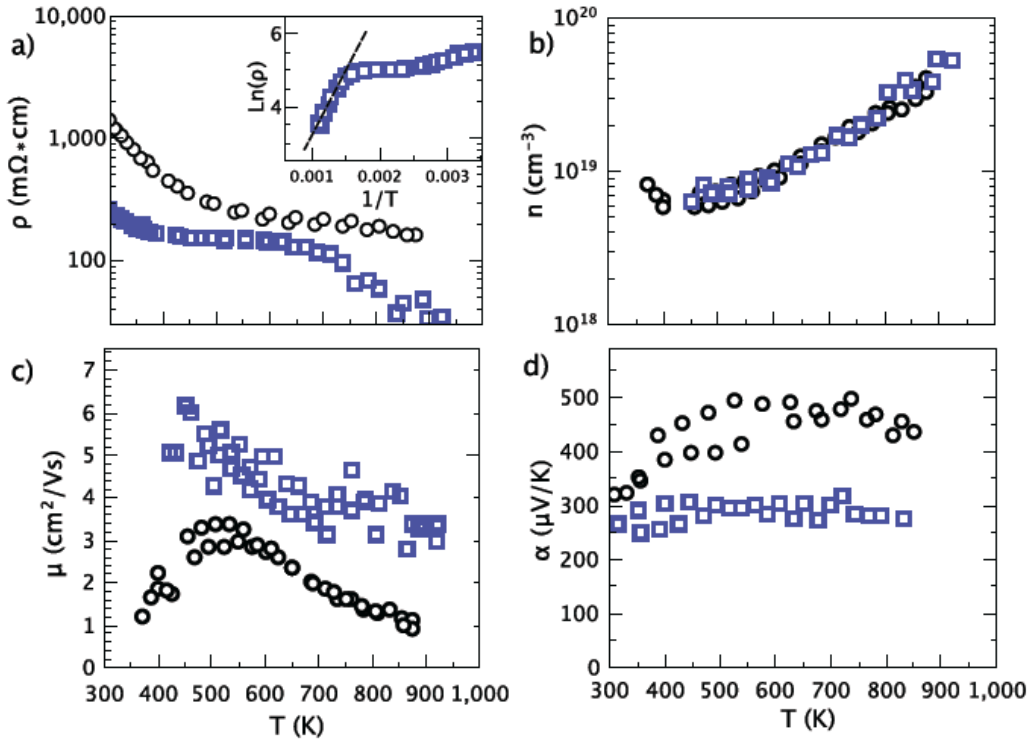

Figure 7.4: (a)The resistivity and (b) carrier concentration of undoped and nominally Zn-doped Sr_3AlSb_3 are indicative of intrinsic semiconducting behavior. A band gap of $E_g = 0.7$ eV was estimated from the nominally Zn-doped sample (see inset) (c) The Hall mobility of the undoped sample is comparable to that of $Yb_{14}MnSb_{11}$, and is increased by the addition of Zn. (d) The Seebeck coefficients are high, peaking at intermediate temperatures.

decreases with increasing temperature, as expected when acoustic phonons are the primary scattering source. Below 500 K, the temperature dependence of μ_H is indicative of an additional scattering source. This behavior is similar to that observed in the mobility of both Ca_3AlSb_3 and Sr_3GaSb_3 samples, which, in both cases, was attributed to grain boundary oxidation [5, 129]. In the absence of grain boundary oxidation, the magnitude of μ_H at room temperature in Sr_3AlSb_3 may be slightly greater than that of $Yb_{14}MnSb_{11}$ [21].

Simple electron counting predicts that each substitution of Zn^{2+} on an Al^{3+} site should create one free hole, h^+, leading to degenerate p-type semiconducting behavior. In several related phases, doping with Zn was found to be extremely effective, in each case leading to at least an order of magnitude increase in n_H [129, 128, 125]. However,

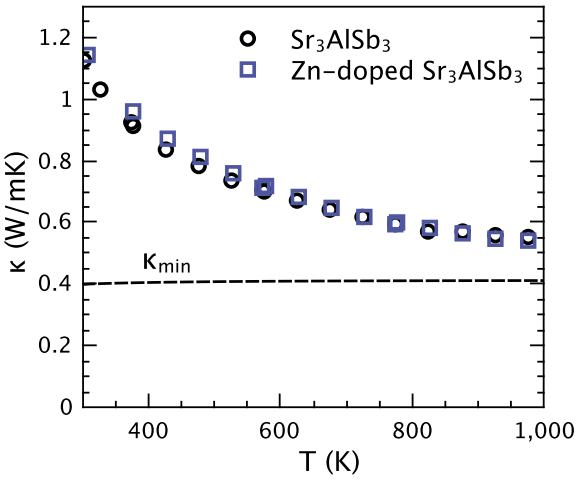

Figure 7.5: The thermal conductivity (κ) of Sr_3AlSb_3 approaches the predicted minimum lattice thermal conductivity (κ_{min}) at high temperature, due in part to the complex unit cell.

in the current study we find that replacing 5% of the Al with Zn in Sr_3AlSb_3 had no appreciable effect on n_H. This suggests that Zn is not an effective dopant in Sr_3AlSb_3, perhaps forming a secondary phase rather than occupying the intended Al sites. Nevertheless, the Zn-containing sample was found to have higher μ_H than the undoped sample (Figure 4c). While the improved mobility led to a reduction in both ρ and α, the temperature dependence of both properties remains consistent with nondegenerate semiconducting behavior. In contrast, the same concentration of Zn in the related compound, Sr_3GaSb_3 resulted in degenerate semiconducting behavior. From the resistivity of nominally Zn-doped Sr_3AlSb_3 (see inset in Fig 7.4 (a)), an independent estimate of the band gap made using the relation $\rho \propto e^{E_g/2k_BT}$ yields $E_g\sim$ 0.7 eV [154].

Thermal Transport Properties The thermal conductivity of Sr_3AlSb_3 is shown in Figure 7.5. Due to high electrical resistivity in both samples, the electronic contribution to κ is negligible, and κ in Figure 7.5 can be considered equivalent to the lattice thermal conductivity, κ_L. With increasing temperature, κ_L decreases due to Umklapp scattering, reaching 0.55 W/mK at 1000 K. The minimum the-

oretical κ_L for Sr_3AlSb_3 (shown as a dashed line in Fig 7.5) was calculated from $\kappa_{min} = \frac{1}{2}\left(\frac{\pi}{6}\right)^{1/3} k_B V^{-2/3}(2\nu_S + \nu_L)$ [80, 121]. Here, V is the atomic volume, and the longitudinal and transverse sound velocities (ν_L=2069 m/s and ν_T=3632 m/s) were obtained from ultrasonic measurements. The lattice thermal conductivity of Sr_3AlSb_3 approaches κ_{min} at high temperature, due primarily to the complexity of its unit cell (56 atoms per primitive cell) [8].

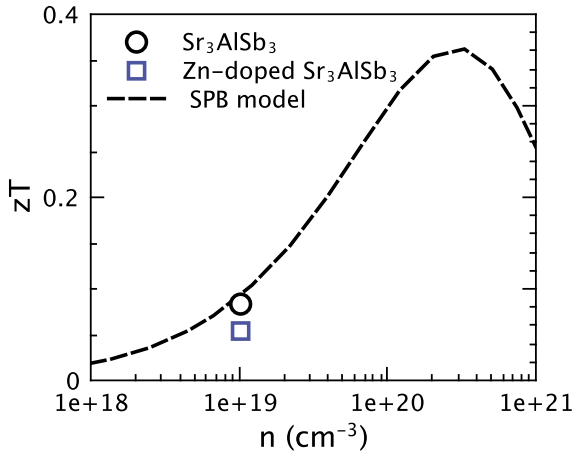

Figure 7.6: An SPB model at 600 K (dashed line) assuming m^*=3 m_e and μ_o=2.8 cm^2/Vs illustrates the potential improvement in zT expected to result from successful doping of Sr_3AlSb_3.

Figure of Merit Classic Zintl phases are generally intrinsic semiconductors with low carrier concentrations, and are therefore not optimized for thermoelectric applications. Optimizing the carrier concentration of these classic compounds through electronic doping can increase the peak zT by nearly an order of magnitude relative to undoped material [5, 129, 10]. For example, undoped Ca_3AlSb_3 has a carrier concentration of 10^{18} h^+/cm^3 and a peak zT value of only 0.1 at 1000 K, while optimally doped Ca_3AlSb_3 has a peak zT of 0.78. In the present study, Sr_3AlSb_3 exhibits a low carrier concentration and a peak zT of approximately 0.15 at 800 K. Zn did not increase the carrier concentration and thus did not lead to improved zT. To estimate the potential gains in zT that *could* be realized in this system with successful doping, a single band model was employed at 600 K. A band mass of m^*=3 m_e and intrin-

sic mobility of μ_o=2.8 cm^2/Vs were obtained from the experimental α, n_H, and μ_H of the undoped sample. This simple model clearly demonstrates that higher carrier concentrations are necessary to realize the full potential of the Sr_3AlSb_3 system. The estimated optimal zT of ∼0.3 in Sr_3AlSb_3 is comparable to that of Ca_3AlSb_3 at 600 K, suggesting that similarly high peak zT values (∼0.8) might be achieved through doping. However, we emphasize that our use of an intrinsic sample to obtain the parameters for this model leads to uncertainty in the exact value of the optimum carrier concentration and zT.

7.3 Conclusion

Here, we have described the electronic structure and thermoelectric properties of the Zintl phase Sr_3AlSb_3, a potential new thermoelectric material based on relatively earth-abundant, non-toxic elements. The structure of Sr_3AlSb_3 is characterized by edge-sharing pairs of tetrahedra, in contrast to the chain-forming phases Sr_3GaSb_3 and Ca_3AlSb_3. The large unit cell and comparatively high density in Sr_3AlSb_3 combine to yield extremely low lattice thermal conductivity ($\kappa_L \sim 0.55$ W/mK). Density Functional theory predicts a band gap of E_g∼1.0 eV in Sr_3AlSb_3 and an average valence band mass approximately twice that of Sr_3GaSb_3 and Ca_3AlSb_3. High temperature transport measurements are in qualitative agreement with the calculated structure, showing that Sr_3AlSb_3 is a nondegenerate p-type semiconductor, with a band gap of E_g∼ 0.6 eV and relatively low mobility (up to 6 cm^2/Vs). While the addition of Zn did not lead to the expected extrinsic semiconducting behavior, the mobility was improved, and a single parabolic band model suggests that substantial zT values can be obtained in this system through the use of a successful p-type dopant.

Chapter 8

Comparison of $A_5M_2Sb_6$ and A_3MSb_3 Zintl Compounds

The following summary compares the thermoelectric properties of the seven $A_5M_2Sb_6$ and A_3MSb_3 Zintl compounds (A= Ca, Sr, and M = Al, Ga, or In) discussed in this thesis. Although these compounds form five different structure types, the chemical and structural similarities lead to very similar transport behavior. By comparing the transport properties of these closely related structure types, we can identify trends that can potentially be used to develop relationships between the chemistry and properties of Zintl phases and guide future work on Zintl thermoelectrics.

8.1 Electronic Structure

The dominant structural features in all $A_5M_2Sb_6$ and A_3MSb_3 compounds are anionic moieties formed from linked M-Sb tetrahedra. It is not surprising then that the electronic density of states show similar characteristics across the five different structure types investigated here. As expected, the valence band edge is dominated by M and Sb states, while the conduction band contains primarily cation electronic states, consistent with the salt-like nature of Zintl phases. In all of the compounds, M-Sb bonding and anti-bonding interactions lead to distinctive peaks in the the valence and conduction band, respectively. Peaks associated with M-Sb bonding interactions are found deep in the valence band (between -4 and -6 eV), as evidenced by the large fraction of M-character, while the corresponding M-Sb anti-bonding states gener-

ally generally determine the conduction band minimum. The only exception is the $Ca_5M_2Sb_6$ structure type, which contains both Sb-Sb bonds and M-Sb bonds. Here, the anti-bonding states associated with Sb-Sb interactions form the conduction band edge, while M-Sb states are found at slightly higher energies. Despite the reduced importance of the M-Sb bonds in $Ca_5M_2Sb_6$, substitutions on the M-site were still found to play an indirect role in determining the size of the band gap in the $Ca_5M_2Sb_6$ system.

Table 8.1: Band gaps were calculated from DFT calculations and from the experimental resistivity and Seebeck coefficients, and were measured directly using optical absorption measurements.

	DFT (eV)	from ρ (eV)	from α (eV)	optical (eV)
$Ca_5Al_2Sb_6$	0.5	0.7	0.5	0.65
$Ca_5Ga_2Sb_6$	0.29	0.6	0.3	0.43
$Ca_5In_2Sb_6$	0.48	0.7	0.4	0.64
$Sr_5Al_2Sb_6$	0.78	0.5	0.4	-
Ca_3AlSb_3	0.25	-	0.6	-
Sr_3GaSb_3	0.77	-	0.5	-
Sr_3AlSb_3	1.05	0.7	0.6	-

The electronic band gaps (E_g) of $A_5M_2Sb_6$ and A_3MSb_3 compounds were estimated using several independent methods; density functional theory, the slope of the high temperature resistivity, the maximum Seebeck value, and from optical measurements. These values are given in Table 8.1. Considering only DFT calculations performed with using the modified Beck-Johnson semi-local exchange potential (excludes calculations for Ca_3AlSb_3), the Sr-based compounds appear to have larger band gaps than Ca-containing compounds. Among the three $Ca_5M_2Sb_6$ compounds with the same structure type, E_g decreases with increasing M electronegativity due to the shift of the M-Sb anti-bonding states towards lower energies.

The key features of the electronic band dispersions (the band degeneracy, band mass, and anisotropy) were found to vary significantly in compounds with different structure types. In the compounds considered here, the exact number of bands that contribute to transport in the valence band is difficult to specify precisely due to

multiple bands within a few k_BT of the band edge. Table 8.2 lists the band degeneracy at the valence band edge ($N_{v,edge}$), which includes only the topmost band(s). The number of additional bands within 0.1 eV of the band edge is given by $N_{v,add}$. Whether or not these additional bands are involved in transport depends on several factors: the energy of the band maximum relative to $E_F = 0$, the degree of Fermi spreading at a given temperature (nearly 0.1 eV at very high temperatures), and the location of the Fermi level, which varies significantly with doping.

Table 8.2: $N_{v,edge}$ is the valence band degeneracy at E_F=0, and $N_{v,add}$ is the number of additional bands within 0.1 eV of the band edge. The single band effective mass, m^*, is given in three perpendicular directions, where m_1^* is parallel to the tetrahedral chains or pairs. m_{DOS}^* is the estimated range for the density of states effective mass.

	$N_{v,edge}$	$N_{v,add.}$	m_1^* (m_e)	m_2^* (m_e)	m_1^* (m_e)	m_{DOS}^* (m_e)
$Ca_5Al_2Sb_6$	2	0	0.20	6.49	1.36	1.92
$Ca_5Ga_2Sb_6$	2	0	0.18	3.74	1.19	1.46
$Ca_5In_2Sb_6$	2	0	0.21	3.76	1.53	1.80
$Sr_5Al_2Sb_6$	-	-	-	-	-	-
Ca_3AlSb_3	2	1	0.15, 0.75	0.15, 0.75	0.75	0.85 -1.11
Sr_3GaSb_3	1	2	0.18	0.57	0.66	0.41 - 0.85
Sr_3AlSb_3	1	2	1.80	1.25	0.21	0.78 - 1.62

Anisotropy The structure types discussed in this thesis are highly anisotropic, leading to a large degree of anisotropy in the electronic band structures. Table 8.2 lists the single band effective mass (m^*) in three perpendicular directions. As might be expected, the orientation of the anionic substructure influences m^*; In compounds with chain-forming structures, the band mass parallel to the chains (m_1^*) is generally lightest. However, this simple picture is complicated by the presence of multiple bands. While the the topmost bands ($N_{v,edge}$) in the chain-forming structures show preference for transport along the chains, the additional bands ($N_{v,add}$) are essentially isotropic. In contrast, in Sr_3AlSb_3, which contains pairs of tetrahedra, the topmost band is lightest in the direction perpendicular to the tetrahedral pairs. These results suggest that while anisotropy in the anionic substructure is important, it cannot necessarily be used as a direct predictor of anisotropy in the band structure or in

electronic transport.

The density of states effective mass, m^*_{DOS}, was estimated using Eq 8.1.

$$m^*_{DOS} = (m^*_1 m^*_2 m^*_3)^{1/3} N_v^{2/3} \tag{8.1}$$

To express the possible range in m^*_{DOS} that stems from differences in the total number of contributing bands, $N_v = N_{v,edge}$ and $N_v = N_{v,add} + N_{v,edge}$ were used as lower and upper bounds. Although these estimates are imprecise, they highlight the lower mass found in Sr_3GaSb_3 and Ca_3AlSb_3 relative to the $Ca_5M_2Sb_6$ compounds.

8.2 Electronic Transport Properties

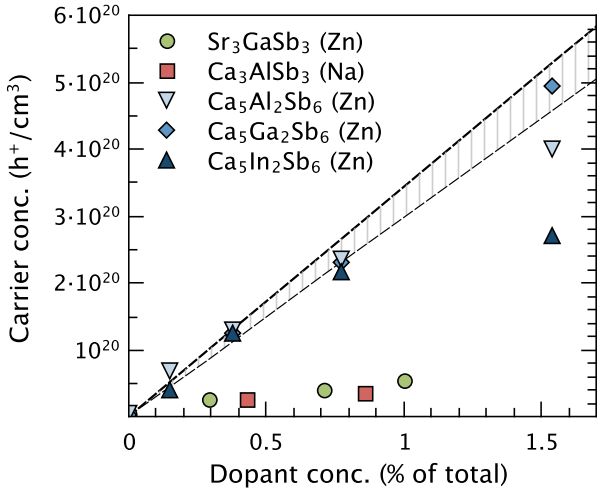

Figure 8.1: Dependence of the experimental Hall carrier concentration on dopant concentration. Dashed lines show the predicted carrier concentration as upper and lower bounds.

Consistent with DFT calculations, $A_5M_2Sb_6$ and A_3MSb_3 Zintl compounds exhibit low carrier concentrations ($n_H < 10^{19} h^+ cm^{-3}$) and behave as intrinsic semiconductors, necessitating doping to optimize the figure of merit. Substitution of Na^{1+} on the A^{2+} site, or Zn^{2+} on the M^{3+} site, was successfully used to increased the p-type carrier concentration in most cases. Figure 8.1 shows the predicted (dashed

lines) and experimental carrier concentrations resulting from a given dopant concentration. In the three $Ca_5M_2Sb_6$ compounds, the carrier concentrations resulting from doping is very close to the predicted values (one free carrier per dopant). However, in Sr_3GaSb_3 and Ca_3AlSb_3, the doping efficiency is very low; n_H increases, but only at a fraction of the expected rate. Finally, doping $Sr_5Al_2Sb_6$ and Sr_3AlSb_3 with Zn had no effect on n_H. This disparity likely stems from both geometric factors and differences in the electronic structure. For example, the $Ca_5M_2Sb_6$ structure type is formed by a large number of compounds, suggesting that the higher doping efficiency in these compounds is due to the more flexible structure. In contrast, $Sr_5Al_2Sb_6$ and Sr_3GaSb_3 are the only compounds known to form their particular structure types.

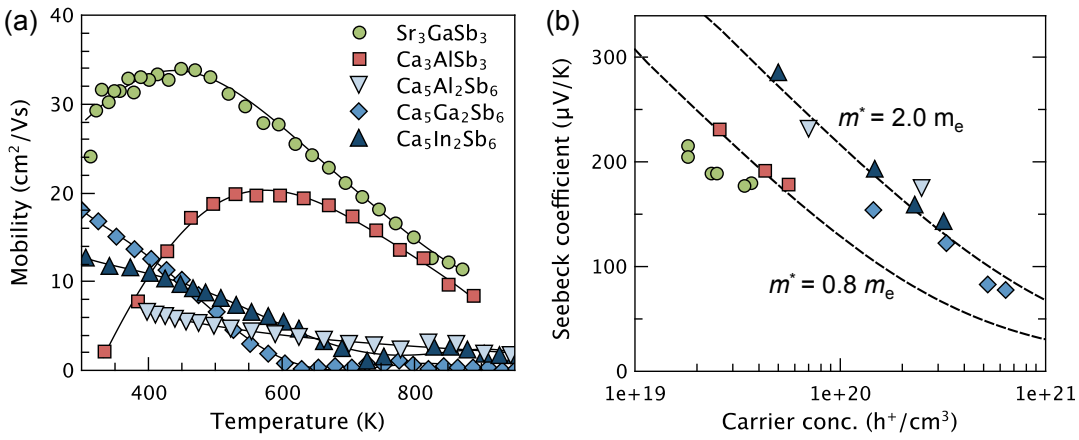

Figure 8.2: (a) The Hall mobility and (b) Seebeck coefficients of chain-forming Zintl compounds are a function of effective mass.

Among the chain-forming compounds discussed in this thesis, the heaviest band masses were predicted for the $Ca_5M_2Sb_6$ compounds. Larger band mass implies lower carrier mobility, larger Seebeck coefficients, and ultimately, that higher carrier concentrations are necessary to optimize zT. Experimentally, $Ca_5M_2Sb_6$ was found to have lower Hall mobility and higher Seebeck coefficients (Figure 8.2a and b, respectively) than either Sr_3AlSb_3 and Ca_3AlSb_3. The dashed curves in Figure 8.2b were calculated using an SPB model, yielding band masses of 2.0 m_e and 0.8 m_e, respectively, for the upper and lower curves. These values are in good agreement with the

m^*_{DOS} values predicted using DFT calculations.

8.3 Thermal Transport Properties

In complex materials, the size of the unit cell is one of the most important predictors of lattice thermal conductivity, κ_L. Figure 8.3 illustrates the decrease in κ_L with increasing unit cell volume in Zintl antimonides. This trend also applies to the specific compounds described in this thesis; the lowest values of κ_L were found in Sr_3GaSb_3, Sr_3AlSb_3, and $Sr_5Al_2Sb_6$, all of which have unit cells containing at least 50 atoms (marked by asterisks).

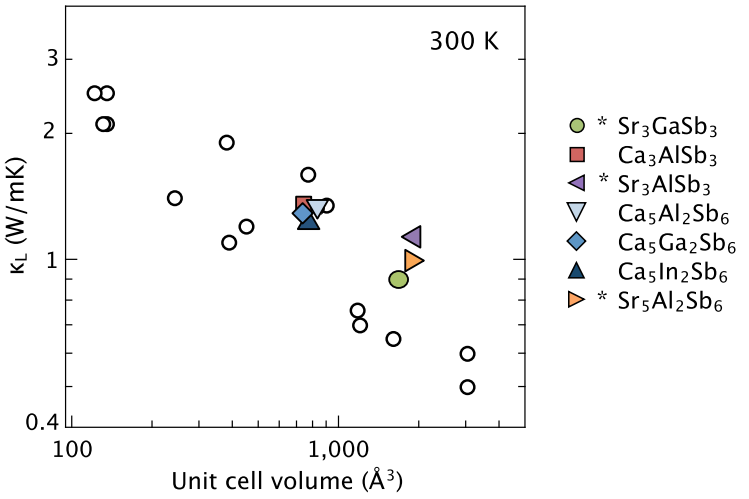

Figure 8.3: The room temperature lattice thermal conductivity of Zintl antimonides decreases with increasing unit cell volume. $A_5M_2Sb_6$ and A_3MSb_3 compounds fit the expected trend. Data is tabulated in Appendix A.

Lattice thermal conductivity is also dependent on the sound velocity, which contributes to the variation in κ_L in compounds with the same unit cell volume. The longitudinal and transverse sound velocities in a solid are related to the material's stiffness and density according to equations 8.2 and 8.3, where d is the theoretical density and K and G are the bulk and shear moduli, respectively. Table 8.3 lists the experimental sound velocities and calculated elastic moduli for each compound. The decrease in the experimental sound velocity with increasing theoretical density is

shown in Figure 8.4, where the dashed lines illustrate the predicted decrease assuming a constant stiffness.

$$\nu_T = \sqrt{\frac{G}{d}} \tag{8.2}$$

$$\nu_L = \sqrt{\frac{K + \frac{4}{3}G}{d}} \tag{8.3}$$

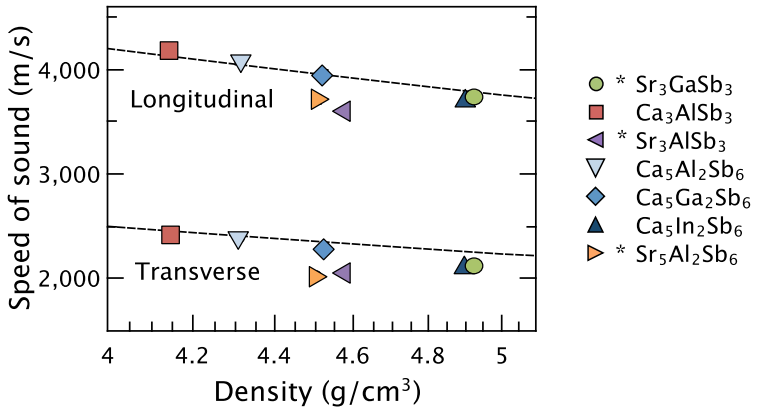

Figure 8.4: The speed of sound decreases with increasing density. The predicted decrease assuming constant shear and bulk moduli is illustrated by the dashed lines.

Table 8.3: The number of atoms per unit cell (N), theoretical density (d), shear and bulk moduli (G and K), and longitudinal and transverse speeds of sound (ν_l and ν_t).

	N	d (g/cm^3)	G (Gpa)	K (GPa)	ν_l (m/s)	ν_t (m/s)
$Ca_5Al_2Sb_6$	26	4.31	24.8	39.4	2400	4100
$Ca_5Ga_2Sb_6$	26	4.52	23.5	40.9	2280	3970
$Ca_5In_2Sb_6$	26	4.90	21.9	38.2	2120	3710
$Sr_5Al_2Sb_6$	52	4.50	18.9	37.2	2050	3720
Ca_3AlSb_3	28	4.14	24.6	39.1	2440	4170
Sr_3GaSb_3	56	4.92	22.3	39.4	2130	3750
Sr_3AlSb_3	56	4.58	19.6	34.2	2070	3630

Shown in Figure 8.5 are the lattice thermal conductivities of Zn-doped Sr_3GaSb_3, Ca_3AlSb_3, and $Ca_5M_2Sb_6$, and undoped $Sr_5Al_2Sb_6$ and Sr_3AlSb_3 as a function of temperature. Remarkably, the temperature dependence of κ_L is similar in all compounds, exhibiting a 1/T decay indicative of Umklapp scattering. It is instructive to compare

Sr_3GaSb_3 and $Ca_5In_2Sb_6$, which have nearly identical densities and sound velocities, but unit cells that differ in size by a factor of two. Despite this, κ_L in Sr_3GaSb_3 is approximately 20% lower across the entire temperature range. Assuming that the Grüneisen parameter does not vary greatly between these compounds, the difference in κ_L can most likely be explained by larger unit cell of Sr_3GaSb_3 (N= 56).

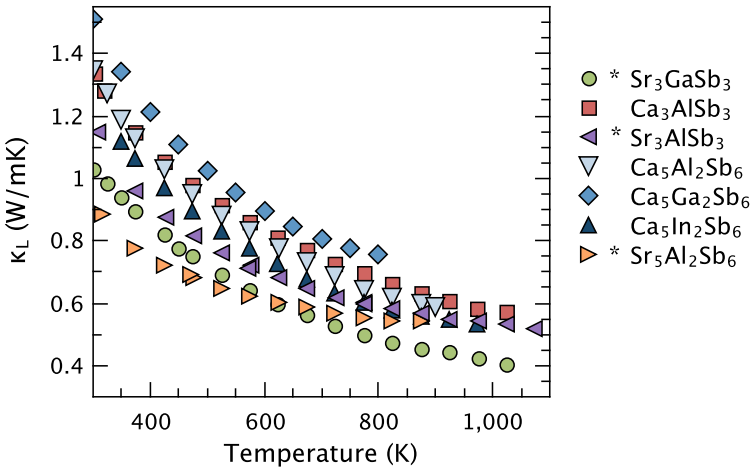

Figure 8.5: The magnitude of the lattice thermal conductivity of chain-forming Zintl phases is a function of sound velocity and unit cell size. Compounds containing more than 50 atoms per unit cell are marked with asterisks.

8.4 Figure of Merit

The figures of merit of optimally-doped Ca_3AlSb_3, Sr_3GaSb_3 and $Ca_5M_2Sb_6$ samples are shown in Figure 8.6. Due to the difference in effective mass, the optimal carrier concentration for $Ca_5M_2Sb_6$ compounds is approximately 10^{20} h^+/cm^3, while Ca_3AlSb_3 and Sr_3GaSb_3 are optimized when $n_H = 5\times10^{19}$ h^+/cm^3. Relative to the other chain-forming Zintl compounds, Sr_3GaSb_3 exhibits a higher figure of merit across the entire measured temperature range, which can be attributed almost entirely to its lower κ_L. However, in all optimally-doped samples, promising values were obtained for the peak zT, highlighting the value of continuing investigations of new Zintl phases. Future improvements to the thermoelectric performance of these

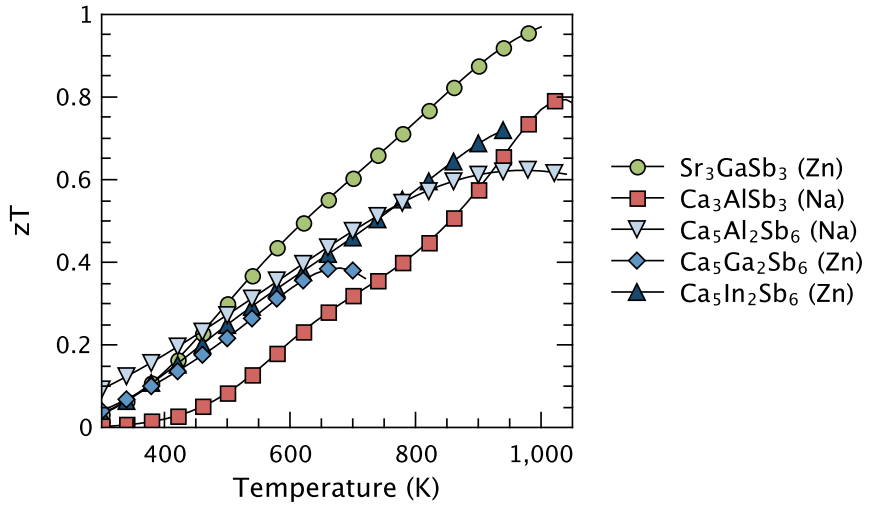

Figure 8.6: The figures of merit of optimally doped Ca_3AlSb_3 and Sr_3GaSb_3 and $Ca_5M_2Sb_6$ samples highlight the importance of low κ_L and high electronic mobility.

compounds may stem from optimization of the synthetic techniques, and from further tuning of the band structure through isoelectronic substitutions.

Appendix A

List of $A_5M_2Pn_6$ and A_3MPn_3 Compounds

The following table lists all known $A_5M_2Pn_6$ and A_3MPn_3 compounds (A= Ca, Sr, Ba, Eu, and M = Al, Ga, In, and Pn = P, As, Sb) that crystallize in the five structure types discussed in this thesis. The experimentally determined lattice parameters are given for each compound. The relevant crystallographic studies are cited in each table, and the compounds included in this thesis are marked with asterisks.

Table A.1:

$Ca_5Ga_2As_5$:	***P*bam**	***Z*=2**					
	a	b	c				ref.
$Ca_5Ga_2As_6$	13.224	11.357	4.138				[170]
$Ca_5Al_2Sb_6$ *	12.124	14.093	4.510				[13]
$Ca_5Ga_2Sb_6$ *	14.021	12.106	4.452				[9]
$Ca_5In_2Sb_6$ *	14.256	12.133	4.457				[9]
$Sr_5In_2Sb_6$	14.749	12.696	4.660				[9]
$Ba_5In_2Sb_6$	15.307	13.358	4.786				[11]
$Eu_5In_2Sb_6$	12.510	14.584	4.624				[146]
$Sr_5Al_5Sb_6$:	***P*nma**	***Z*=4**					
	a	b	c				ref.
$Sr_5Al_2Sb_6$ *	12.124	10.341	13.409				[11]
Ca_3InP_3:	***P*nma**	***Z*=2**					
	a	b	c				ref.
Ca_3InP_3	12.019	4.138	13.460				[158]
Sr_3InP_3	12.809	4.330	13.866				[122]
Eu_3InP_3	12.652	4.268	13.564				[159]
Ca_3AlAs_3	12.212	4.201	13.434				[171]
Ca_3GaAs_3	12.171	4.197	13.414				[158]
Ca_3AlSb_3 *	12.835	4.489	14.282				[12]
Sr_3GaSb_3:	***P*2$_1$/n**	***Z*=4**					
	a	b	c	α	β	γ	ref.
Sr_3GaSb_3 *	11.762	14.509	11.749	90	110.0	90	[122]
Ba_3AlSb_3:	***C*mca**	***Z*=4**					
	a	b	c				ref.
Eu_3GaP_3	18.543	6.335	12.276				[172]
Sr_3AlSb_3 *	20.410	6.900	13.501				[65]
Ba_3AlSb_3	21.133	7.194	14.069				[173]

Appendix A

Lattice thermal conductivity of Zintl antimonides

Table A.1: Room temperature lattice thermal conductivity, κ_L, for Zintl antimonides with unit cell volume, V_{unit}, and number of atoms per unit cell, N.

	V_{unit}	N	κ_L	ref.
LiZnSb	122	6	2.5	[45]
Mg_3Sb_2	131	5	2.1	[174]
$SrZn_2Sb_2$	135	5	2.1	[75]
$YbZn_2Sb_2$	135	5	2.5	[75]
$BaZn_2Sb_2$	242	8	1.4	[175]
$CeFe_4Sb_{12}$	381	17	1.9	[176]
$SrZnSb_2$	449	16	1.2	[46]
$Ca_5Ga_2Sb_6$	756	26	1.3	[126]
$Ca_5Al_2Sb_6$	759	26	1.33	[125]
$Yb_5In_2Sb_6$	768	26	1.6	[147]
$Ca_5In_2Sb_6$	771	26	1.25	[127]
Ca_3AlSb_3	822	28	1.33	[128]
$Ba_4In_8Sb_{16}$	897	28	1.35	[50]
$Yb_{11}Sb_{10}$	1177	42	0.76	[47]
$Yb_{11}GaSb_9$	1201	40	0.7	[48]
Zn_4Sb_3	1607	69	0.65	[177]
$Sr_5Al_2Sb_6$	1681	52	0.9	Ch. 4
Sr_3GaSb_3	1884	56	1.0	[129]
Sr_3AlSb_3	1901	56	1.14	[65]
$Yb_{14}MnSb_{11}$	3029	104	0.5	[21]
$Yb_{14}AlSb_{11}$	3037	104	0.6	[21]

Bibliography

[1] C. B. Vining, Thermoelectric properties of pressure-sintered SiGe thermoelectric alloys, *J. Appl. Phys* **69**, 4333-4340 (1991).

[2] Y. Pei, N. A. Heinz, A. LaLonde, G. J. Snyder, Combination of large nanostructures and complex band structure for high performance thermoelectric lead telluride, *Energ. Environ. Sci.* **4**, 3640 (2011).

[3] Y. Pei, et al., Synthesis and thermoelectric properties of $K_yCo_4Sb_{12}$, *Appl. Phys. Lett.* **89**, 221107 (2006).

[4] C. A. Cox, et al., Structure, heat capacity, and high-temperature thermal properties of $Yb_{14}Mn_{1-x}Al_xSb_{11}$, *Chem. Mater.* **21**, 1354-1360 (2009).

[5] A. Zevalkink, E. S. Toberer, W. G. Zeier, E. Flage-Larsen, G. J. Snyder, Ca_3AlSb_3: an inexpensive, non-toxic thermoelectric material for waste heat recovery, *Energ. Environ. Sci.* **4**, 510 (2011).

[6] A. F. May, E. S. Toberer, A. Saramat, G. J. Snyder, Characterization and analysis of thermoelectric transport in n-type $Ba_8Ga_{16-x}Ge_{30+x}$, *Phys. Rev. B* **80** (2009).

[7] G. A. Slack, *Solid State Physics*, vol. 34 (Academic Press, New York, 1979).

[8] E. S. Toberer, A. Zevalkink, G. J. Snyder, Phonon engineering through crystal chemistry, *J. Mater. Chem.* **21**, 15843 (2011).

[9] G. Cordier, H. Schafer, M. Stelter, Perantimonidogallate und Indate: zur Kenntnis von $Ca_5Ga_2Sb_6$, $Ca_5In_2Sb_6$, $Sr_5In_2Sb_6$, *Z. Naturforsch., B* **33**, 5-8 (1986).

[10] E. S. Toberer, A. Zevalkink, G. Snyder, The Zintl compound $Ca_5Al_2Sb_6$ for low cost thermoelectric power generation, *Adv. Funct. Mater.* **20**, 4375-4380 (2010).

[11] G. Cordier, M. Stelter, $Sr_5Al_2Sb_6$ und $Ba_5In_2Sb_6$: zwei neue Zintlphasen mit unterschiedlichen Baenderanionen, *Z. Naturforsch* **43b**, 463-466 (1988).

[12] G. Cordier, H. Schaefer, M. Stelter, Ca_3AlSb_3 und $Ca_5Al_2Bi_6$, zwie neue Zintlphasen mit kettenförmigen Anionen, *Z. Naturforsch* **39b**, 727-732 (1984).

[13] G. Cordier, E. Czech, M. Jakowski, H. Schaefer, Zintlphasen mit komplexen Anionen: zur Kenntnis von $Ca_5Al_2Sb_6$ und $Ca_3Al_2As_4$, *Rev. Chemie Minerale* **18**, 9-18 (1981).

[14] G. Cordier, M. Stelter, H. Schaefer, Zintl phases with complex anions - data on $Sr_6Al_2Sb_6$, *J. of Less Common Metals* **98**, 285-290 (1984).

[15] L. E. Bell, Cooling, heating, generating power, and recovering waste heat with thermoelectric systems, *Science* **321**, 1457 (2008).

[16] G. S. Nolas, J. Sharp, H. J. Goldsmid, *Thermoelectrics - Basic principles and new materials developments* (Springer, Heidelberg, Germany, 2001).

[17] F. J. DiSalvo, Thermoelectric cooling and power generation, *Science* **285**, 703-706 (1999).

[18] G. J. Snyder, E. S. Toberer, Complex thermoelectric materials, *Nature Mater.* **7**, 105-114 (2008).

[19] Y. Pei, et al., Convergence of electronic bands for high performance bulk thermoelectrics, *Nature* **473**, 66-9 (2011).

[20] Y. Pei, J. Lensch-Falk, E. S. Toberer, D. L. Medlin, G. J. Snyder, High thermoelectric performance in PbTe due to large nanoscale Ag_2Te precipitates and La doping, *Adv. Funct. Mater.* **21**, 241-249 (2011).

[21] E. S. Toberer, et al., Traversing the metal-insulator transition in a Zintl phase: rational enhancement of thermoelectric efficiency in $Yb_{14}Mn_{1-x}Al_xSb_{11}$, *Adv. Funct. Mater.* **18**, 2795-2800 (2008).

[22] S. K. Bux, et al., Nanostructured bulk silicon as an effective thermoelectric material, *Adv. Funct. Mater.* **19**, 2445-2452 (2009).

[23] A. F. May, D. J. Singh, G. J. Snyder, Influence of band structure on the large thermoelectric performance of lanthanum telluride, *Phys. Rev. B* **79**, 153101 (2009).

[24] S. M. Kauzlarich, ed., *Chemistry, Structure, and Bonding of Zintl Phases and Ions* (VCH Publishers, Inc, New York, 1996).

[25] F. Laves, Eduard Zintls Arbeiten uber die Chemie und Struktur von Legierungen, *Naturwiss* **29** (1941).

[26] E. Zintl, Intermetallische Verbindungen, *Angew. Chem.* **52** (1939).

[27] W. Klemm, Centenary lecture - metalloids and their compounds with the alkali metals, *Proc. Chem. Soc. London* **12**, 329 (1958).

[28] R. Hoffmann, *A Chemist's View of Bonding in Extended Structures* (VCH Publishers, Inc, Weinheim New York, 1988).

[29] R. Nesper, Bonding patterns in intermetallic compounds, *Angen. Chem. Int. Ed. Engl.* **30**, 789-817 (1991).

[30] W. B. Pearson, Classification of the crystal-structures of intermetallic phases according to building principles and properties, *J. Less-Common Met.* **109** (1985).

[31] H. G. Witte, J. von Schnering, Die Kristallstruktur von NaSi und NaGe, *Z. Anorg. Allg. Chem* **327**, 260-273 (1964).

[32] F. Gascoin, S. Ottensmann, D. Stark, M. S. Haile, G. Snyder, Zintl phases as thermoelectric materials: tuned transport properties of the compounds $Ca_xYb_{1-x}Zn_2Sb_2$, *Adv. Funct. Mater.* **15**, 1860-1864 (2005).

[33] J. K. Burdett, G. J. Miller, Fragment formalism in main-group solids: applications to AlB_2, $CaAl_2Si_2$, $BaAl_4$, and related materials, *Chem. Mater.* **2**, 12-26 (1990).

[34] G. Cordier, H. Schaefer, M. Stelter, Darstellung und Struktur der Verbindung $Ca_{14}AlSb_{11}$, *Z. Anorg. Allg. Chem* **519**, 183-188 (1984).

[35] H. Schaefer, On the problem of polar intermetallic compounds: the stimulation of E. Zintl's work for the modern chemistry of intermetallics, *Ann. Rev. Mater. Sci* **15**, 1-41 (1985).

[36] S. M. Kauzlarich, S. R. Brown, G. J. Snyder, Zintl phases for thermoelectric devices, *Dalton Trans.* pp. 2099–107 (2007).

[37] E. S. Toberer, A. F. May, G. J. Snyder, Zintl chemistry for designing high efficiency thermoelectric materials, *Chem. Mater.* **22**, 624-634 (2010).

[38] S. Brown, S. Kauzlarich, F. Gascoin, G. J. Snyder, $Yb_{14}MnSb_{11}$: New high efficiency thermoelectric material for power generation, *Chem. Mater.* **18**, 1873-1877 (2006).

[39] X.-J. Wang, et al., Synthesis and high thermoelectric efficiency of Zintl phase $YbCd_{2-x}Zn_xSb_2$, *Appl. Phys. Let.* **94**, 092106 (2009).

[40] H. Zhang, et al., Thermoelectric properties of $Eu(Zn_{1-x}Cd_x)_2Sb_2$, *Dalton Trans* **39**, 1101-4 (2010).

[41] Q.-G. Cao, et al., Zintl phase $Yb_{1-x}Ca_xCd_2Sb_2$ with tunable thermoelectric properties induced by cation substitution, *J. Appl. Phys.* **107**, 053714 (2010).

[42] E. S. Toberer, S. R. Brown, T. Ikeda, S. M. Kauzlarich, G. J. Snyder, High thermoelectric efficiency in lanthanum doped $Yb_{14}MnSb_{11}$, *Appl. Phys. Lett.* **93**, 062110 (2008).

[43] S. Brown, et al., Improved thermoelectric performance in $Yb_{14}Mn_{1-x}Zn_xSb_{11}$ by the reduction of spin-disorder scattering, *Chem. Mater.* **20**, 3412-3419 (2008).

[44] J.-A. Paik, E. Brandon, T. Calliat, R. Ewell, J. P. Fleurial, Life testing of $Yb_{14}MnSb_{11}$ for high performance thermoelectric couples, *Proc. Nuclear Emerging Tech. for Space* (2011).

[45] E. S. Toberer, A. F. May, C. J. Scanlon, G. J. Snyder, Thermoelectric properties of *p*-type LiZnSb: assessment of ab initio calculations, *J. Appl. Phys.* **105**, 063701 (2009).

[46] A. F. May, E. S. Toberer, G. J. Snyder, Transport properties of the layered Zintl compound $SrZnSb_2$, *J. Appl. Phys.* **106**, 013706 (2009).

[47] S. R. Brown, S. M. Kauzlarich, F. Gascoin, G. Jeffrey Snyder, High-temperature thermoelectric studies of $A_{11}Sb_{10}$ (A =Yb, Ca), *Journal of Solid State Chemistry* **180**, 1414-1420 (2007).

[48] T. Yi, C. A. Cox, E. S. Toberer, G. J. Snyder, S. M. Kauzlarich, High-Temperature Transport Properties of the Zintl Phases $Yb_{11}GaSb_9$ and $Yb_{11}InSb_9$, *Chem. Mater.* **22**, 935-941 (2010).

[49] S.-M. Park, S.-J. Kim, M. G. Kanatzidis, A unique framework in $BaGa_2Sb_2$: a new Zintl phase with large tunnels, *Inorg. Chem.*. **40**, 3781-3785 (2001).

[50] S.-J. Kim, S. Hu, C. Uher, M. G. Kanatzidis, $Ba_4In_8Sb_{16}$: thermoelectric properties of a new layered zintl phase with infinite zigzag Sb chains and pentagonal tubes, *Chem. Mater.* **11**, 3154-3159 (1999).

[51] B. Saparov, S. Bobev, A. Ozbay, E. R. Nowak, Synthesis, structure and physical properties of the new Zintl phases $Eu_{11}Zn_6Sb_{12}$ and $Eu_{11}Cd_6Sb_{12}$, *J. Sol. State Chem.* **181**, 2690-2696 (2008).

[52] S.-M. Park, S.-J. Kim, M. G. Kanatzidis, $Eu_7Ga_6Sb_8$: A Zintl phase with Ga-Ga bonds and polymeric gallium antimonide chains, *J. Sol. State Chem.* **177**, 2867-2874 (2004).

[53] A. P. Holm, et al., $Eu_{10}Mn_6Sb_{13}$: A new ternary rare-earth transition metal Zintl phase, *Inorg. Chem.* **42**, 4660-4667 (2003).

[54] R. Lam, A. Mar, Synthesis and structure of $Ba_2Sn_3Sb_6$, a Zintl phase containing channels and chains, *Inorg. Chem.* **35**, 6959-6963 (1996).

[55] S.-M. Park, S.-J. Kim, M. G. Kanatzidis, Ga-Ga bonding and tunnel framework in the new Zintl phase $Ba_3Ga_4Sb_5$, *J. Sol. State Chem.* **175**, 310-315 (2003).

[56] J. Mathieu, et al., Flux growth and electronic properties of $Ba_2In_5Pn_5$ (Pn = P, As): Zintl phases exhibiting metallic behavior, *Chem. Mater.* **20**, 5675-5681 (2008).

[57] R. P. Hermann, et al., Neutron and nuclear inelastic scattering study of the Einstein oscillators in Ba-, Sr-, and Eu-filled germanium clathrates, *Phys. Rev. B* **72** (2005).

[58] Y. Takasu, et al., Off-center rattling and cage vibration of the carrier-tuned type-I clathrate $Ba_8Ga_{16}Ge_{30}$ studied by Raman scattering, *Phys. Rev. B* **82** (2010).

[59] G. S. Nolas, J. L. Cohn, G. A. Slack, S. B. Schujman, Semiconducting Ge clathrates: promising candidates for thermoelectric applications, *Appl. Phys. Lett.* **73**, 178 (1998).

[60] C. Uher, Skutterudites: Prospective novel thermoelectrics, *Semiconductors and Semimetals*, T. M. Tritt, ed. (Academic Press, San Diego, 2001), vol. 69, pp. 139–253.

[61] G. S. Nolas, G. Fowler, J. Yang, Assessing the role of filler atoms on the thermal conductivity of filled skutterudites, *J. Appl. Phys.* **100**, 043705 (2006).

[62] B. C. Sales, D. Mandrus, R. K. Williams, Filled skutterudite antimonides: a new class of thermoelectric materials, *Science* **272**, 1325-1328 (1996).

[63] D. Sanchez-Portal, R. M. Martin, S. M. Kauzlarich, W. E. Pickett, Bonding, moment formation, and magnetic interactions in $Ca_{14}MnBi_{11}$ and $Ba_{14}MnBi_{11}$, *Phys. Rev. B 65* **65**, 144414 (2002).

[64] A. Zevalkink, J. Swallow, G. J. Snyder, Thermoelectric properties of Mn-doped $Ca_5Al_2Sb_6$, *J. Elect. Mater.* **41**, 813-818 (2012).

[65] A. Zevalkink, G. S. Pomrehn, J. Swallow, Y. Takagiwa, G. J. Snyder, Thermoelectric properties and electronic structure of the Zintl phase Sr_3AlSb_3, *Chem. Sus. Chem.* p. 10.1002/cssc.201300518 (2013).

[66] G. S. Pomrehn, A. Zevalkink, W. G. Zeier, G. Snyder, Influence of electronegativity on defect formation in AZn_2Sb_2 Zintl phases (A=Ca, Sr, Eu, Yb), *Submitted* (2013).

[67] S.-Q. Xia, S. Bobev, New manganese-bearing antimonides and bismuthides with complex structures: synthesis, structural characterization, and electronic properties of $Yb_9Mn_{4+x}Pn_9$ (Pn = Sb or Bi), *Chem. Mater.* **22**, 840-850 (2009).

[68] S. K. Bux, et al., Glass-like lattice thermal conductivity and high thermoelectric efficiency in $Yb_9Mn_{4.2}Sb_9$, *J. Mater. Chem. A* p. Accepted (2013).

[69] C. A. Uvarov, F. Ortega-Alvarez, S. M. Kauzlarich, Enhanced high-temperature thermoelectric performance of $Yb_{14-x}Ca_xMnSb_{11}$, *Inorg. Chem.* **51**, 7617-24 (2012).

[70] S.-Q. Xia, S. Bobev, Interplay between size and electronic effects in determining the homogeneity range of the $A_9Zn_{4+x}Pn_9$ and $A_9Cd_{4+x}Pn_9$ Phases, A = Ca, Sr, Yb, Eu; Pn = Sb, Bi, *j. Am. Chem. Soc* **129**, 10011-10018 (2007).

[71] G. D. Mahan, Good thermoelectrics, *Solid State Phys.* (Academic Press, 1998), vol. 51 of *Academic Press*.

[72] I. Todorov, D. Y. Chung, L. Ye, A. J. Freeman, M. G. Kanatzidis, Synthesis, structure and charge transport properties of $Yb_5Al_2Sb_6$: a Zintl phase with incomplete electron transfer, *Inorg. Chem.* **48**, 4768-76 (2009).

[73] Y. Pei, A. D. LaLonde, H. Wang, G. J. Snyder, Low effective mass leading to high thermoelectric performance, *Energ. Environ. Sci.* **5**, 7963-7969 (2012).

[74] A. Zevalkink, et al., Influence of the triel elements (M = Al, Ga, In) on the transport properties of $Ca_5M_2Sb_6$ Zintl compounds, *Chem. Mater.* **24**, 2091-2098 (2012).

[75] E. S. Toberer, A. F. May, B. C. Melot, E. Flage-Larsen, G. J. Snyder, Electronic structure and transport in thermoelectric compounds $A$$Zn_2Sb_2$ (A = Sr, Ca, Yb, Eu), *Dalton Trans.* **39**, 1046-54 (2010).

[76] U. I. Ravich, B. A. Efimova, I. A. Smirnov, *Semiconducting lead chalcogenides* (Plenum Press, 1970).

[77] A. F. May, et al., Properties of single crystalline $A$$Zn_2Sb_2$ (A=Ca,Eu,Yb), *J. Appl. Phys.* **111**, 033708 (2012).

[78] R. Berman, *Thermal Conduction in Solids* (University Press, Oxford, 1976).

[79] T. M. Tritt, *Thermal Conductivity Theory, Properties, and Application*, Physics of Solids and Liquids (Plenum Publishers, New York, NY, 2004).

[80] D. G. Cahill, R. Pohl, Lattice vibrations and heat transport in crystals and glasses, *Ann. Rev. Mater. Sci* **39**, 93-121 (1988).

[81] A. Ward, D. A. Broido, D. A. Stewart, G. Deinzer, Ab initio theory of the lattice thermal conductivity in diamond, *Phys. Rev. B* **80**, 125203 (2009).

[82] A. Ward, D. A. Broido, Intrinsic phonon relaxation times from first principle studies of the thermal conductivity of Si and Ge, *Phys. Rev. B* **81**, 085205 (2010).

[83] J. An, A. Subedi, D. J. Singh, Ab Initio phonon dispersions for PbTe, *Cond. Mat. Mater. Sci.* (2008).

[84] J. Dong, O. F. Sankey, C. W. Myles, Theoretical study of the lattice thermal conductivity in Ge framework semiconductors, *Phys. Rev. Lett.* **86**, 2361 (2001).

[85] N. de Koker, Thermal conductivity of MgO periclase from equilibrium first principles molecular dynamics, *Phys. Rev. Lett.* **103**, 125902 (2009).

[86] N. Bernstein, D. J. Singh, Calculations of dynamical properties of skutterudites: thermal conductivity, thermal expansivity, and atomic mean-square displacement, *Phys. Rev. B* **81** (2010).

[87] C. J. Vineis, A. Shakouri, A. Majumdar, M. G. Kanatzidis, Nanostructured thermoelectrics: big efficiency gains from small features, *Adv. Mater.* **22**, 3970-80 (2010).

[88] S. K. Bux, J.-P. Fleurial, R. B. Kaner, Nanostructured materials for thermoelectric applications, *Chem. Comm.* **46**, 8311-8324 (2010).

[89] A. J. Minnich, M. S. Dresselhaus, Z. F. Ren, G. Chen, Bulk nanostructured thermoelectric materials: current research and future prospects, *Energ. Environ. Sci.* **2**, 466-479 (2009).

[90] G. Meisner, D. Morelli, S. Hu, J. Yang, C. Uher, Structure and lattice thermal conductivity of fractionally filled skutterudites: solid solutions of fully filled and unfilled end members, *Phys. Rev. Lett.* **80**, 3551-3554 (1998).

[91] P. G. Klemens, M. Gell, Thermal conductivity of thermal barrier coatings, *Materials Science and Engineering* **A245**, 143-149 (1998).

[92] J. Callaway, Model for lattice thermal conductivity at low temperatures, *Phys. Rev.* **113**, 1044-1051 (1959).

[93] M. G. Holland, Analysis of lattice thermal conductivity, *Phys. Rev.* **132**, 2461-2471 (1963).

[94] P. G. Klemens, Theory of thermal conductivity in solids, *Thermal Conductivity*, R. P. Tye, ed. (Academic Press, London, 1969), vol. 1.

[95] C. Dames, G. Chen, *CRC Handook of Thermoelectrics* (CRC Press, 2006), chap. Thermal conductivity of nanostructured thermoelectric materials.

[96] D. M. Rowe, V. S. Shukla, N. Savvides, Phonon scattering at grain boundaries in heavily doped fine-grained silicon-germanium alloys, *Nature* **290**, 765-766 (1981).

[97] C. Kittel, *Introduction to Solid State Physics* (Wiley and Sons, 2004).

[98] J. D. Chung, A. J. H. McGaughey, M. Kaviany, Role of phonon dispersion in lattice thermal conductivity modeling, *J. of Heat Trans.* **126**, 376 (2004).

[99] M. A. Black, Thermal conductivity and anharmonic forces, *Amer. J. Phys.* **41**, 691-696 (1972).

[100] J. S. Dugdale, D. K. C. MacDonald, Lattice thermal conductivity, *Phys. Rev.* **98**, 1955 (1955).

[101] M. Roufosse, P. G. Klemens, Lattice thermal conductivity of minerals at high temperatures, *Phys. Rev. B* **7**, 5379-5386 (1973).

[102] G. Leibfried, E. Schloemann, Thermal conductivity of dielectric solids by a variational technique, *Nachr. Akad. Wiss. Goettingen II* **A(4)** (1954).

[103] C. L. Julian, Theory of heat conduction in rare-gas crystals, *Phys. Rev.* **137**, A128-A137 (1965).

[104] G. A. Slack, S. Galginaitis, Thermal conductivity and phonon scattering by impurities in CdTe, *Phys. Rev.* **133** (1964).

[105] H. Wang, Y. Pei, A. D. LaLonde, G. J. Snyder, Heavily doped *p*-type PbSe with high thermoelectric performance: an alternative for PbTe, *Adv. Mater.* **23**, 1366-70 (2011).

[106] H. J. Goldsmid, A. W. Penn, Boundary scattering of phonons in solid solutions, *Phys. Lett.* **27A**, 523-524 (1968).

[107] J. E. Parrott, The thermal conductivity of sintered semiconductor alloys, *J. Phys. C: Solid State Phys.* **2**, 147-151 (1969).

[108] Ø. Prytz, E. Flage-Larsen, E. S. Toberer, G. J. Snyder, J. Tafto, Reduction of lattice thermal conductivity from planar faults in the layered Zintl compound $SrZnSb_2$, *J. Appl. Phys.* **109**, 043509 (2011).

[109] K. Guo, et al., Enhanced thermoelectric figure of merit of Zintl phase $YbCd_{2-x}Mn_xSb_2$ by chemical substitution, *Eu. J. Inorg. Chem.* **2011**, 4043-4048 (2011).

[110] C. Yu, et al., Improved thermoelectric performance in the Zintl phase compounds $YbZn_{2-x}Mn_xSb_2$ via isoelectronic substitution in the anionic framework, *J. Appl. Phys* **104**, 013705 (2008).

[111] P. G. Klemens, The scattering of low-frequency lattice waves by static imperfections, *Proc. Phys. Soc. A* **68**, 1113-1127 (1955).

[112] M. Blackman, On the heat conduction of simple cubical crystals, *Philo. Mag.* **19**, 989 (1935).

[113] M. Born, T. V. Karman, On fluctuations in spatial grids, *Phyzik Z.* **13**, 297 (1912).

[114] S. Pettersson, Calculation of the thermal conductivity of alkali halide crystals, *J. Phys. C: Solid State Phys.* **20**, 1047-1061 (1987).

[115] M. R. Winter, D. R. Clarke, Oxide materials with low thermal conductivity, *J. Am. Ceram. Soc.* **90**, 533-540 (2007).

[116] C. J. Friedrich, R. Gadow, M. H. Lischka, Lanthanum hexaaluminate thermal barrier coatings, *The 25th An. Int. Conf. on Composites, Advanced Ceramics, Materials, and Structures: B* pp. 375–382 (2001).

[117] T. Takeuchi, N. Nagasako, R. Asahi, U. Mizutani, Extremely small thermal conductivity of the Al-based Mackay-type 1x1-cubic approximants, *Phys. Rev. B* **74** (2006).

[118] N. P. Padture, P. G. Klemens, Low thermal conductivity in garnets, *J. Am. Ceram. Soc* **80**, 1018-1020 (1997).

[119] R. Bruls, H. T. Hintzen, R. Metselaar, On the crystal structure of the quasicrystalline approximant $YbCd_6$ at low temperature, *J. Appl. Phys.* **98**, 126101 (2005).

[120] G. A. Slack, *The thermal conductivity of non-metallic crystals*, vol. 34 (Academic Press, New York, 1979).

[121] D. Cahill, S. Watson, R. Pohl, Lower limit to the thermal conductivity of disordered crystals, *Phys. Rev. B* **46**, 6131-6140 (1992).

[122] G. Cordier, H. Schaefer, M. Stelter, Sr_3GaSb_3 und Sr_3InP_3 zwei neue Zintlphasen mit komplexen Anionen, *Z. Naturforsch* **42b**, 1268-1272 (1987).

[123] G. Cordier, M. Stelter, H. Schaefer, Zintlphasen mit komplexen Anionen: zur Kenntnis von $Sr_6Al_2Sb_6$, *J. Less-Common Metals* **98**, 285-290 (1984).

[124] A. F. May, J.-P. Fleurial, G. J. Snyder, Thermoelectric performance of lanthanum telluride produced via mechanical alloying, *Phys. Rev. B* **78**, 125205 (2008).

[125] A. Zevalkink, E. S. Toberer, T. Bleith, E. Flage-Larsen, G. J. Snyder, Improved carrier concentration control in Zn-doped $Ca_5Al_2Sb_6$, *J. Appl. Phys* **110**, 013721 (2011).

[126] S. I. Johnson, A. Zevalkink, G. J. Snyder, Improved thermoelectric properties in Zn-doped $Ca_5Ga_2Sb_6$, *J. Mater. Chem. A* **1**, 4244 (2013).

[127] A. Zevalkink, J. Swallow, G. J. Snyder, Thermoelectric properties of Zn-doped $Ca_5In_2Sb_6$, *Dalton Trans.* (2013).

[128] W. G. Zeier, A. Zevalkink, E. Schechtel, W. Tremel, G. J. Snyder, Thermoelectric properties of Zn-doped Ca_3AlSb_3, *J. Mater. Chem.* **22**, 9826 (2012).

[129] A. Zevalkink, et al., Thermoelectric properties of Sr_3GaSb_3, a chain-forming Zintl compound, *Energ. Environ. Sci.* **5**, 9121 (2012).

[130] A. Cohelo, Topas academic v4.1 (2004).

[131] K. A. Borup, et al., Measurement of the electrical resistivity and hall coefficient at high temperatures, *Rev. Sci. Instrum.* **Submitted** (2012).

[132] S. Iwanaga, E. S. Toberer, A. LaLonde, G. J. Snyder, A high temperature apparatus for measurement of the Seebeck coefficient, *Rev. Sci. Instrum.* **82** (2011). Iwanaga, Shiho Toberer, Eric S. LaLonde, Aaron Snyder, G. Jeffrey.

[133] C. Wood, D. Zoltan, G. Stapfer, Measurement of seebeck coefficient using a light pulse, *Rev. Sci. Instruments* **56**, 719 (1985).

[134] P. Kubelka, F. Munk, Reflection characteristics of paints, *Z. Technische Physik* **12**, 593-601 (1932).

[135] P. K. Basu, *Theory of Optical Processes in Semiconductors. Series on Semiconductor Science and Technology* (Oxford University Press, 1997).

[136] G. Kresse, J. Hafner, Ab-initio molecular dynamics for liquid metals, *Phys. Rev. B* **47**, 558-561 (1993).

[137] G. Kresse, J. Furthmuller, Efficiency of ab-initio total energy calculations for metals and semiconductors using a plane-wave basis set, *Comput. Mater. Sci.* **6**, 15-50 (1996).

[138] J. P. Perdew, K. Burke, M. Ernzerhof, Generalized gradient approximation made simple, *Phys. Rev. Lett.* **77**, 3865–3868 (1996).

[139] G. Kresse, D. Joubert, From ultrasoft pseudopotentials to the projector augmented-wave method, *Phys. Rev. B* **59**, 1758-1775 (1999).

[140] E. Flage-Larsen, O. M. Løvvik, Prytz, J. Ø. Taftø, Bond analysis of phosphorus skutterudites: elongated lanthanum electron buildup in $LaFe_4P_{12}$, *Comput. Mater. Sci.* **47**, 752-757 (2010).

[141] P. Blaha, K. Schwarz, G. Madsen, D. Kvasnicka, J. Luitz, WIEN2k: an augmented plane wave plus local orbitals program for calculating crystal properties, *Institute of Physical and Theoretical Chemistry, TU Vienna* (2001).

[142] F. Tran, P. Blaha, Accurate band gaps of semiconductors and insulators with a semilocal exchange-correlation potential, *Phys. Rev. Lett.* **102**, 226401 (2009).

[143] D. Koller, F. Tran, P. Blaha, Merits and limits of the modified becke-johnson exchange potential, *Phys. Rev. B* **83**, 195134 (2011).

[144] P. E. Blochl, Projector augmented-wave method, *Phys. Rev. B* **50** (1994).

[145] D. Heyd, E. Scuseria, M. Enzerhof, Hybrid functionals based on a screened coulomb potential, *J. Chemical Phys.* **118**, 8207-8215 (2003).

[146] S.-M. Park, E. S. Choi, W. Kang, S.-J. Kim, $Eu_5In_2Sb_6$, $Eu_5In_{2-x}Zn_xSb_6$: rare earth zintl phases with narrow band gaps, *J. Mater. Chem.* **12**, 1839-1843 (2002).

[147] S.-J. Kim, J. R. Ireland, C. R. Kannewurf, M. G. Kanatzidis, $Yb_5In_2Sb_6$: a new rare earth Zintl phase with a narrow band gap, *Journal of Solid State Chemistry* **155**, 55-61 (2000).

[148] W.-Q. Cao, Y.-G. Yan, X.-F. Tang, S.-K. Deng, The effects of In isoelectronic substitution for Ga on the thermoelectric properties of $Sr_8Ga_{16-x}In_xGe_{30}$ type-I clathrates, *J. Phys. D: Appl. Phys.* **41**, 215105 (2008).

[149] N. Nasir, et al., Clathrates $Ba_8(Zn,Cd)_xSi_{46-x}$, x$\sim$7: synthesis, crystal structure and thermoelectric properties, *J. Phys. Condens. Matter* **21** (2009).

[150] J. Xu, H. Kleinke, Unusual Sb-Sb bonding in high temperature thermoelectric materials, *J. Comput. Chem.* **29**, 2134-43 (2008).

[151] N. N. Greenwood, A. Earnshaw, *Chemistry of the elements* (Pergamon Press, 1989).

[152] E. H. Putley, *The Hall Effect and Related Phenomena*, vol. 34 (Butterworths, London, 1960).

[153] C. Herring, E. Vogt, Transport and deformation potential theory for many-valley semiconductors with anisotropic scattering, *Phys. Rev.* **101**, 944–961 (1956).

[154] H. J. Goldsmid, J. W. Sharp, Estimation of the thermal band gap of a semiconductor from Seebeck measurements, *J. Electron. Mater.* **28**, 869-872 (1999). Goldsmid, HJ Sharp, JW.

[155] R. D. Shannon, C. T. Prewitt, Effective ionic radii in oxides and fluorides, *Acta Cryst.* **B25**, 925-946 (1969).

[156] B. Sales, et al., Kondo lattice behavior in the ordered dilute magnetic semiconductor $Yb_{14-x}La_xMnSb_{11}$, *Phys. Rev. B* **72** (2005).

[157] H. J. Goldsmid, *Applications of Thermoelectricity* (J. Wiley and Sons Inc., New York, 1960).

[158] G. Cordier, H. Schaefer, M. Stelter, Neue Zintlphasen: Ba_3GaSb_3, Ca_3GaAs_3 und Ca_3InP_3, *Z. Naturforsch., B* **40**, 1100-1104 (1985).

[159] J. Jiang, et al., Complex magnetic ordering in Eu_3InP_3: a new rare earth metal Zintl compound, *Inorg. Chem.* **44**, 2189-2197 (2005).

[160] G. Cordier, H. Schaefer, Ca_3AlAs_3- ein intermetallisches Analogon zu den Kettensilicaten, *Angew. Chem.* **93**, 474 (1981).

[161] M. Somer, W. Cabrera, K. Peters, H. von Schnering, G. Cordier, Crystal structure of tribarium triarsenidoindate Ba_3InAs_3, *Z. Kristallogr.* **211**, 632 (1996).

[162] G. A. Papoian, R. Hoffmann, Hypervalent bonding in one, two, and three dimensions: extending the Zintl-Klemm concept to nonclassical electron-rich networks, *Angen. Chem. Int. Ed. Engl.* **39**, 2408-2448 (2000).

[163] M. Mills, R. Lam, M. J. Ferguson, L. Deakin, A. Mar, Chains, planes, and antimonides, *Coordination Chem. Rev.* **233-234**, 207-222 (2002).

[164] V. I. Fistul, *Heavily Doped Semiconductors* (Plenum Press, 1969).

[165] D.-Y. Chung, et al., $CsBi_4Te_6$: a high-performance thermoelectric material for low-temperature applications, *Science* **287**, 1024-1027 (2000).

[166] A. D. LaLonde, Y. Pei, H. Wang, G. J. Snyder, Lead telluride alloy thermoelectrics, *Mater. Today* **14**, 526-532 (2011).

[167] A. Zunger, Practical doping principles, *Appl. Phys. Let.* **83**, 57 (2003).

[168] R. Petritz, Theory of photoconductivity in semiconductor films, *Phys. Rev.* **104**, 1508-1516 (1956).

[169] Y. L. Yan, Y. X. Wang, Crystal structure, electronic structure, and thermoelectric properties of $Ca_5Al_2Sb_6$, *J. Mater. Chem.* **21**, 12497 (2011).

[170] P. Verdier, P. l'Haridon, M. Maunaye, Y. Laurent, Etude structural de $Ca_5Ga_2As_6$, *Acta Cryst. B* **32**, 726-728 (1976).

[171] G. Cordier, M. Stelter, H. Schaefer, Zintl phases with complex anions - data on Ca_3AlAs_3 and $Ba_6Al_2Sb_6$, *Z. Naturforschung* **37**, 975-980 (1982).

[172] M. Somer, W. Carrillo Cabrera, K. Peters, H. von Schnering, G. Cordier, Crystal structure of hexaeuropium di-mue-phosphido-bis(diphosphidogallate(III)) $Eu_6Ga_2P_6$, *Z. Kristallogr.* **211**, 257 (1996).

[173] G. Cordier, G. Savelsberg, H. Schaefer, Zintlphasen mit komplexen Anionen: zur Kenntnis von Ca_3AlAs_3 und Ba_3AlSb_3, *Z. Naturforsch., B* **37**, 975-980 (1982).

[174] C. L. Condron, S. M. Kauzlarich, F. Gascoin, G. J. Snyder, Thermoelectric properties and microstructure of Mg_3Sb_2, *J. Solid State Chem.* **179**, 2252 (2006).

[175] X.-J. Wang, M.-B. Tang, J.-T. Zhao, H.-H. Chen, X.-X. Yang, Thermoelectric properties and electronic structure of zintl compound bazn2sb2, *Appl. Phys. Lett.* **90**, 232107 (2007).

[176] D. T. Morelli, G. P. Meisner, Low temperature properties of the filled skutterudite $CeFe_4Sb_{12}$, *J. Appl. Phys.* **77**, 3777-3781 (1995).

[177] T. Caillat, J. P. Fleurial, A. Borshchevsky, Preparation and thermoelectric properties of semiconducting Zn_4Sb_3, *J. Phys. Chem. Solids* **58**, 1119–1125 (1997).